
Report No. KS-07-5
FINAL REPORT

FINITE ELEMENT ANALYSIS OF FATIGUE PRONE DETAILS OF THE TUTTLE CREEK BRIDGE

Ashish Bhargava
W. M. Kim Roddis, Ph.D., P.E.

November 2007

KANSAS DEPARTMENT OF TRANSPORTATION

**Division of Operations
Bureau of Materials and Research**



1 Report No. KS-07-5	2 Government Accession No.	3 Recipient Catalog No.	
4 Title and Subtitle Finite Element Analysis of Fatigue Prone Details of the Tuttle Creek Bridge		5 Report Date November 2007	6 Performing Organization Code
		8 Performing Organization Report No.	
7 Author(s) Ashish Bhargava*, W. M. Kim Roddis*, Ph.D., P.E. *currently associated with George Washington University		10 Work Unit No. (TRAIS)	
9 Performing Organization Name and Address Kansas University Transportation Center The University of Kansas 1530 W 15th Street, 2150 Learned Hall Lawrence, KS 66045-7609		11 Contract or Grant No. C1443	
		13 Type of Report and Period Covered Final Report Fall 2003- Spring 2007	
12 Sponsoring Agency Name and Address Kansas Department of Transportation Bureau of Materials and Research 700 SW Harrison Street Topeka, Kansas 66603-3745		14 Sponsoring Agency Code RE-0363-01	
		15 Supplementary Notes For more information write to address in block 9.	
16 Abstract <p>Many older steel girder bridges exhibit distortion-induced fatigue cracking at the cross-frame to girder connections. In a two-girder bridge like the Tuttle Creek Bridge there are no redundant load paths and this problem is of even greater concern. The primary girders of the bridge structure are fatigue critical elements and even when such cracks are relatively small they must be examined extensively. The Tuttle Creek Bridge, built in 1962, developed distortion-induced fatigue cracks in the web gap region. The crack prevention repairs of 1986 were not effective and continued crack growth was observed. The bridge was again repaired recently in the summer of 2005.</p> <p>A finite element study is performed in this study for a typical intermediate girder span, to characterize the behavior of fatigue critical details and to evaluate the effectiveness of the newly installed retrofits. A dual-level finite element analysis was performed using macro-level models of the entire bridge structure and micro-level models of some portions of the bridge under investigation. The finite element procedure was found to be efficient and accurate. The models were calibrated using field strain data obtained from two field tests done before and after the retrofits. The analytical results were in good agreement with the measured field data.</p> <p>The analysis shows that the top flange web gap region is the most susceptible to distortion-induced fatigue. The study successfully explains the observed crack patterns on the bridge. The study indicates a significant reduction in web gap stresses after the retrofit. The retrofit also reduces stresses in the gusset plate region and eliminates the stress concentration near the weld terminations. Based upon the most critical detail and assuming that the traffic volume doubles from the present ADTT of 65, the service life of the bridge is estimated to be over one hundred years.</p>			
17 Key Words Tuttle Creek, bridge, fatigue, steel girder, cracking, finite element method		18 Distribution Statement No restrictions. This document is available to the public through the National Technical Information Service, Springfield, Virginia 22161	
19 Security Classification (of this report) Unclassified	20 Security Classification (of this page) Unclassified	21 No. of pages 126	22 Price

FINITE ELEMENT ANALYSIS OF FATIGUE PRONE DETAILS OF THE TUTTLE CREEK BRIDGE

Final Report

Prepared by

Ashish Bhargava
W. M. Kim Roddis, Ph.D., P.E.

A Report on Research Sponsored By

THE KANSAS DEPARTMENT OF TRANSPORTATION
TOPEKA, KANSAS

November 2007

© Copyright 2007, **Kansas Department of Transportation**

NOTICE

The authors and the state of Kansas do not endorse products or manufacturers. Trade and manufacturer's names appear herein solely because they are considered essential to the object of this report.

This information is available in alternative accessible formats. To obtain an alternative format, contact the Office of Transportation Information, Kansas Department of Transportation, 700 SW Harrison Street, Topeka, Kansas 66603-3745 or phone (785) 296-3585 (Voice) (TDD).

DISCLAIMER

The contents of this report reflect the views of the authors who are responsible for the facts and accuracy of the data presented herein. The contents do not necessarily reflect the views or the policies of the state of Kansas. This report does not constitute a standard, specification or regulation.

ABSTRACT

Many older steel girder bridges exhibit distortion-induced fatigue cracking at the cross-frame to girder connections. In a two-girder bridge like the Tuttle Creek Bridge there are no redundant load paths and this problem is of even greater concern. The primary girders of the bridge structure are fatigue critical elements and even when such cracks are relatively small they must be examined extensively. The Tuttle Creek Bridge, built in 1962, developed distortion-induced fatigue cracks in the web gap region. The crack prevention repairs of 1986 were not effective and continued crack growth was observed. The bridge was again repaired recently in summer of 2005.

A finite element study is performed in this study for a typical intermediate girder span, to characterize the behavior of fatigue critical details and to evaluate the effectiveness of the newly installed retrofits. A dual-level finite element analysis was performed using macro-level models of the entire bridge structure and micro-level models of some portions of the bridge under investigation. The finite element procedure was found to be efficient and accurate. The models were calibrated using field strain data obtained from two field tests done before and after the retrofits. The analytical results were in good agreement with the measured field data.

The analysis shows that the top flange web gap region is the most susceptible to distortion-induced fatigue. The study successfully explains the observed crack patterns on the bridge. The study indicates a significant reduction in web gap stresses after the retrofit. The retrofit also reduces stresses in the gusset plate region and eliminates the stress concentration near the weld terminations. Based upon the most critical detail and

assuming that the traffic volume doubles from the present ADTT of 65, the service life of the bridge is estimated to be over hundred years.

TABLE OF CONTENTS

Abstract	iii
Table of Contents	v
List of Figures	viii
List of Tables	xii
Chapter 1: Introduction	1
1.1 General	1
1.2 Brief Description of the Bridge Structure	3
1.3 History of Fatigue Cracking	3
1.3.1 Web Gap Cracking	3
1.3.2 Gusset-Plate Cracking	4
1.3.3 Longitudinal Stiffener Cracking	5
1.3.4 Cope Hole Cracking	5
1.3.5 “New” Crack	6
1.4 Objective	6
Chapter 2: Applied Finite Element Procedure	14
2.1 Submodeling	14
2.2 Coarse Models	15
2.2.1 Modeling Non-Composite Action	16
2.2.2 Boundary Conditions and Loading	16
2.2.3 Global Axes Orientation and Sign Convention	17
2.3 Submodels	18
2.3.1 Top Connection Submodels	18
2.3.2 Bottom Connection Submodels	19
2.4 Calibration Method	19
Chapter 3: Overall Bridge Behavior	23
3.1 Composite Action	24
3.2 Cross-Frame Gages	25
3.3 Summary	26
Chapter 4: Top Connection Analysis	35

4.1	Top Flange Web Gap	35
4.1.1	Pre-1986 Web Gap Geometry.....	35
4.1.2	Pre-Retrofit FE Analysis.....	37
4.1.3	Post-Retrofit FE Analysis	38
4.2	Top Flange Connection Model Calibration.....	40
4.2.1	Comparison with Pre-Retrofit Field Test.....	40
4.2.2	Comparison with Post-Retrofit Field Test.....	42
4.2.3	Calibrated FE Model.....	43
4.2.4	Effectiveness of the Stop Hole Repair	44
4.3	Effect of Type ‘A’ Retrofit on Top Flange Stresses	45
4.4	Fatigue Life	46
4.5	Summary	48
Chapter 5: Bottom Connection Analysis.....		65
5.1	Bottom Flange Web Gap.....	65
5.1.1	Pre-Retrofit FE Analysis.....	65
5.1.2	Post-Retrofit FE Analysis	66
5.2	Bottom Flange Connection Model Calibration	67
5.2.1	Comparison with Pre-Retrofit Field Test Data.....	67
5.2.2	Comparison with Post-Retrofit Field Test Data.....	68
5.3	Bottom Flange-to-Gusset Plate Connection.....	69
5.3.1	Pre-Retrofit FE Analysis.....	69
5.3.2	Post-Retrofit FE Analysis	69
5.4	Gusset Plate Connection Calibration.....	70
5.4.1	Comparison with Pre-Retrofit Field Test Data	70
5.4.2	Comparison with Post-Retrofit Field Test Data.....	71
5.5	Summary	72
Chapter 6: Analysis of Cope Hole		83
6.1	Description	83
6.2	FE Analysis	83
6.2.1	Results.....	83
6.2.1.1	Comparison of Results for the Cope Hole Submodels	84

6.2.1.2	Simply Supported Beam With a Cope at Mid-Span.....	85
6.3	Summary	86
Chapter 7: Analysis of “New” Horizontal Crack		94
7.1	Description	94
7.2	FE Analysis	94
7.2.1	Through Crack with Stop Holes	94
7.2.1.1	Comparison with Fisher’s Formula	95
7.2.2	Outside Stiffener	96
7.3	Summary	96
Chapter 8: Conclusions		103
References		107

LIST OF FIGURES

Figure 1.1: Tuttle Creek Bridge	7
Figure 1.2: Bridge Cross-Section	7
Figure 1.3: Girder Details of a Typical Intermediate Span.....	8
Figure 1.4: Framing Plan of the Structure	9
Figure 1.5: Out-of-Plane Distortion of the Unstiffened Web Gap.....	10
Figure 1.6: Pre-1986 Web Gap Crack Patterns and Repair Procedure.....	10
Figure 1.7: Horizontal and Horseshoe Type Cracks, [Marshall et.al., 2005].....	11
Figure 1.8: Post-1986 Retrofit Horizontal Crack Growth	11
Figure 1.9: Post-1986 Retrofit Horseshoe Crack Growth	12
Figure 1.10: Gusset Plate Crack Patterns	12
Figure 1.11: Gusset Plate Weld Tear, [Marshall et.al., 2005].....	13
Figure 1.12: Cope Hole Crack Patterns.....	13
Figure 2.1: Coarse Models	20
Figure 2.2: Coupling of Nodes to Model Non-Composite Action	20
Figure 2.3: Coarse Model Truck Moving Direction	21
Figure 2.4: Coarse Model vs. Submodel	22
Figure 3.1: Location of Flange Gages, G9 and G10.....	28
Figure 3.2: Variation of Girder Longitudinal Stress, SZ, With Depth Obtained From FEA for Noncomposite Model.....	29
Figure 3.3: Variation of Girder Long. Stress, SZ, With Depth Obtained From Test.....	29
Figure 3.4: Frame Member Used for Comparison of Composite and Noncomposite Models.....	30
Figure 3.5: Variation of Girder Longitudinal Stress, SZ, With Depth Obtained From FEA for Composite Model	31
Figure 3.7: Comparison of SY Stress Contours for Submodel TR for Composite and Noncomposite Global Models.....	32
Figure 3.8: Location of Frame Gages, G11 to G16	33
Figure 3.9: Location of Frame Gages, G17 to G20	34

Figure 4.1: Pre-1986 Top Connection Submodel, B2W	49
Figure 4.2: Stress Variation in Pre-1986 Top Flange Web Gap	49
Figure 4.3: Truck Position for Load Case # 21	50
Figure 4.4: Out-of-Plane Displacement in Pre-1986 Top Flange Web Gap.....	50
Figure 4.5: SX Stress Contours in Pre-1986 Top Flange Web Gap	51
Figure 4.6: SY Stress Contours in Pre-1986 Top Flange Web Gap	51
Figure 4.7: SZ Stress Contours in Pre-1986 Top Flange Web Gap	52
Figure 4.8: Variation of Web Gap Stress Across the Stiffener Plate in Pre-1986 Top Flange Web Gap	52
Figure 4.9: Pre-Retrofit Top Connection Submodel, TNR	53
Figure 4.10: SX Stress Contours in Pre-Retrofit Top Flange Web Gap.....	53
Figure 4.11: SY Stress Contours in Pre-Retrofit Top Flange Web Gap.....	53
Figure 4.12: SZ Stress Contours in Pre-Retrofit Top Flange Web Gap.....	54
Figure 4.13: Out-of-Plane Displacement in Pre-Retrofit Top Flange Web Gap.....	55
Figure 4.14: Type 'A' Repair for Top Flange Connection	56
Figure 4.15: Post-Retrofit Top Connection Submodel, TR	57
Figure 4.16: SX Stress Contours in Post-Retrofit Top Flange Web Gap	57
Figure 4.17: SY Stress Contours in Post-Retrofit Top Flange Web Gap	58
Figure 4.18: SZ Stress Contours in Post-Retrofit Top Flange Web Gap	58
Figure 4.19: Out-of-Plane Displacement in Post-Retrofit Top Flange Web Gap	59
Figure 4.20: Location of Top Flange Web Gap Gages, G1 to G4	60
Figure 4.21: Calibrated Top Connection Submodel, TRC	61
Figure 4.22: SY Stress Contours in Calibrated Post-Retrofit Top Web Gap FE Model .	61
Figure 4.23: Calibrated Top Connection Submodel With Stop Hole, TRCH.....	62
Figure 4.24: SY Stress Contours in Calibrated Post-Retrofit Top Web Gap FE Model With Stop Holes.....	62
Figure 4.25: Stop Hole Retrofit proposed by Fisher et. al.....	63
Figure 4.26: SX and SZ Stress Contours in Top Flange For Pre-Retrofit Model (TNR)	63
Figure 4.27: SX and SZ Stress Contours in Top Flange For Post-Retrofit Model (TR)	64
Figure 5.1: Pre Repair Bottom Connection Submodel, BNR	73
Figure 5.2: Stress Variation in Bottom Web Gap Model (BNR)	73

Figure 5.3: Truck Position for Load Case # 22	74
Figure 5.4: SX Stress Contours in Pre-Retrofit Bottom Flange Web Gap	74
Figure 5.5: SY Stress Contours in Pre-Retrofit Bottom Flange Web Gap	75
Figure 5.6: SZ Stress Contours in Pre-Retrofit Bottom Flange Web Gap.....	75
Figure 5.7: Out-of-Plane Displacement in Pre-Retrofit Bottom Flange Web Gap.....	76
Figure 5.8: Type 'B' Repair for Bottom Flange Connection	76
Figure 5.9: SX Stress Contours in Post-Retrofit Bottom Flange Web Gap.....	77
Figure 5.10: SY Stress Contours in Post-Retrofit Bottom Flange Web Gap.....	77
Figure 5.11: SZ Stress Contours in Post-Retrofit Bottom Flange Web Gap.....	78
Figure 5.12: SZ Stress Contours in Post-Retrofit Bottom Flange Web Gap.....	78
Figure 5.13: Out-of-Plane Displacement in Post-Retrofit Bottom Flange Web Gap	79
Figure 5.14: Location of Bottom Flange Web Gap Gages, G5 to G8	80
Figure 5.15: SX and SZ Stress Distribution in Pre-Retrofit Bottom Flange-to-Gusset Connection	81
Figure 5.16: SX and SZ Stress Distribution in Post-Retrofit Bottom Flange-to-Gusset Connection	81
Figure 5.17: Location of Gusset Plate Gages.....	82
Figure 6.1: Type 'D' Repair	87
Figure 6.2: Global Model Showing the Location of the Cope Hole Submodel.....	87
Figure 6.3: Cope Hole Submodel With Radius 1½ inch, Model CP150.....	88
Figure 6.4: Global Deflection at Load Case # 14.....	88
Figure 6.5: Vector Plot of Maximum Principal Stresses for Model CP150 LC#14	89
Figure 6.6: Maximum Principal Stress for Model CP075 LC#14	89
Figure 6.7: Maximum Principal Stress for Model CP150 LC#14	90
Figure 6.8: Maximum Principal Stress for Model CP200 LC#14	90
Figure 6.9: Maximum Principal Stress for Model CP250 LC#14	91
Figure 6.10: FE Models for Simply Supported Beam With a Cope at Mid-Span	91
Figure 6.11: Maximum principal Stress for Model BM075.....	92
Figure 6.12: Maximum principal Stress for Model BM150.....	92
Figure 6.13: Maximum principal Stress for Model BM250.....	93
Figure 7.1: New Crack Observed in June 2005.....	98

Figure 7.2: Submodel TRNC 98

Figure 7.3: SX Stress Contours in Top Web Gap After Including a 4" Through Crack .. 99

Figure 7.4: SY Stress Contours in Top Web Gap After Including a 4" Through Crack .. 99

Figure 7.5: SZ Stress Contours in Top Web Gap After Including a 4" Through Crack. 100

Figure 7.6: Top Web Gap Submodel With Outside Stiffener, TRO 100

Figure 7.7: SX Stress Contours in Top Web Gap After Incl. an Outside Stiffener. 101

Figure 7.8: SY Stress Contours in Top Web Gap After Incl. an Outside Stiffener. 101

Figure 7.9: SZ Stress Contours in Top Web Gap After Incl. an Outside Stiffener. 102

LIST OF TABLES

Table 3.1: Comparison of Stress in Top and Bottom Flange from FEA with Field Tests	24
Table 3.2: Comparison of Cross-Frame Member Stresses from FEA with Field Tests	26
Table 4.1: Pre and Post Retrofit Peak FEA Stresses in Top Flange Web Gap	40
Table 4.2: Peak Stresses Obtained from TNR Models at B2W and B2E	41
Table 4.3: Pre-Retrofit Top Web Gap Stresses Obtained from Field Test Data and FE Analysis	41
Table 4.4: Post-Retrofit Top Web Gap Stresses Obtained from Field Test Data and FE Analysis	42
Table 4.5 Post-Retrofit Top Web Gap Stresses Obtained from field Test Data and Calibrated FE Analysis	44
Table 4.6: Pre-Retrofit and Post-Retrofit Top Web Gap Peak Stresses Obtained from Extrapolated Gage Values and FE Analysis	44
Table 4.7: Top Flange SX and SZ Stresses Before and After Retrofit	46
Table 4.8: Fatigue Life of the Bridge	47
Table 5.1: Pre and Post Retrofit Peak FEA Stresses in Bottom Flange Web Gap	67
Table 5.2: Pre-Retrofit Bottom Web Gap Stresses Obtained from Field Test Data and FE Analysis	68
Table 5.3: Post-Retrofit Bottom Web Gap Stresses Obtained from Field Test Data and FE Analysis	68
Table 5.4: Comparison of Pre-Retrofit and Post-Retrofit Top Web Gap Peak Stresses Obtained from Extrapolated Gage Values with FE Analysis	68
Table 5.5: Pre and Post Retrofit Peak FEA Stresses in Bottom Flange-to-Gusset Connection	70
Table 5.6: Pre-Retrofit Gusset Plate Stresses Obtained from Field Test Data and FE Analysis	71
Table 5.6: Pre-Retrofit Gusset Plate Stresses Obtained from Field Test Data and FE Analysis	72
Table 6.1: Maximum Principal Stress Around the Cope for LC # 14	84
Table 6.2: Maximum Principal Stress Around the Cope in a Simply Supported Beam	85

Table 7.1: Stresses at the slot end (point 1) and at the crack tip (point 2).....	95
Table 7.2: Stresses at the Slot End (point 1) Before and After Including the Outside Stiffener.....	96

CHAPTER 1: INTRODUCTION

1.1 General

Welded steel structures designed in the 1950's and 60's did not account for the possibility of fatigue cracking occurring from out-of-plane bending. Cyclic out-of-plane bending stresses result in relative rotation and displacement between longitudinal girders and transverse members framing into these girders, generally through stiffeners on the longitudinal members. These stresses lead to fatigue cracks.

This type of cracking has been observed in numerous structures across the nation and various "fixes" have been used to retard and/or fix the cracking. NCHRP Report 336 [Fisher et. al., 1986] documents this type of cracking. Unfortunately, the solution to these various types of cracking is dependent upon the particular detail in a given structure. Such is the case as has been observed by KDOT personnel on Bridge No. 16-81-2.25(017) by various inspections from the bridge management section.

The design of connections between lateral bracing, cross-frames, and primary bridge girders is a critical part of bridge design, as is the termination of longitudinal stiffeners. These issues are of even greater concern for a two-girder structure such as the Tuttle Creek Bridge. Since a two-girder bridge lacks redundant load paths, the primary girders are Fracture Critical Elements. This means that details prone to develop fatigue cracks, such as the connections and terminations called out above, are of special concern for the Tuttle Creek Bridge.

The connections between lateral bracing, cross-frames, and primary bridge girders of the types used on the Tuttle Creek Bridge are known to be susceptible to out-of-plane distortion induced cracking. A cross-section cut across the roadway of the

bridge would show a box-like structure composed of the girder webs as the vertical sides, the deck as the upper horizontal side, and the lateral bracing as the lower horizontal side. The cross-frames provide bracing from corner to corner of this box to prevent racking. The problem is that this simple description, and the design philosophy in practice at the time of engineering the Tuttle Creek Bridge, fails to account for the complex three-dimensional behavior of the actual bridge structure under traffic. The twisting response of the box to traffic loading, such as a truck in one lane, causes strains to be imposed on the girder web at these connections. While these may appear to be “stiff” connections, they act as part of a structural system that is flexible. Cyclic stresses and strains are induced from differential bending of the girders along their axis, together with twisting of the box-like cross-section.

The problem with this bridge, and other steel girder bridges of this vintage, is a localized phenomenon. A three dimensional state of stress exists where the girder web acts as a restraint against relative movements of the end of the lateral bracing and cross-frames. The connection is welded and provides what appears to be a stiff connection. The girder stresses induced from its flexural bending combine with the torsional stresses caused by the connections. These present a three-dimensional state of stress where the stresses in the girder are magnified by the significant stress from the lateral bracing and cross-frames. The resulting principal tensile stresses may be substantially larger than those determined by analysis of the stress components.

The situation is made worse by the fact that the members are subject to cyclic loads and stresses from traffic. The fatigue situation can exaggerate any excessive

stress or strain problems that exist in the system and stresses that are acceptable in a monotonic loading may not be when applied cyclically over many years.

1.2 Brief Description of the Bridge Structure

The Tuttle Creek Bridge [KDOT Bridge No. 16-81-2.24(0.17)] built in 1962 carries road traffic over the Big Blue River (Tuttle Creek Reservoir). It is located on a traffic route with an AADT, in 2003, of 430 vehicles per day with 15% truck traffic. The structure, as shown in Figure 1.1, comprises of two longitudinal built-up steel girders with pin and hanger connection system consisting of 30 spans. The overall bridge length is 5350.1 ft. Figure 1.2 shows the cross section of the cross-section of the bridge. The roadway width is 28 ft. with two 12 ft. traffic lanes and two 2 ft. shoulders. Girder details of a typical intermediate span and the framing plan are shown in Figures 1.3 and 1.4. The concrete deck slab is non-composite. The cross-frame members are first bolted then welded to the connection stiffener. The stiffener is welded to the web plate and prior to any retrofits it was only snug fitted to the top and bottom flange.

The material specification for the main structural steel members is ASTM A373-54T and the expansion devices conform to ASTM A7-56T.

1.3 History of Fatigue Cracking

1.3.1 Web Gap Cracking

Prior to the 2005 retrofits the transverse connection plate was only snug fitted to the girder flanges. This created an unstiffened segment of the girder web, commonly referred to as the web gap. It was the primary site of fatigue cracks found on the bridge. Under live loads, the differential displacements of the two girders force the end of the transverse structural member to rotate, pulling the unstiffened web gap out-of-plane as

shown in Figure 1.5. This out-of-plane distortion creates high secondary stresses at the connection plate end leading to fatigue cracking. Cracks developed at both the web-to-flange and web-to-connection plate fillet welds, typically as horizontal or horseshoe cracks, as indicated in Figure 1.5. Cracks are mostly located in the positive moment regions because of large differential girder deflections occur at the mid spans. Cracks are more frequent at the girder top flanges. This is because the top flange is restrained to rotation and lateral movement by the concrete deck. The bottom flanges are relatively much less constrained and are therefore less susceptible to distortion-induced fatigue cracking. Figures 1.6 and 1.7 show the two distinct crack patterns, Type A horizontal cracks and Type B horseshoe cracks, observed on the bridge in the top web gap. A total of 379 horseshoe type cracks and 291 horizontal type cracks were found on the bridge [Marshall et. al., 2005].

In 1986, KDOT performed retrofits at all the transverse connection plates as shown in Figure 1.6. In this fix, the high constraint web gap region was made flexible by cutting back the connection plate by 4 in. and providing a smooth transition of 0.5 in radius fillet. Burr free holes were also drilled at all the crack tips. The repair was, however, not effective and fatigue critical inspections in 2000 reported continuous crack growth at the end of stiffener plate and reinitiation from stop holes, as shown in Figures 1.8 and 1.9.

Detailed analysis of a typical top connection is presented in Chapter 4.

1.3.2 Gusset-Plate Cracking

In addition to the web gap region, cracks were also found within the gusset plate connection. Two types of crack were observed: cracking was observed in the gusset-

flange fillet welds perpendicular to the girder and the tack welds parallel to the girder. The two crack patterns are shown Figures 1.10 and 1.11. Both the types of cracks were only weld tears and did not propagate into the girder flange. The first type of crack was found mostly at weld terminations along the sides of the gusset plate. The second type was in the tack weld placed on the underside of the gusset plate. The cracks are believed to be caused by the prying action of the bracing members under the action of traffic loads.

Detailed analysis of bottom connection is presented in Chapter 5.

1.3.3 Longitudinal Stiffener Cracking

Cracks were observed in the butt welds of the stiffener splices. The cracks were found only in the weld material and they did not propagate into the parent material. Details of the cracks were not present in the inspection reports, so a detailed analysis similar to web gap and gusset plate regions could not be performed. The termination of longitudinal is a fatigue prone detail. However, no cracks were found on the bridge. A detailed analysis of the stiffener termination was performed at KU and a retrofit strategy was recommended as a preventive measure.

1.3.4 Cope Hole Cracking

Cracks were found at the rim of weld access holes present on the bridge at the field splices, see Figure 1.12. The cracks originated from the splice weld and they propagated into the girder web plate. As discussed later in this report, the cope hole is located in a low stress field region. Initial defect at the weld is the most likely cause of this crack. Detailed analysis of a typical cope hole is presented in Chapter 6.

1.3.5 “New” Crack

During a site inspection of September 2005 a horizontal crack was found at the fourth cross-frame of span 14. The crack originated at cope end of the stiffener clip. It was not a through thickness crack and was detected by a Magnetic Particle test. The crack is not a typical distortion-induced fatigue crack. It is believed to be originated at a mill flaw. A Detailed analysis of this crack is presented in Chapter 7.

1.4 Objective

The objective of this study is to analyze and identify the sources of fatigue cracking found on the bridge and to assess the effectiveness of the installed retrofits. The connection details are modeled and analyzed using Finite Element (FE) based method utilizing three dimensional isoparametric elements. This report addresses the results of these analyses and model calibration using the two field investigations done before and after the retrofits.



Figure 1.1: Tuttle Creek Bridge

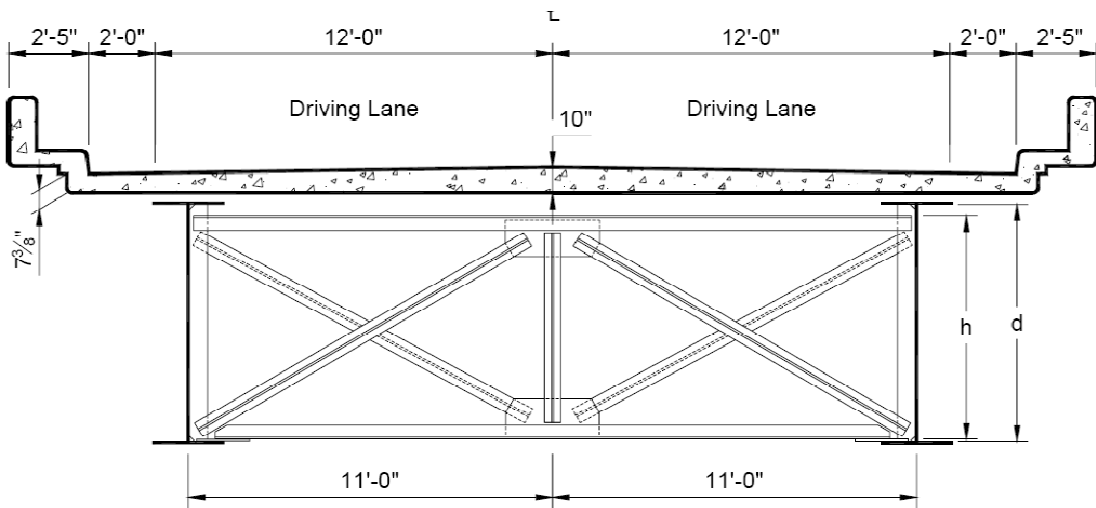


Figure 1.2: Bridge Cross-Section

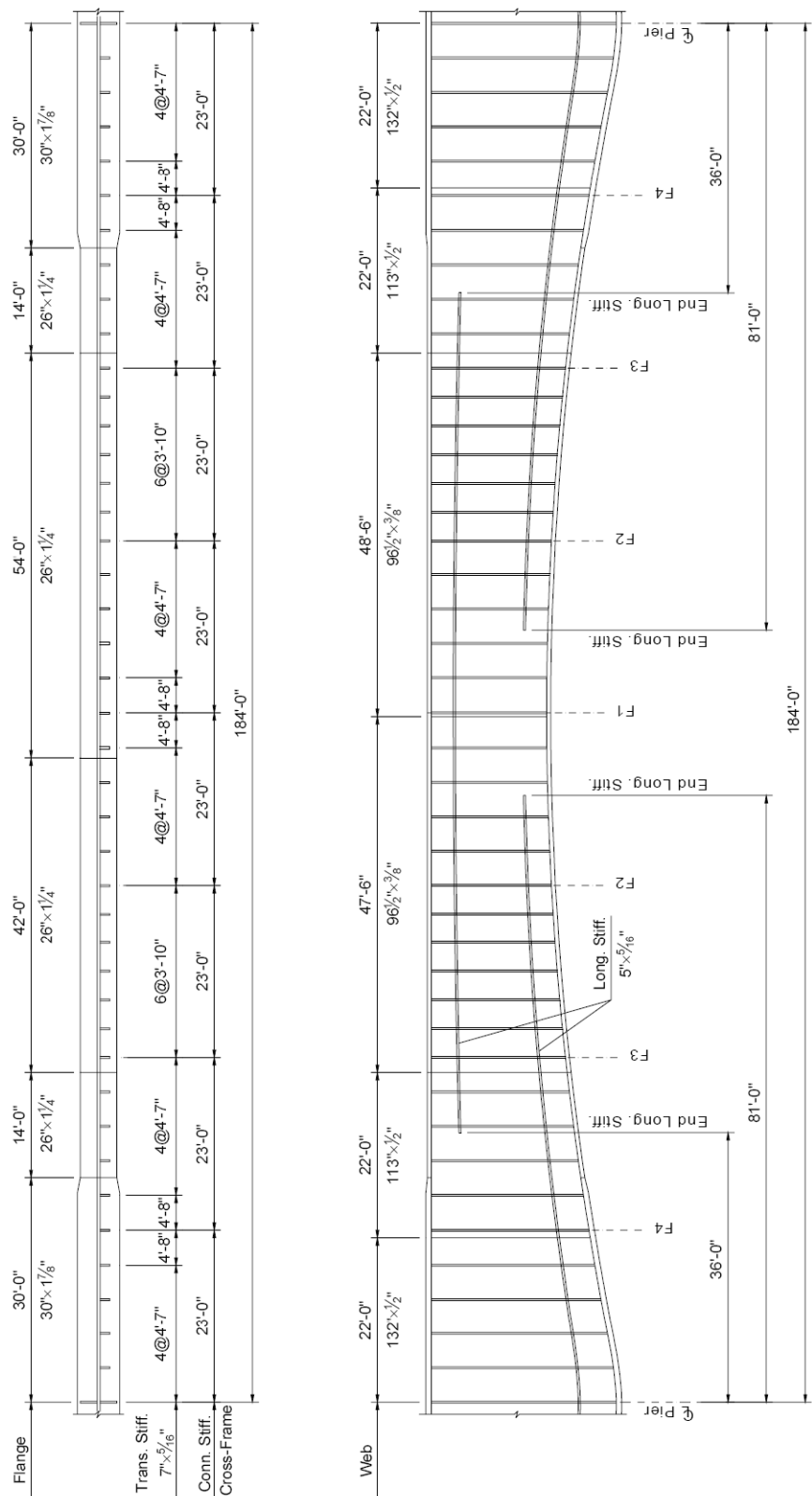


Figure 1.3: Girder Details of a Typical Intermediate Span

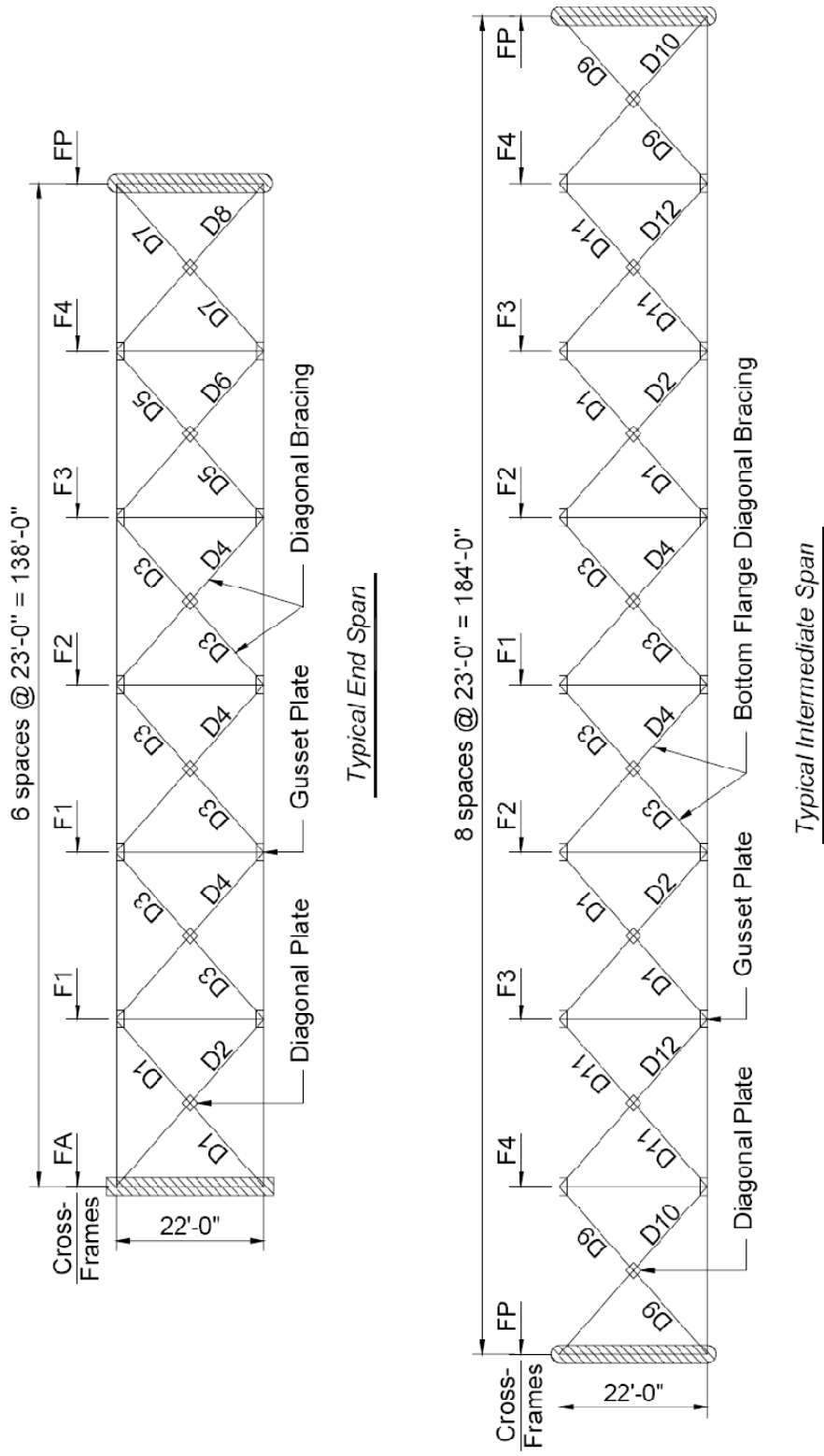


Figure 1.4: Framing Plan of the Structure

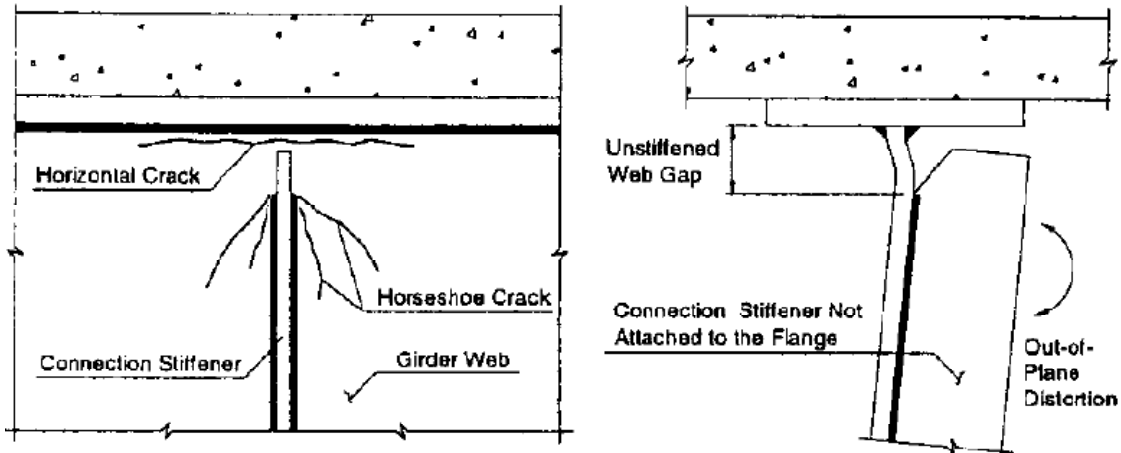


Figure 1.5: Out-of-Plane Distortion of the Unstiffened Web Gap [Roddis and Zhao, 2003]

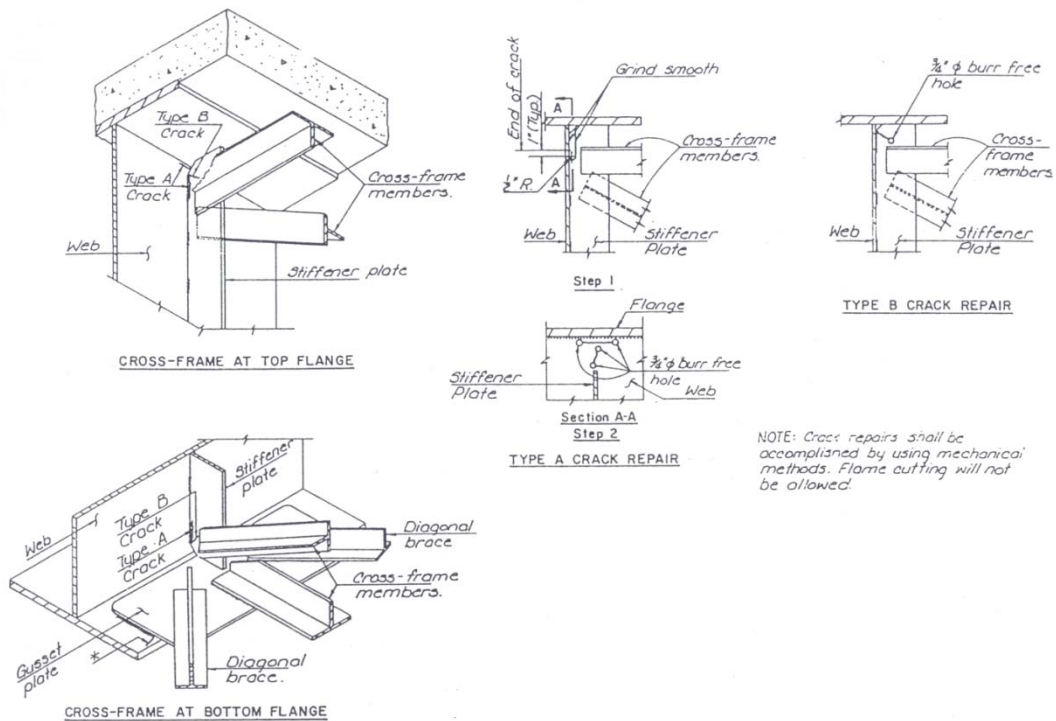


Figure 1.6: Pre-1986 Web Gap Crack Patterns and Repair Procedure

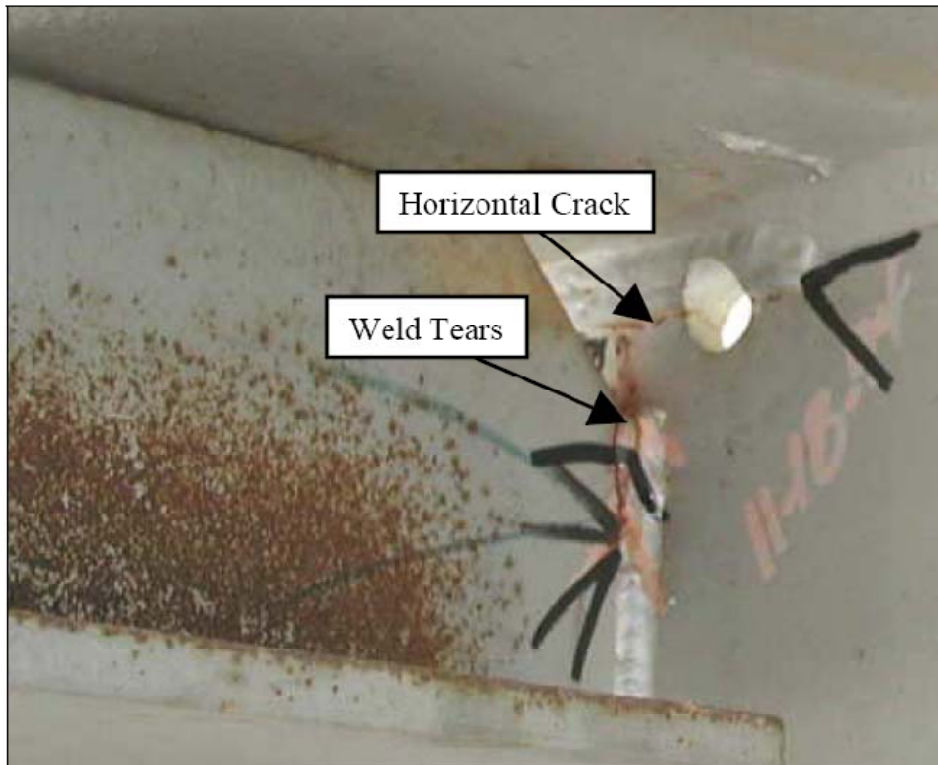


Figure 1.7: Horizontal and Horseshoe Type Cracks, [Marshall et.al., 2005]

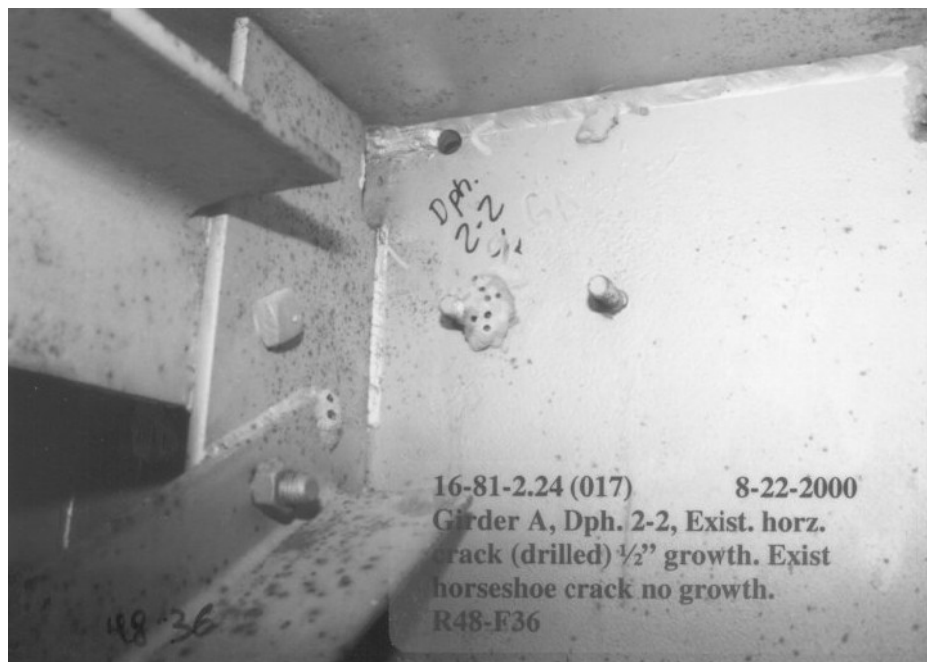


Figure 1.8: Post-1986 Retrofit Horizontal Crack Growth

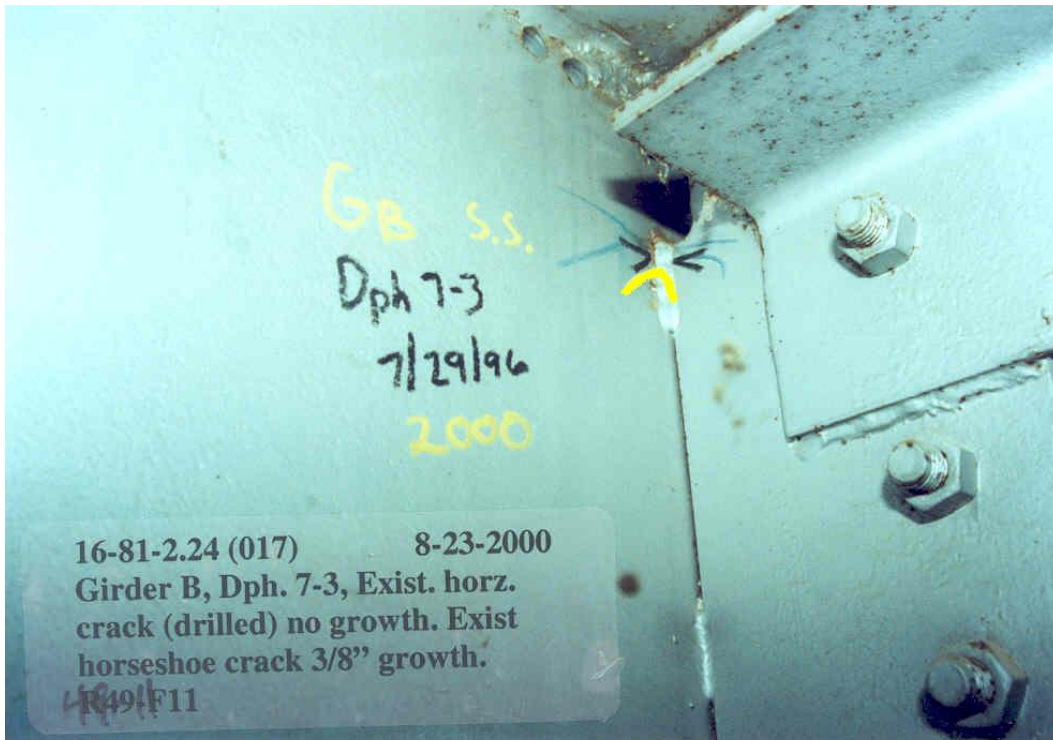


Figure 1.9: Post-1986 Retrofit Horseshoe Crack Growth

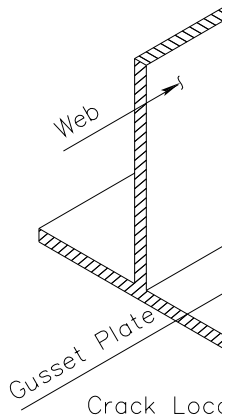


Figure 1.10: Gusset Plate Crack Patterns

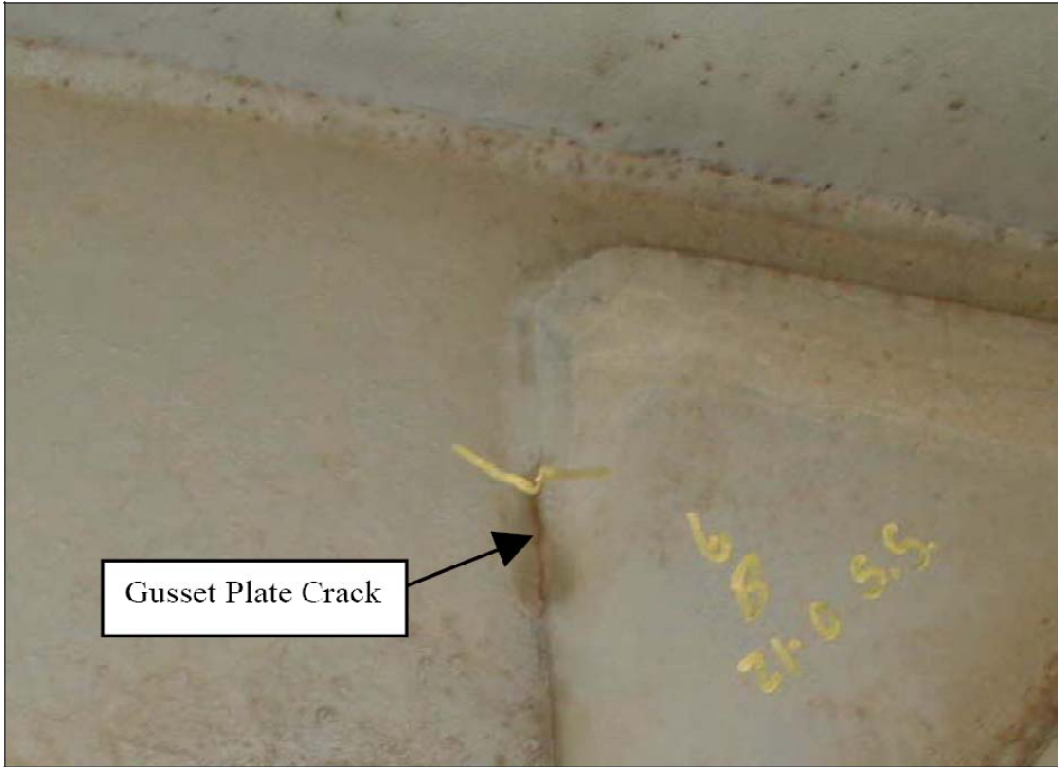


Figure 1.11: Gusset Plate Weld Tear, [Marshall et.al., 2005]

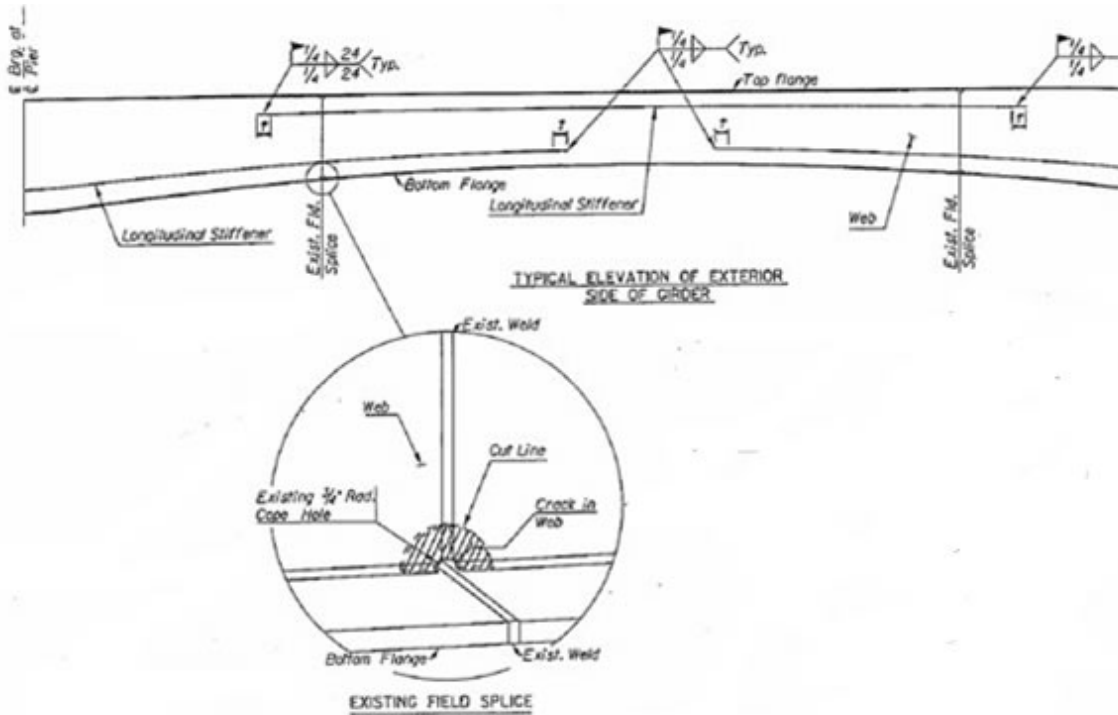


Figure 1.12: Cope Hole Crack Patterns

CHAPTER 2: APPLIED FINITE ELEMENT PROCEDURE

Out-of-plane displacement of the web gap induces secondary stresses over a small unstiffened portion of the girder web. These secondary stresses are not accounted for during analysis involved in a routine design. Current design specifications also do not identify procedures to estimate these secondary stresses. Finite Element (FE) based methods provide us a viable tool to estimate these stresses. Field investigations and experiments can also be used to estimate these secondary stresses [Connor and Fisher, 2005]; however, it is costlier to run physical experiments than to run numerical experiments. Another advantage of doing a finite element analysis is that the mathematical models can be easily updated to accommodate changes to geometry or loading environment. Finite element analyses based on multi-level modeling procedures are commonly applied and past studies utilizing these methods have reported good agreement between the analytical results and the experimental data [NCHRP 336, Li and Schultz, 2005, D'Andrea et.al., 2002]. This chapter introduces the FE modeling approach used in this study.

2.1 Submodeling

Finite element based methods are sensitive to element size. In order to properly characterize the stress field in regions of high stress gradient, it is required to use a finer mesh. However, the computational cost increases significantly with increasing number of elements. Multi-level methods minimize this cost by allowing use of independent finite element models with different levels of refinement for models as the region of interest is approached. A two-level modeling approach is used in this study: a large coarse model simulating the global structure behavior under the truck load, and the small local

submodel with relatively finer mesh to reveal the local stress field at the crack sensitive connection details. To link the analysis between the coarse model and the submodel appropriate data mapping process needs to be specified. The software used for this study is ANSYS 10.0 [2006] academic version, having an upper limit node number of 128,000. It has a submodeling tool called the Cut Boundary DOF (degrees of freedom) Interpolation, which maps the displacement results from the coarse model on the boundary nodes of the submodel.

Submodeling procedure is based on St. Venant's principle, which states that if an actual force distribution is replaced by a statically equivalent system, the distribution of stress and strain is altered only near the regions of load application. The principle implies if cut-off boundaries of the submodel are far enough from regions of localized stress concentration, reasonable accurate results can be obtained from the submodel. The results away from stress concentration regions are relatively stable and are not sensitive to change in mesh size. Therefore the extent of the boundary must be carefully defined so that the mapped displacements results from the coarse model can be correctly used and satisfactory stress results can be obtained in the region of interest.

2.2 Coarse Models

Finite element models used in this study are derived from the models built as part of previous research conducted at the University of Kansas by Dr. Yuan Zhao [Zhao, 2003]. Three coarse models are used in this study. Each model includes a typical intermediate span of the bridge, as shown in Figure 2.1. First coarse model (CM1) represents the pre-1986 bridge geometry. Second coarse model (CM2) represents the

post-1986 retrofit bridge geometry where top connection was modified to include a 4 in. web gap. The third model (CM3) represents the post-2005 retrofit bridge geometry where the softened top connection was stiffened by positively attaching the connection stiffener to the top flange. The connection was modeled by using rigid links between the stiffener nodes and the flange nodes at their intersection. Figure 2.1 shows the top connection details for the three coarse models. The deck slab is modeled by 8-node brick elements (ANSYS Solid45). The girder flanges, web, and stiffeners are modeled by 4-noded shell elements (ANSYS Shell181). The cross frame members and lateral bracings are modeled by 3-D spar elements (ANSYS Link 8).

2.2.1 Modeling Non-Composite Action

Coincident nodes are built at the girder top flange in contact with the bottom of the deck slab. To model the non-composite action, each pair of the coincident nodes is coupled for transverse and vertical DOFs while the longitudinal DOFs are left uncoupled as shown in Figure 2.2. This enables the deck surface to slide freely on the flange surface in the longitudinal direction but the motion is restricted in the vertical and the transverse direction. The details of non-composite behavior are discussed later in this report in Chapter 3.

2.2.2 Boundary Conditions and Loading

The girder and deck end sections are assumed to be fixed, to simulate the continuous support over the piers, so the deck, flange, and web nodes at the model end sections are restrained to all DOFs.

An HS15 truck with 10% wheel load increment of impact effect is considered for model loading. As shown in Figure 2.3, the truck is placed at the center of the

westbound lane close to Girder A. The truck is moved in increments of 5 ft. for a total of 40 load cases. In this study, the cross-frame to girder connections are named combining the girder designation, cross-frame type, and the location corresponding to the mid-span cross-frame F1. The structural response is expected to be axisymmetric about the intersection of the girder mid-span and the center of the roadway width when the same truck is applied close to Girder B (the eastbound lane). Therefore, only the bridge behavior under the westbound truck loading is investigated.

2.2.3 Global Axes Orientation and Sign Convention

The orientation of the axes with respect to the bridge model is shown in an isometric view in the top left corner of Figure 2.1. The bridge is modeled with its length being parallel to the global-Z direction. The transverse direction is global-X and the vertical direction is global-Y.

Stress range is the governing parameter to determine the fatigue life. Principal stresses are normally used to identify crack initiation locations in FE analysis. In this study, however, the FE models are built such that the potential crack path is oriented perpendicular to the axial stresses. This assumption was verified in a previous KDOT research study involving FE analysis of five KDOT bridges including the Tuttle Creek Bridge. It was shown to be consistent with fundamental fracture Mode 1 [Dowling, 1999] assumption that only the stress component normal to the crack path is responsible for crack growth. In this study, therefore, axial stresses are be used to identify the fatigue hot spots. In the stress distribution plots in the subsequent chapters SX represents the stress in the transverse direction, SY in the vertical direction, and SZ in the longitudinal direction. Positive values indicate tension and negative values indicate compression. All

the units in the distribution plots are in US customary units with length in inches (in.), force in kilopounds (kips), and stress in pounds per square inch (ksi)

2.3 Submodels

All the submodels are built using shell elements. The boundaries for all the submodels are located at half the average depth of the girder from top or bottom and 4 ft. either side from the stiffener. Figure 2.4 shows differences between the global and local models. The mesh is much finer in the submodel compared to the coarse model and the web gap geometry is modeled with a greater detail and the high stress concentration regions are meshed with finer mesh. Element size away from the region of concern was controlled within 1 in. which is about one-twelfth the element size used in the coarse model. For regions where the stress gradients are high mesh size was determined to obtain satisfactory convergence in the results and the size varied from 25in to 0.05in. The displacement results of the global coarse model were mapped onto the submodel boundary nodes. This process was automated using ANSYS feature and was repeated for all the load cases. Since only the displacements were mapped, the forces from the frame members were not applied automatically. For every load case, the member forces in the link elements were extracted and were applied as nodal forces at the corresponding node location in the submodel. The submodels are then analyzed for all the load cases to determine the maximum stresses.

2.3.1 Top Connection Submodels

Three submodels are used to study the top connection –

- Pre-1986 submodel designated as B2W
- Pre-Retrofit submodel designated as TNR (top no repair)

- Post-Retrofit submodel designated as TR (top repaired)
- Calibrated submodels TRC (top repaired calibrated) and TRCH (top repaired calibrated with holes)

The details of the submodels are discussed along with the analysis results in Chapter 4.

2.3.2 Bottom Connection Submodels

Two submodels are used to study the bottom connection –

- Pre-retrofit submodel designated as BNR
- Post-retrofit model designated as BR

The details are discussed along with the analysis results in Chapter 5.

2.4 Calibration Method

The strain data obtained from field tests are used to calibrate the FE models. Two tests were planned one before the retrofit and one after the retrofit. Detailed comparison of the field test results with FE results are given in Chapters 3, 4, and 5.

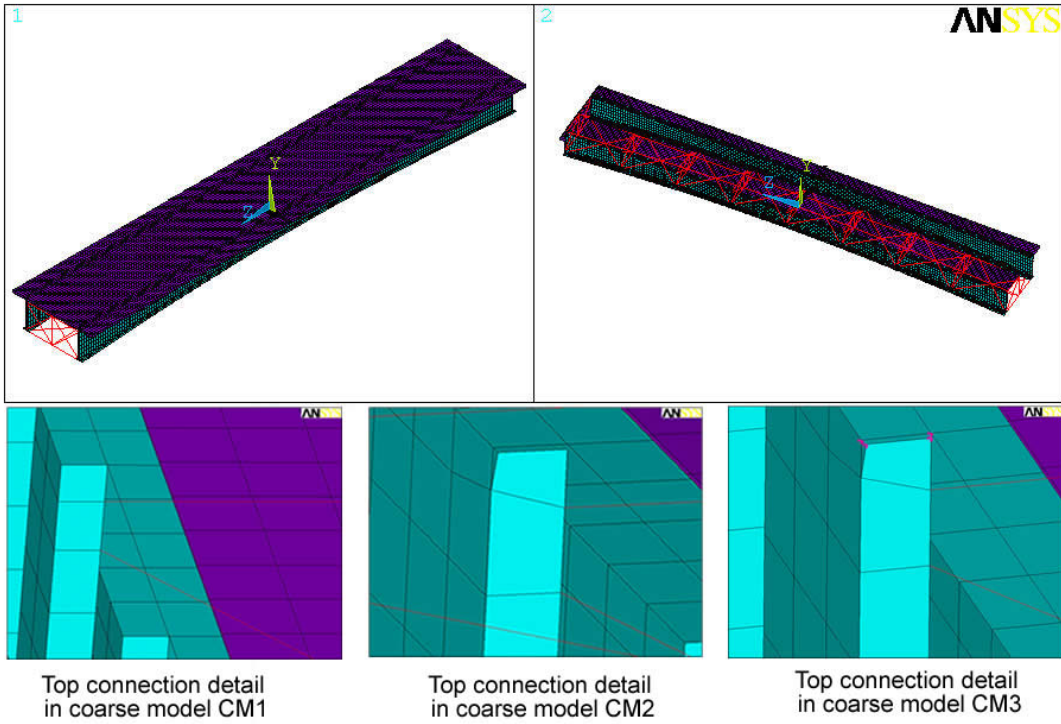


Figure 2.1: Coarse Models

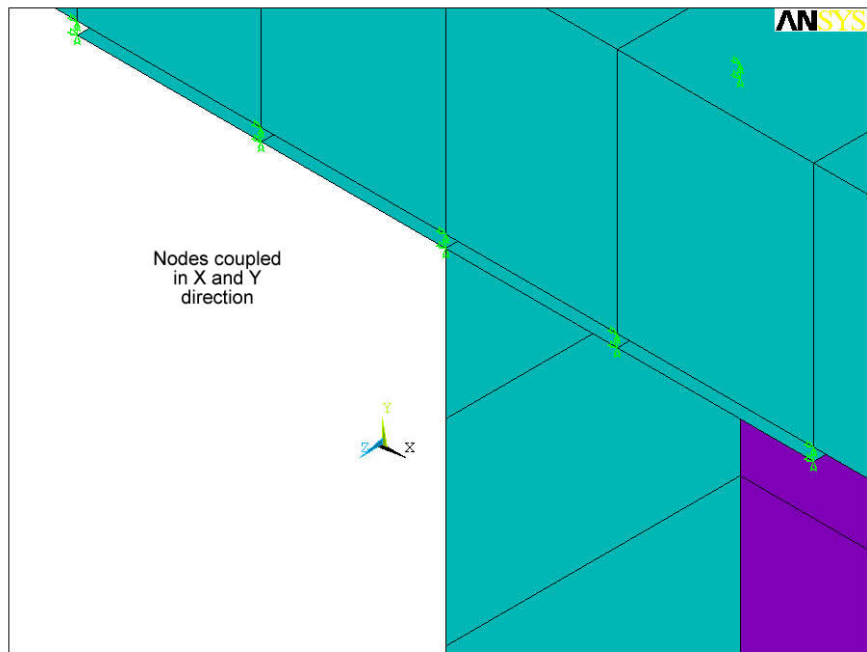


Figure 2.2: Coupling of Nodes to Model Non-Composite Action

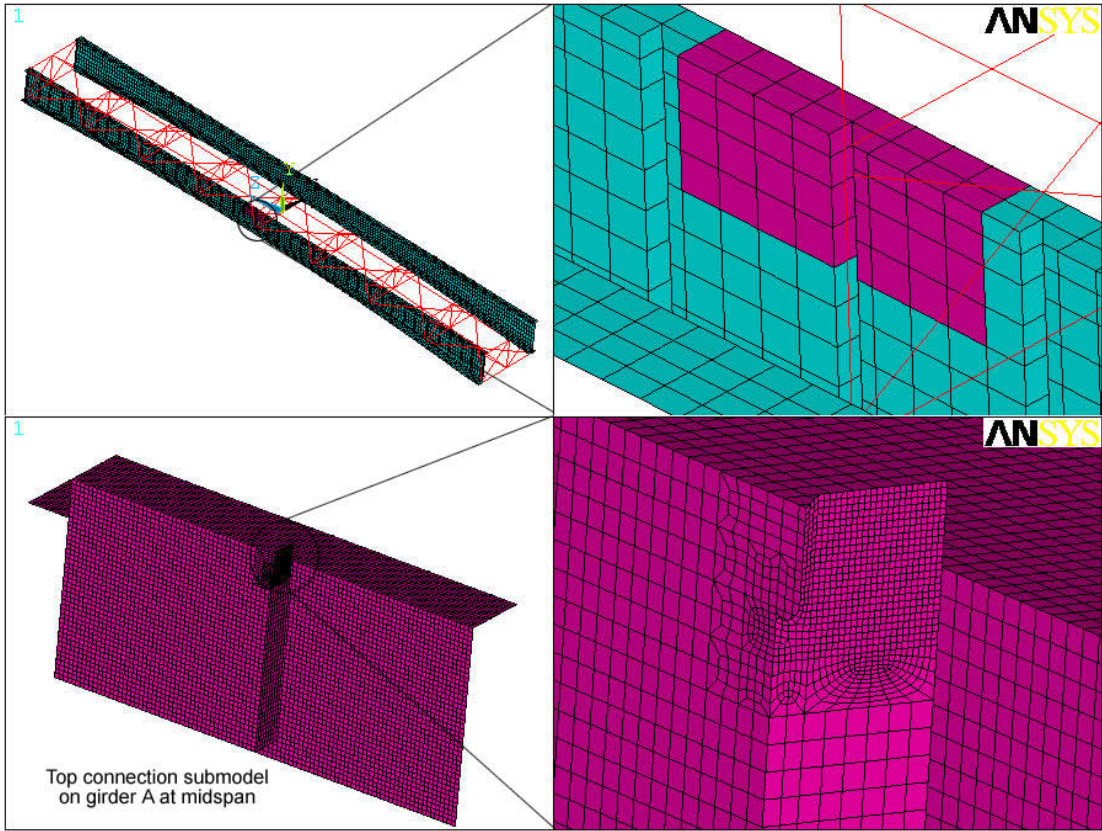


Figure 2.4: Coarse Model vs. Submodel

CHAPTER 3: OVERALL BRIDGE BEHAVIOR

A typical intermediate span was selected for this study. The coarse global FE model was built by including all the major structural components, the girders, deck slab, cross-frame members, web stiffeners, and the transverse connection plate. The submodel analyses are based on the results from this global FE model. Therefore it is essential that the assumptions made to build the FE model be validated.

The major concern in this study is the distortion induced fatigue cracking in the web gap. In the structure the load path that leads to out-of-plane distortion can be defined as: truck loading $\xrightarrow{(1)}$ deck slab $\xrightarrow{(2)}$ girders $\xrightarrow{(3)}$ cross frame $\xrightarrow{(4)}$ web gap. The global behavior will depend upon the degree of composite action, as indicated by first load step. When designed, the bridge was assumed to act noncompositely; however, large amounts of friction between the concrete deck slab and the flange can be expected to produce some degree of composite action. The fourth step represents the pull-action of the frame members to produce the out-of-plane distortion. The amount of out-of-plane distortion depends upon the forces in the cross frame members. Since the distortion occurs over a small segment of the web, a small change in out-of-plane displacement will cause significant change in web gap stress distribution. Therefore, it is essential that these forces are accurately calculated from the global FE model.

During the field tests gages were placed on top and bottom flanges near cross frame F-2 to estimate the degree of composite action. Gages were also placed on the cross-frame frame members to estimate the stresses that are transferred to the connection plate. Comparison of the field test data with the FE analysis results is presented in the following sections.

3.1 Composite Action

Gages (G9 and G10) were placed on the top and bottom flanges in the first phase of field investigations done prior to the retrofits. The gages were located close to the cross-frame F-2. Their exact location is shown in Figure 3.1. Gage G10 was damaged in the post-retrofit test and its strain data was not available. The gages were symmetrically placed about the centroid of the cross-section. If the girders were acting noncompositely, the top and the bottom flange will show equal strain magnitudes with opposite signs. Table 3.1 compares the stress at the gage locations.

Table 3.1: Comparison of Stress in Top and Bottom Flange from FEA with Field Tests

Location	Gage Number	Stress at Gage Location		(ksi)
		Pre-Retrofit Test	Post-Retrofit Test	FE Analysis
Upper Flange	G9	-0.6	-0.6	-0.02
Lower Flange	G10	2.8	-damaged-	0.02

The FE model was build assuming a noncomposite action which is reflected in the strain values being equal in magnitude and opposite in sign. However, the field data indicates that some degree of composite action is present. For the FE model the neutral axis is at half the dept of the section at cross-frame F2, which is approximately 43 inches from the top flange, see Figure 3.2. From the test data the neutral axis is estimated to be at a depth of 15 inches from the top flange, see Figure 3.3.

Previous studies on other KDOT bridges [Zhao 2003] have shown that the differences in composite versus noncomposite behavior of the bridge girders in major axis bending do not affect significantly the connection response to out-of-plane distortion. The reported errors are all below 10%. However, to verify this effect the global FE model is modified to include noncomposite action. Figure 3.4 shows the plot

of longitudinal stress, SZ , with depth of the girder section for the modified FE model. The depth of the neutral axis for the model is approximately 18 in. from the top flange which matches well with the experiment data.

The connection response to out-of-plane distortion is directly affected by stresses in the frame members. The axial stress in a frame member (see Figure 3.6) is obtained using both the noncomposite and composite global FE models. Figure 3.7 shows the comparison of the two analyses for all load cases. The maximum compressive stress in both the cases occurs at LC # 12. The maximum stress for the composite model is 18% lower than that for the noncomposite model. To evaluate the effect on local stresses, submodel TR (see section 2.3.1) is analyzed using both the models and for the most critical load case. Figure 3.7 compares the distribution of the vertical stress, SY , obtained from using the two models. The maximum tensile stress in the connection for a composite model is 20% lower than that for the noncomposite model. From these two comparisons, one at global level and the other at the submodel level, it can be concluded that considering the composite action does not alter the stress values significantly. Further, the errors caused in the estimates are on the conservative side. Therefore, the noncomposite global model will be used for analysis in the present study.

3.2 Cross-Frame Gages

The primary source of web gap stresses is the out-of-plane distortion caused by the pull of the frame members on the connection stiffener. It is therefore essential to estimate these pull stresses accurately. In the field test performed before the retrofits ten gages, G11 to G16 and G17 to G20, were placed on cross frames F2 and F3, respectively. The locations of these gages are shown in Figures 3.8 and 3.9. Gages

G13, G15, and G16 were relocated to new locations in the post-retrofit field tests. Table 3.2 gives the comparison of the FEA results with the two field test. The coarse models CM2 and CM3 (see section 2.2) are used to compare with the pre-retrofit and post-retrofit field data.

Table 3.2: Comparison of Cross-Frame Member Stresses from FEA with Field Tests

Gage Number	Stress at Gage Location (ksi)			
	Pre-Retrofit		Post-Retrofit	
	Test	FEA (model CM2)	Test	FEA (model CM3)
G11	1.1	0.4	2.1	1.0
G12	0.7	0.5	0.8	0.8
G13	-0.5	-0.5	-	-0.4
G14	-0.6	-0.3	-0.5	-0.4
G15	1.3	1.1	-	1.2
G16	0.8	0.4	-	0.5
G17	-0.5	-0.3	-0.3	-0.2
G18	-0.5	-0.1	-0.4	-0.2
G19	1.1	0.9	0.9	0.9
G20	-0.9	-1.1	-0.6	1.2

The stresses in the frame members are controlled more by the global behavior than by the localized stresses in the regions where the retrofits were applied. Consequently, the stresses in the frame members do not change significantly after the retrofits. The stresses derived from the measured strains are in good agreement with the calculated stress thus validating the accuracy of the FE model in predicting the brace forces.

3.3 Summary

The finite element models were built assuming noncomposite action, but the field data indicates that the bridge is acting compositely. The study shows that considering the noncomposite action in the analysis does not alter the stress distribution significantly and in addition that the stress estimates are conservative. Therefore, it is reasonable to assume noncomposite action of the bridge. The pre and post retrofit axial stresses in

the frame members are in good agreement with the finite element models thus validating the coarse models used in this study.

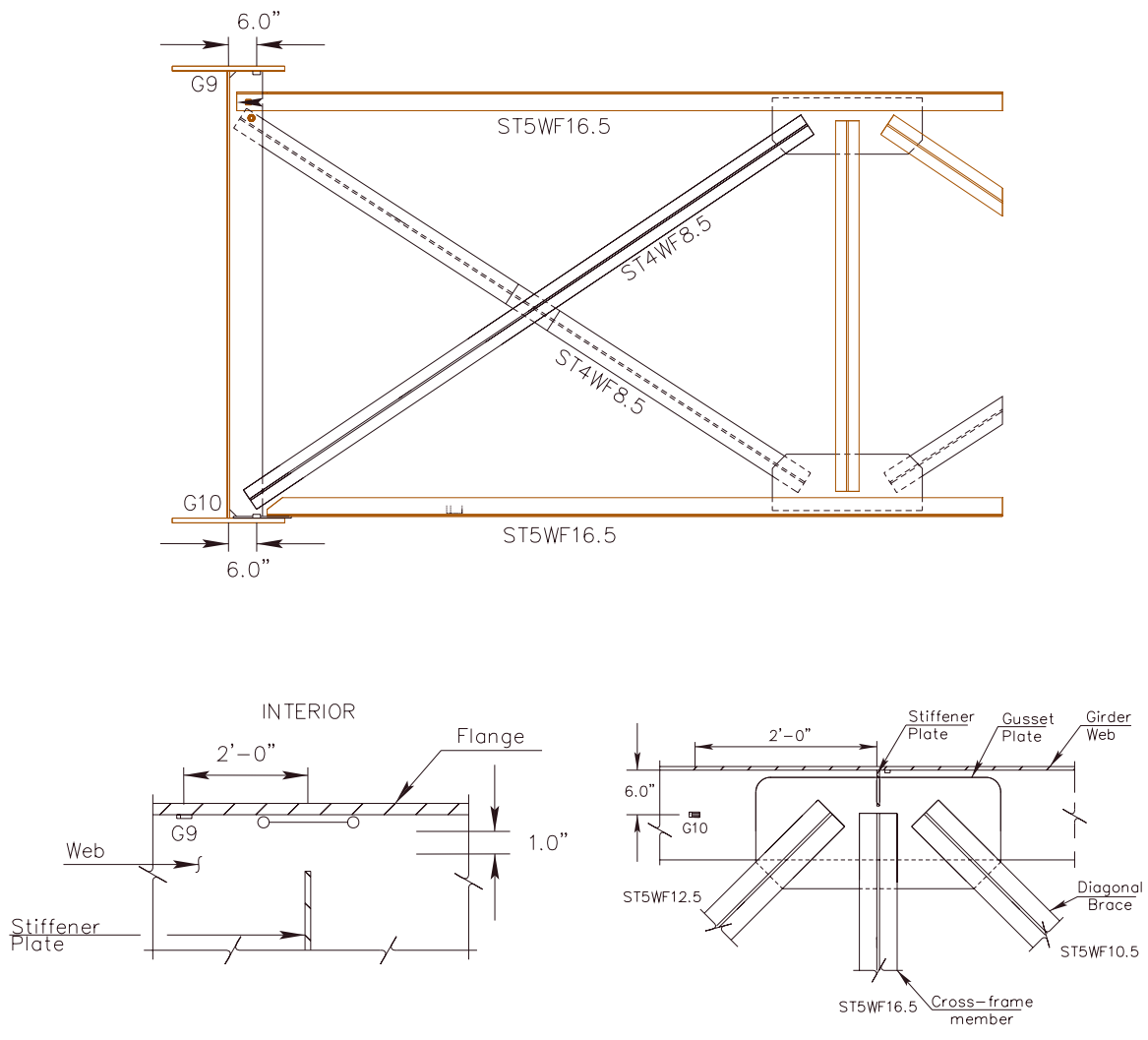


Figure 3.1: Location of Flange Gages, G9 and G10

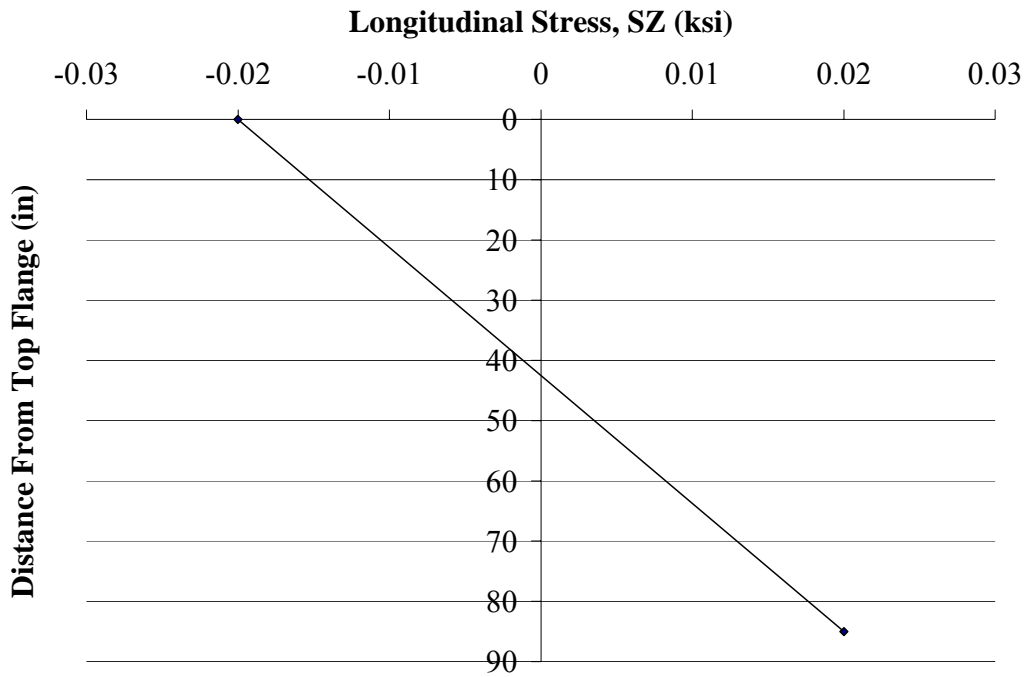


Figure 3.2: Variation of Girder Longitudinal Stress, SZ, With Depth Obtained From FEA for Noncomposite Model

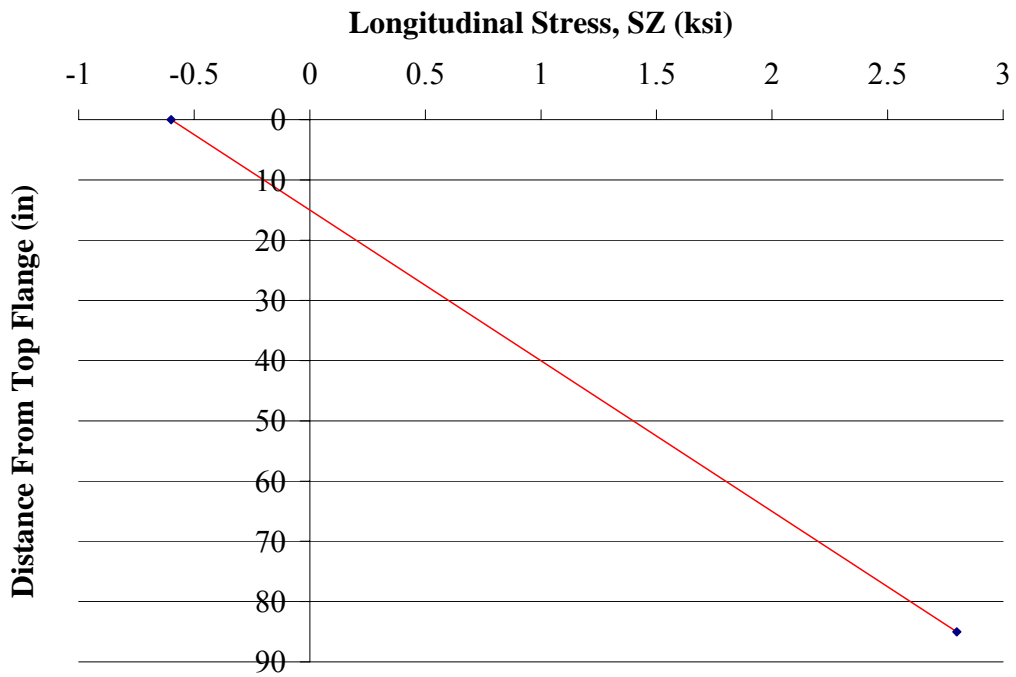


Figure 3.3: Variation of Girder Longitudinal Stress, SZ, With Depth Obtained From Test

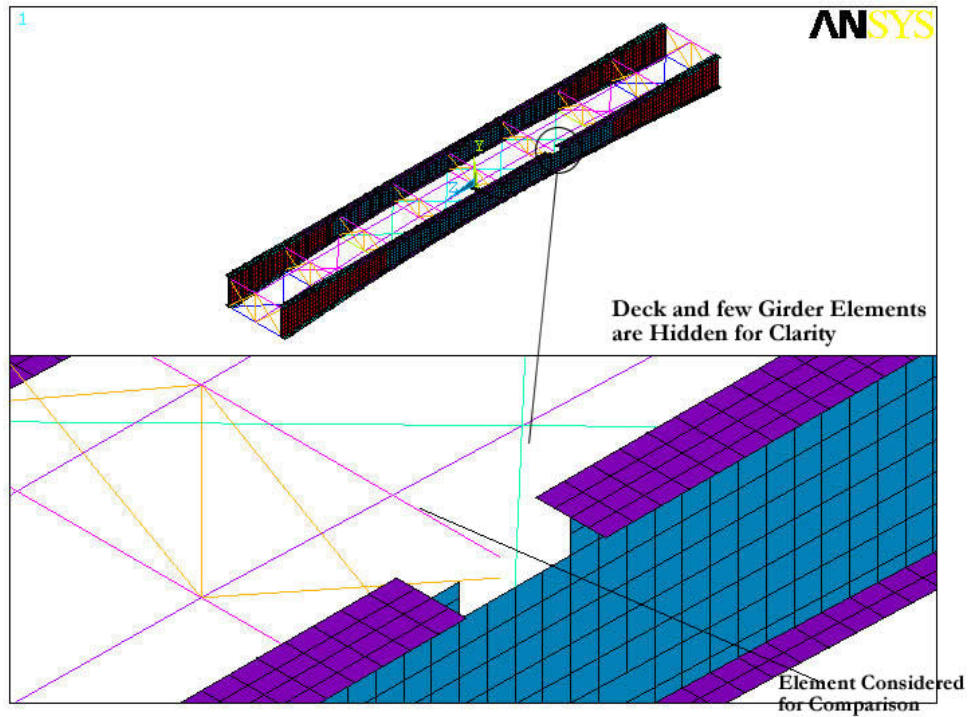


Figure 3.4: Frame Member Used for Comparison of Composite and Noncomposite Models

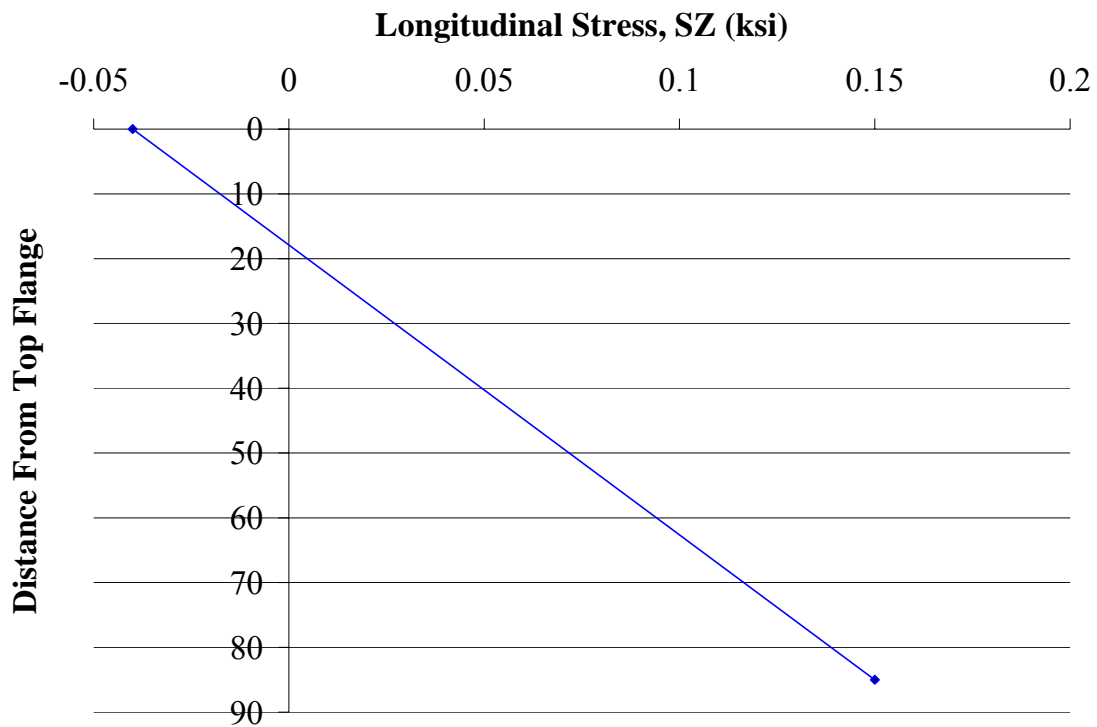


Figure 3.5: Variation of Girder Longitudinal Stress, SZ, With Depth Obtained From FEA for Composite Model

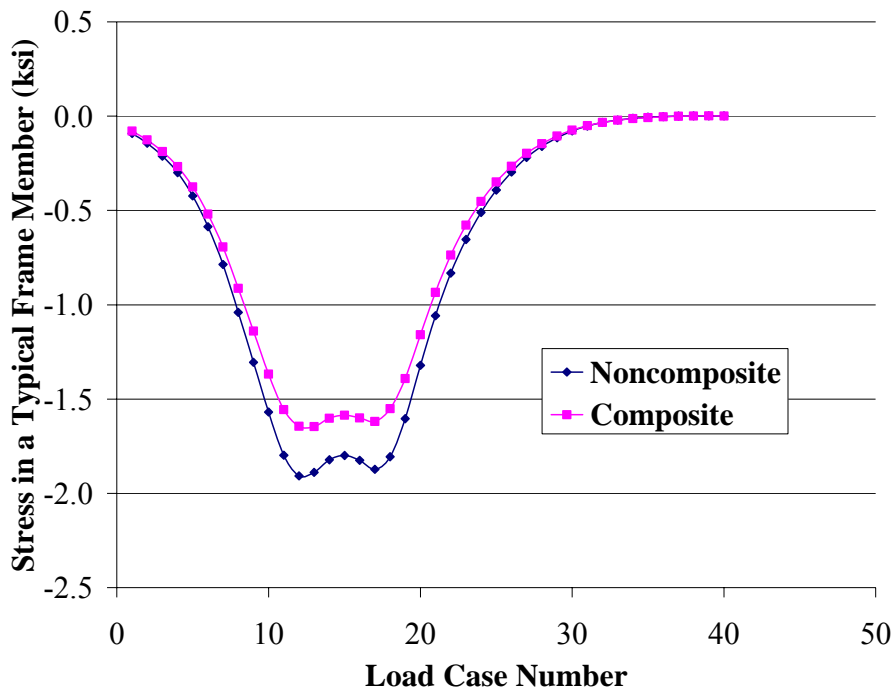
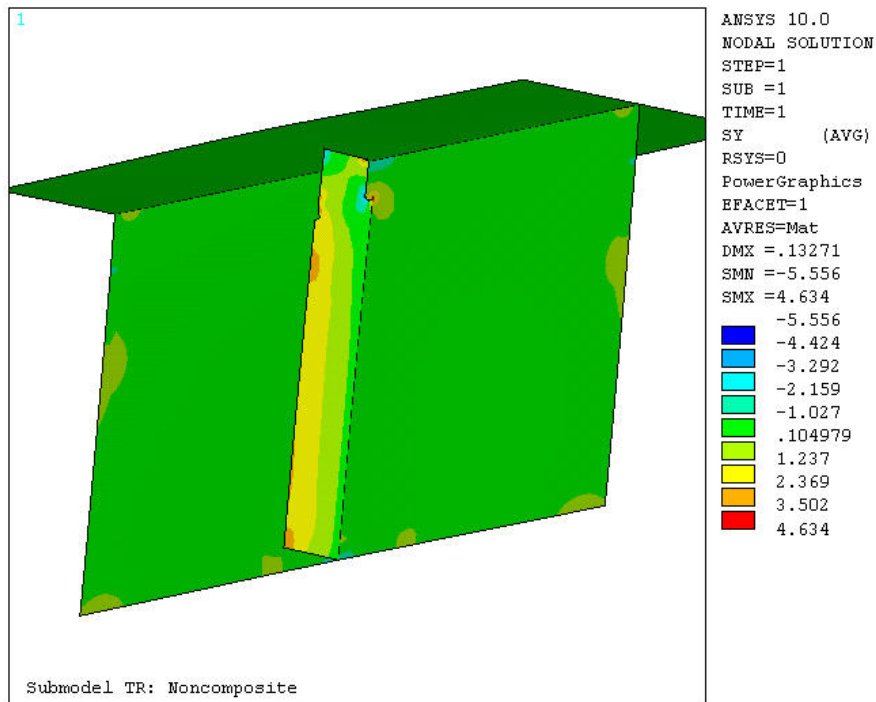
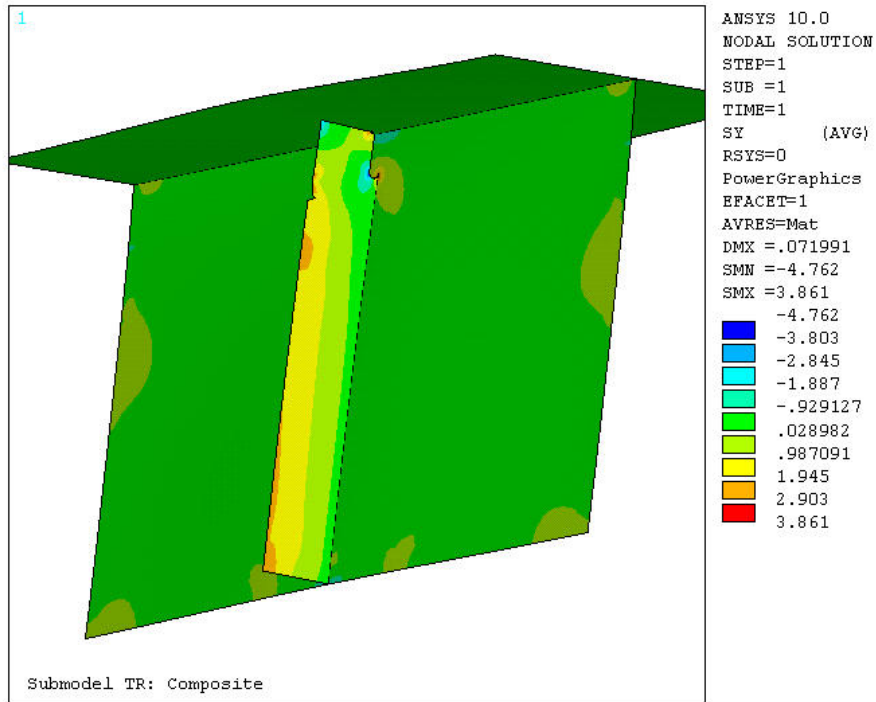


Figure 3.6: Comparison of Axial Stress in Frame Member for Composite and Noncomposite Models



(a)



(b)

Figure 3.7: Comparison of SY Stress Contours for Submodel TR for Composite and Noncomposite Global Models

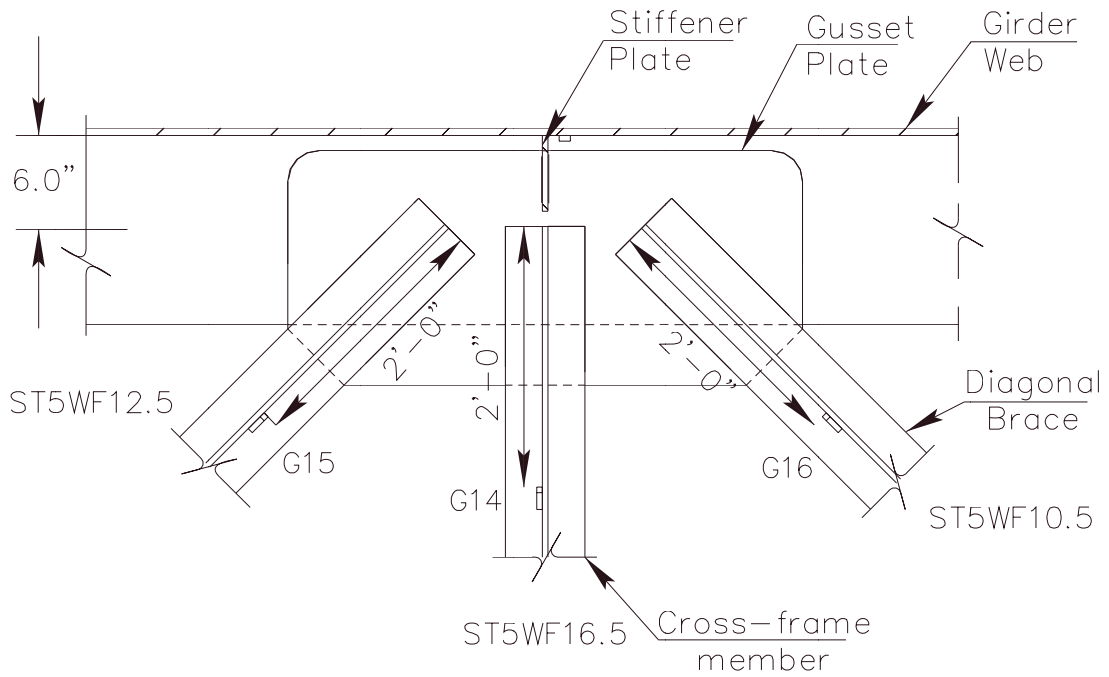
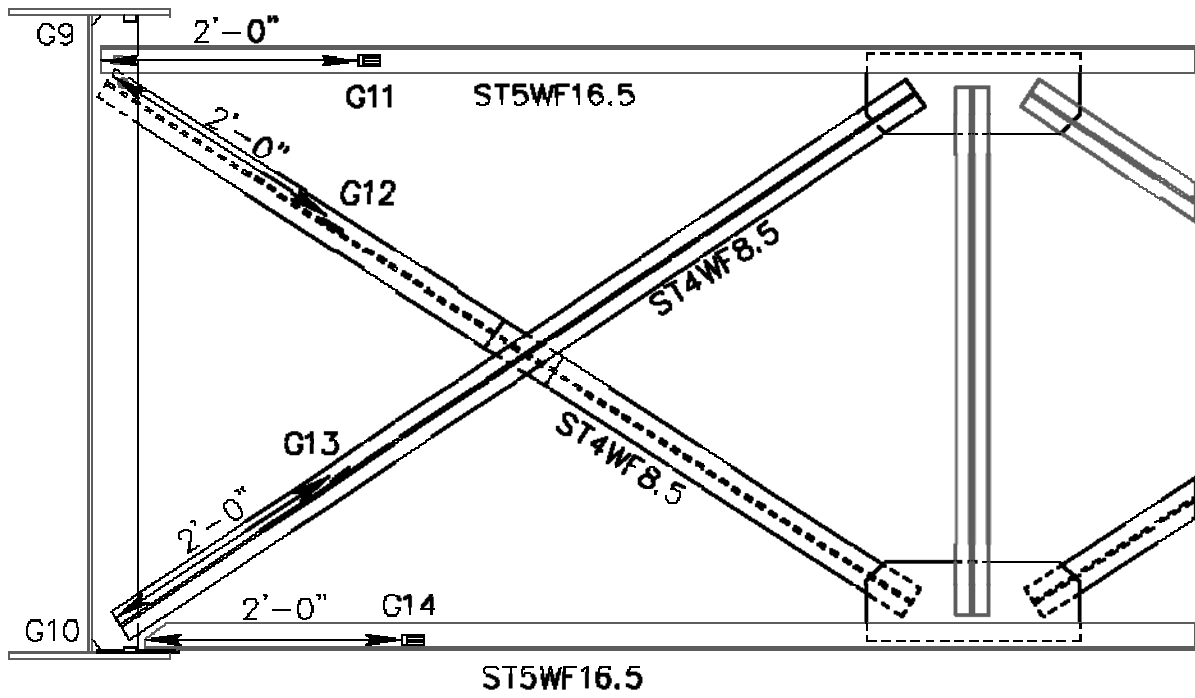


Figure 3.8: Location of Frame Gages, G11 to G16

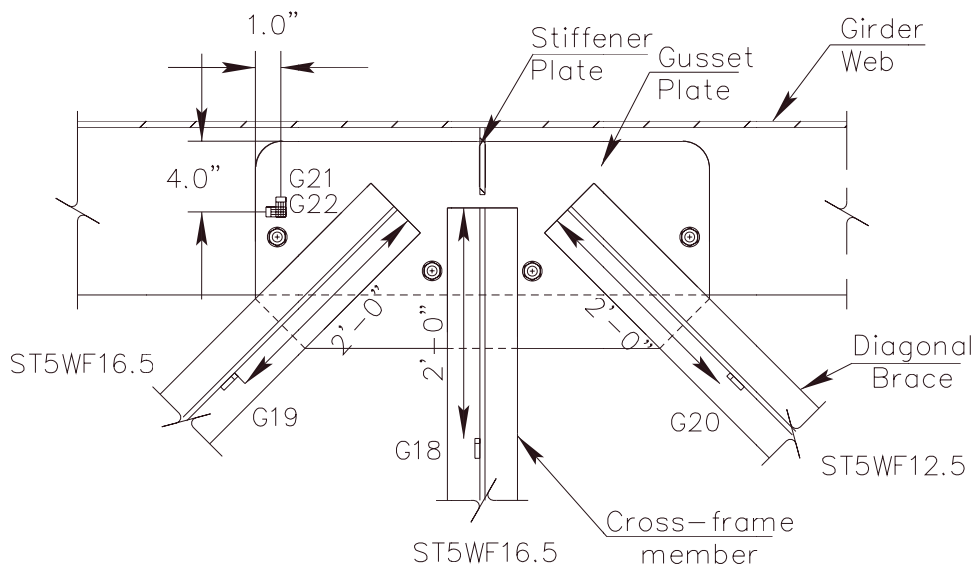
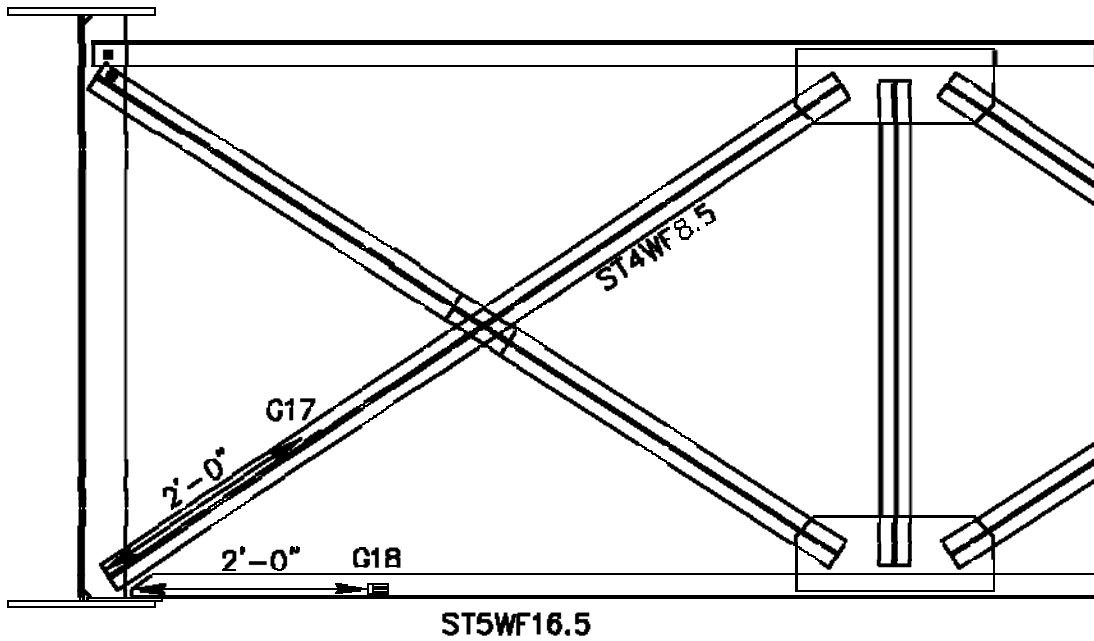


Figure 3.9: Location of Frame Gages, G17 to G20

CHAPTER 4: TOP CONNECTION ANALYSIS

In Steel bridges designed prior to 1970 it was a common practice to either terminate the transverse stiffener short of the flanges or only snug fit the stiffener between the flanges. Welding along the stiffener to flange intersection was discouraged to avoid a fatigue prone detail. Unfortunately, this creates an unstiffened portion of the web, commonly referred to as “web gap,” which is susceptible to fatigue caused by out-of-plane distortion. Tuttle Creek Bridge was no different and such details were present on the bridge, which were the primary site of fatigue cracking. Current bridge design specification prevents out-of-plane distortion fatigue through requirement of using a positive attachment between the girder flanges and the connection stiffeners.

The stresses caused by out-of-plane distortion are considered secondary stresses and are not accounted for in a routine analysis and design procedures. The stress range is the governing parameter to evaluate the fatigue life of a bridge and evaluate the effectiveness of fatigue retrofits. Finite element studies are therefore performed in this study to estimate these secondary stresses. The results from the analysis of the top flange connection are presented in this chapter. The analysis results are compared to the field test data and finite element models are then calibrated to better represent the actual physical behavior.

4.1 Top Flange Web Gap

4.1.1 Pre-1986 Web Gap Geometry

In previous finite element studies on Tuttle Creek Bridge a comprehensive analysis was done to determine the stress distribution around top and bottom flange web gaps at all the cross frames [Zhao and Roddis 2003]. The web gaps were modeled

to include a 1.5 x 1.5 inch clip, see Figure 4.1, to represent bridge conditions prior to any retrofits. The study indicated that for a west bound truck the most stressed top flange web gap is at connection B2W (see Figure 2.3). So, only the connection at B2W is analyzed in the present study.

Figure 4.2 shows the web gap stress variation of the detail under truck loading. The detail experiences two stress cycles when the truck goes across the bridge. However, a double-hump variation suggests that a small cycle is superimposed on a cycle with much larger stress range. For example, a rainflow cycle count on SY stress variation show that there are two stress cycles of magnitudes 4 ksi and 49 ksi. For each stress component the peak stress occurs at LC#21 when the truck is close to the mid span, see Figure 4.3. The minimum stress is nearly zero for all the stress components. AASHTO classifies a transverse stiffener as category C detail for which the Constant Amplitude Fatigue Limit (CAFL) is 10 ksi. The maximum stresses developed in the detail are all higher than CAFL and are of very high magnitude. This is why many cracks were found in the web gap region. Out-of-plane distortion caused by the pull of the cross-frame members is the cause of these localized secondary stresses in the web gap. Figure 4.4 shows variation of the out-of-plane distortion relative to the top flange (Point B in the figure) along the 1.5 in. web gap. The maximum out of plane displacement is 6.72×10^{-3} in. It is interesting to note that even a very small out-of-plane distortion can induce high secondary stresses. This is because the entire rotation of the slot end is absorbed over a small length of the unstiffened web gap.

Figures 4.5 to 4.7 show the web gap SX, SY, and SZ stress contours. The peak SX stress develops in the elements associated with the stiffener plate. The transverse

stress in the girder web is negligible because of the assumptions involved in plate bending theory, where displacement and stress normal to the mid-surface of the plate are ignored. Peak SY and SZ stresses develop in girder web elements. High stresses are localized in the web gap region and they start to drop below CAFL (10 ksi) at 3 in. away from each side of the stiffener plate, see Figure 4.8.

The vertical stress (SY) and longitudinal stress (SZ) are the primary driving stresses for a horizontal and a horseshoe type cracks, respectively. From the stress distribution plots (Figure 4.6 and 4.7) it can be observed that the peak SY and SZ stresses develop at the flange-to-web intersection and at the end of stiffener plate. This explains the observed crack patterns found in the top web gap detail on the bridge (Type A and Type B cracks in Figure 1.6).

4.1.2 Pre-Retrofit FE Analysis

In 1986, a retrofit strategy of softening the upper web gap was performed. In these repairs, the transverse connection plates were cut 1 in. below the termination of the existing weld cracks and a 0.5 in. radius was placed at the end of the cut. The total web gap length after the retrofit was approximately 4.5 in. The submodel B2W is modified to include the new web gap geometry, Figure 4.9. This modified submodel is called model TNR (top no repair) as it represents the pre-2005 retrofit or the 'no repair' condition of the top flange web gap. The coarse model used to analyze this submodel was CM2 which included a 4 in. web gap (see section 2.2).

The overall behavior is similar to model B2W. For a westbound truck the maximum stresses occur for LC#21. Figures 4.10 to 4.12 show the web gap SX, SY and SZ axial stress contours in model TNR. The peak transverse stresses develop in

stiffener plate elements and peak vertical and longitudinal stresses develop in the girder web. The maximum SX, SY, and SZ stresses are 27 ksi, 34 ksi, and 32 ksi, respectively. Compared to submodel B2W, the stresses developed at the slot end increase by 42%, 12%, and 39%, respectively for SX, SY, and SZ. The SY stress near the flange-to-web intersection reduces by 48% from 49 ksi to 25 ksi. The stresses however are still much higher than CAFL. The variation across the stiffener plate is similar to model B2W and the stresses drop below CAFL 3 in. away from each side of the stiffener plate.

The relative out-of-plane displacement of the slot end is 2×10^{-2} in., see Figure 4.13. Comparing with submodel B2W the relative displacement at 1.5 in. below the top flange reduces by 40%. The softening strategy was not effective and continued crack growth was observed (Figures 1.7 and 1.8). The increased flexibility increases the distortion at the slot end, however, it does not loosen the constraints enough to reduce the web gap stresses below acceptable limits and hence the continued crack growth.

4.1.3 Post-Retrofit FE Analysis

Analysis conducted prior to the repair proposal successfully demonstrated the effectiveness of a positive attachment between stiffener plate and top flange [Zhao and Roddis, 2004]. A positive attachment forces the top flange to deflect out-of-plane along with the web to reduce the out-of-plane displacement and hence lower the web gap stresses. The newly installed retrofit (Type 'A' Repair) positively attaches the connection stiffener plate to the top flange by using threaded welded studs and two angles attached to the stiffener by fillet welds, as shown in Figure 4.14. In addition, stop holes were drilled to arrest the horizontal crack growth.

The model TNR is modified to include the stiffener-to-flange attachment. The positive attachment is modeled by merging the coincident nodes at the stiffener-to-flange intersection. This modified submodel is called TR (top repaired), see Figure 4.15. The mesh is refined near the slot end and at the flange/stiffener intersection to aid convergence in the results. Merging the nodes is a simplified modeling approach for representing the installed bracket connection. The intent of the repair is to make the top flange deflect out-of-plane along with the web when it is pulled by the stiffener plate due to the action of the brace members. Merging the coincident nodes at the stiffener-to-flange intersection couples the motion of flange and the stiffener at these nodes in all directions, thus it is reasonable to assume that this model will be able to characterize the behavior of the modified web gap geometry.

Similar to the previous two submodels, the peak stresses occur at LC#21. Figures 4.16 to 4.18 show the SX, SY, and SZ stress contours for model TR at LC#21. The hot-spot for all the stress components is observed to be at the slot end. The stress distribution is similar to the previous two models. The peak SX stresses develop in the stiffener plate elements and the peak SY and SZ stresses develop in the girder web. The peak stresses are reduced significantly by at least 80%, proving the effectiveness of the repair. Figure 4.19 shows the plot of out-of-plane displacement relative to the top flange along the 4.5 in. long web gap. The web gap distortion is also significantly reduced. Table 4.1 summarizes the comparison of the critical web gap stresses and out-of-plane displacement before and after the retrofit.

Table 4.1: Pre and Post Retrofit Peak FEA Stresses in Top Flange Web Gap

	Pre-Retrofit	Post-Retrofit	Change
SX (ksi)	26.8	5.3	-80%
SY (ksi)	34.1	6.1	-82%
SZ (ksi)	32.0	4.3	-87%
Out-of-Plane Displacement (in.)	2×10^{-2}	8×10^{-4}	-96%

Note: Negative sign indicates percentage decrease after the retrofit

4.2 Top Flange Connection Model Calibration

4.2.1 Comparison with Pre-Retrofit Field Test

During the field investigations web gap gages (G1 to G8) were placed on top connection of B2E (Figure 2.2) of span # 29 the first full span from the easternmost abutment. Two sets of gages were used: one on the interior side of the girder (G1 and G2) and one on the exterior (G3 and G4). The location of the top web gap gages is shown in Figure 4.20. The FE models TR and TNR were built for the most critical top connection which was located at B2W. So, additional top connection submodels were built at connection B2E to compare with the test data. The modeling techniques used are same as used for models TNR and TR. Table 4.2 summarizes the peak stresses developed in the pre retrofit top connection models at B2W and B2E. The results indicate that the stresses developed in connection at B2E are 5% lower than those developed at B2W. This also corroborates the findings of the previous studies [Zhao and Roddis, 2004] which indicated that that B2W is the most stressed to connection. The stress distribution developed at B2E were similar to those obtained for models at B2W, however, the peak stresses in models at B2E occurs for LC#13 compared to LC#21 for models at B2W.

Table 4.2: Peak Stresses Obtained from TNR Models at B2W and B2E

	B2W	B2E	Difference (%)
SX (ksi)	26.7	25.3	5.0
SY (ksi)	34.1	32.4	5.0
SZ (ksi)	32.0	30.3	5.0

The results for models at B2E are used to compare with the test data for westbound truck pass. The pre-retrofit and post retrofit models at B2E are also designated as TNR and TR, respectively. These extrapolated stresses are compared with the peak stress at flange-to-web weld obtained from model TNR at B2E. From the FE analysis the stress values were obtained for nodes close to the gage locations.

Table 4.3: Pre-Retrofit Top Web Gap Stresses Obtained from Field Test Data and FE Analysis

Gage Number	Stress at Gage Location (ksi)		Stress Near Horiz. Crack Tip (ksi)	
	Test	FEA	Test	FEA
G1	-24.7	-18.6	-34.4	-25.2
G2	-9.3	-9.5		(-27%)
G3	25.3	18.7	35.4	26.0
G4	9.2	9.6		(-27%)

Table 4-3 compares the stresses obtained from FE analysis with that derived from the field strain data. The stresses at the gage locations G2 and G4 are in good agreement with the field data. Field stress values are gage location G1 and G3 are, however, 27% higher than the estimated analytical values. The gages G1 and G3 are closer to the horizontal crack which may influence their measured strain values. The surface crack was not included in the finite element model and so the difference in the stress values is expected. Since the crack is included in the calibrated post-retrofit finite element model (see section 4.2.3), no further analysis is done for model TNR. The gages on the interior and exterior sides of the girder show, respectively, compressive and tensile stresses as predicted by the FE model. The predicted and the observed

stresses are much higher than the CAFL (10 ksi) for a category C detail. This shows that the 4 in. repair was inadequate and explains the observed continued crack growth.

4.2.2 Comparison with Post-Retrofit Field Test

Table 4.4 compares the stresses obtained from model TR with that obtained from the field test for gages G1 to G4 (Figure 4.20). The extrapolated gage stresses are compared with maximum stresses at flange-to-web weld in submodel TR.

Table 4.4: Post-Retrofit Top Web Gap Stresses Obtained from Field Test Data and FE Analysis

Gage Number	Stress at Gage Location (ksi)		Stress Near Horiz. Crack Tip (ksi)	
	Test	FEA	Test	FEA
G1	-4.5	-2.3	-6.6	-3.3
G2	-1.1	-1.8		(-50%)
G3	7.0	1.6	9.3	2.0
G4	3.3	1.1		(-78%)

The predicted peak tensile stresses at flange-to-web weld on girder exterior face are lower than the observed field values for the pre and post retrofit test by 27% and 78%, respectively (see Tables 4.3 and 4.4). Further, the amount of reduction predicted from FE analysis is greater than that predicted from the field tests. It is thus necessary to modify and calibrate the FE models to simulate the true physical behavior. The differences in the stresses are caused by the presence of a surface crack on the interior face of the girder. The location of the crack is indicated in the Figure 4.14. The crack introduces an additional stress raiser at its tip and modifies the stress distribution in the web gap. Therefore, the model TR is reanalyzed with this crack included in the FE model. The results from this analysis are discussed in the next section.

4.2.3 Calibrated FE Model

Submodel TR is modified to include a 2 in. long through thickness crack, 0.5 in. below the top flange surface and extending 1 in. on both side of the stiffener plate, see Figure 4.21. The modified submodel is called TRC (top repaired calibrated). A surface crack could not be represented in the FE analysis and the crack is modeled by leaving a small gap (0.05 in.) between the shell elements at the appropriate location of the crack. The FE mesh is refined to appropriate levels to achieve satisfactory convergence at the crack tip. Since the measured gage stresses correspond the vertical stresses, FE results for only the SY stress components are presented here.

Figures 4.22 shows the web gap SY stress distribution plots for model TRC. The hot-spot is relocated from the slot end to the crack tips. Presence of the crack, however, does not alter significantly the overall distribution in the web gap. The stresses are localized around the crack tip and away from the tip the stress distribution is similar to that obtained from model TR. The crack tip stresses are higher than the observed values. This is because the crack was modeled as a through crack rather than a surface crack, which significantly increases the stress concentration near the crack tip

The model TRC is further modified to include the $\frac{3}{4}$ in. stop hole drilled at the crack tip, see Figure 4.23. This model is called TRCH (top repaired calibrated with holes). The hole removes the singularity at the crack tip and reduces the stresses. Figure 4.24 shows the SY stress distribution in the web gap. Table 4.5 compares the web gap stresses obtained from the calibrated model TRCH with the measured values. The peak stress values are much closer to the measured values. The error in estimation of peak tensile stress reduces from 78% to 13%. The stresses away from the crack still

differ from the measured values. The possible reason for this difference could be that the gages are placed much closer to the crack than indicated on the drawings.

Table 4.5 Post-Retrofit Top Web Gap Stresses Obtained from field Test Data and Calibrated FE Analysis

Gage Number	Stress at Gage Location (ksi)		Stress Near Horiz. Crack Tip (ksi)	
	Test	FEA	Test	FEA
G1	-4.5	-2.5	-6.6	-11.2
G2	-1.1	-2.0		(+41%)
G3	7.0	1.3	9.3	8.1
G4	3.3	1.0		(-13%)

The field test and the analysis both show a significant amount of reduction in stresses after retrofit, see Table 4.6, proving the effectiveness of the type 'A' repair.

Table 4.6: Pre-Retrofit and Post-Retrofit Top Web Gap Peak Stresses Obtained from Extrapolated Gage Values and FE Analysis

	Pre-Retrofit Stress Near Horiz. Crack Tip (ksi)		Post-Retrofit Stress Near Horiz. Crack Tip (ksi)	
	Test	FEA	Test	FEA
Interior Side	-34.4	-25.2	-6.6 (-81%)	-11.2 (-55%)
Exterior Side	35.4	26.0	9.3 (-74%)	8.1 (-68%)

Note: Negative sign indicates percentage decrease after the retrofit

4.2.4 Effectiveness of the Stop Hole Repair

In 1980, Fisher proposed a criterion to determine the size of the stop holes to prevent reinitiation of the fatigue cracks [Fisher et. al., 1980], this is

$$\frac{\Delta\sigma\sqrt{\pi A_r}}{\sqrt{\rho}} \leq 4\sqrt{\sigma_y} \quad \text{Equation 4.1}$$

where: ΔK = stress intensity factor range = $\Delta \sigma \sqrt{\pi A_r}$;

ρ = radius of the drilled stop hole (in);

A_r = half the equivalent crack length after rehabilitation, see Figure 4.25;

$\Delta \sigma$ = nominal stress range (ksi);

σ_y = yield strength of the material (ksi).

The nominal stress is defined as the far-field stress away from any stress concentrations. The stress magnitudes obtained from the field test are higher than the calculated values. Therefore, it is conservative to use the field stress values than the FE results to evaluate the effectiveness of the stop hole repair. The gage G3 is closer to the crack tip and the stresses at its location may still be affected by the crack and therefore it is not appropriate to use its value in the above equation. Stress at gage location G4 is assumed to be sufficiently away from the crack tip and used as the nominal stress, i.e., $\Delta \sigma$ is taken as 3.3 ksi. Yield stress for material ASTM A373-54T can be assumed as the lower bound value for the material i.e., 36 ksi. The equation indicates that it is conservative to use a lower estimate for yield strength, i.e., lower the material strength severer is the requirement on the hole diameter. For a 2 in. long crack with $\frac{3}{4}$ in diameter holes at the ends, $A_r = 1.375$. Using Eq. 4.1 the minimum diameter required for an effective stop hole is 0.2 in. The installed hole diameter is 0.75 in and is therefore sufficient to arrest the crack growth.

4.3 Effect of Type 'A' Retrofit on Top Flange Stresses

The installed repair (Type 'A') positively attaches the top flange to the stiffener plate. Under the action of bracing member forces the flange will be forced to move out-of-plane along with the stiffener. In the past, stiffener-to-flange weld was not

recommended to avoid a fatigue critical detail. In this section the effects of the retrofit on stress distribution in the top flange is examined. Since the effects of the horizontal crack in the web are localized, the flange stresses will not be, therefore the submodels TNR and TR are used for comparing the flange stresses before and after the retrofit. Figures 4.26 and 4.27 show the flange SX and SZ stress distributions before and after the repair. The plate bending theory assumes that the stresses normal to the mid-surface are neglected; consequently, the normal stresses SY are negligible. Similar to web gap stresses peak stresses in flange occur at LC#21. The peak stresses are observed at the flange-to-stiffener connection. Since the flange moves out-of-plane and rotate, it creates stress concentrations at the corners of the stiffener plate. Due to the positive attachment this out-of-plane movement will be greater after the retrofit and hence greater stresses near the corners of stiffener plate at the flange-to-stiffener connection. Table 4.7 summarizes the maximum SX and SZ stresses in the flange before and after the repair.

Table 4.7: Top Flange SX and SZ Stresses Before and After Retrofit

	Pre-Retrofit	Post Retrofit
SX (ksi)	1.2	2.8
SZ (ksi)	-0.2	1.1

4.4 Fatigue Life

The top flange web gap compared to other details on the bridge is most susceptible to fatigue cracks. So, the fatigue life calculations are done only for this detail and it is assumed that it will control the overall fatigue life of a typical intermediate span of the bridge. The stress variation for a truck going across the span indicates that the detail experiences two stress cycles. However, stress range of one is much larger than the other [see section 4.1.1]. Therefore only one stress range cycle per truck is used for

fatigue life calculations. This assumption is consistent with ASSHTO LRFD [AASHTO 1998], which recommends one stress cycle per truck passage for spans greater than 40 ft. Based upon the traffic flow the fatigue life of the detail can be calculated using the equation

$$N_Y = \frac{A}{365n(\Delta\sigma)^3(ADTT)_{SL}} \quad \text{Equation 4.2}$$

Where: N_Y = fatigue life in years

A = Fatigue category constant for category C detail = $44 \times 10^8 \text{ ksi}^3$

n = number of stress cycle per truck passage

$\Delta\sigma$ = stress range

$(ADTT)_{SL}$ = average number of trucks per day in a single-lane

The peak stress range obtained from the field test data is higher than those calculated from the analysis and so it is conservative to use the measured values for fatigue life calculations. For one truck passage the analysis shows that the minimum stress is zero. Thus the stress range can be taken as $\Delta\sigma = \sigma_{\max} - \sigma_{\min} = 9.3 \text{ ksi}$. $(ADTT)_{SL}$ in 2003 was 430 with 15 % truck traffic. Table 4.8 calculates the fatigue life corresponding to the future $(ADTT)_{SL}$ value considered as a percent increase of the 2003 KDOT statistics.

Table 4.8: Fatigue Life of the Bridge

Percentage of the 2003 truck traffic	Future $(ADTT)_{SL}$	Fatigue life (years)
200%	130	115
175%	114	131
150%	98	153
100%	65	231

4.5 Summary

The finite element models were successfully calibrated to the field test data. The results obtained from the calibrated model TRC are in good agreement with the test data. The pre-retrofit analysis shows that the distortion induced stresses in the web gap are the primary cause of the fatigue cracks. The peak stresses in the web gap develop at the end of the clip and at the flange-to-web fillet weld, which explains the observed crack patterns of the horseshoe and horizontal type cracks. The stresses are reduced significantly after the stiffener is attached to the top flange. The analysis shows a reduction of at least 68% in peak stresses, which agrees well with the field test data which shows a reduction of at least 74% in the peak stresses. The stresses are now well below the fatigue limit of 10 ksi. In addition to the positive attachment, the stop holes at the horizontal crack tips are sufficient to arrest crack growth. Type 'A' repair is thus very effective in improving the fatigue life of the detail and provides a service life of 231 years for the present truck traffic statistics.

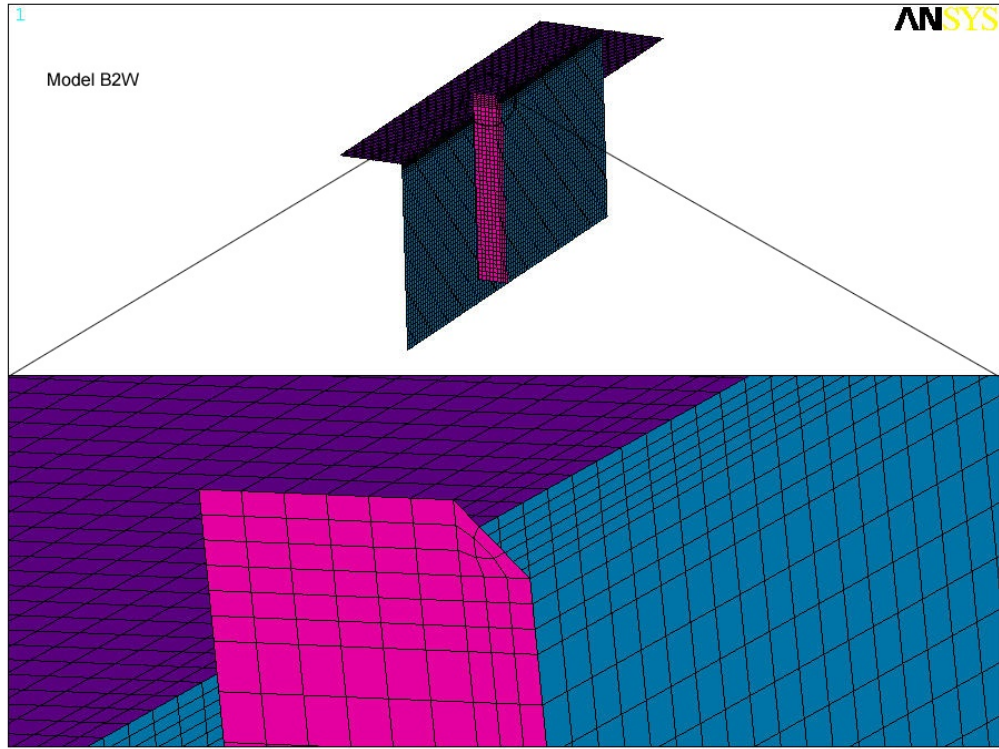


Figure 4.1: Pre-1986 Top Connection Submodel, B2W

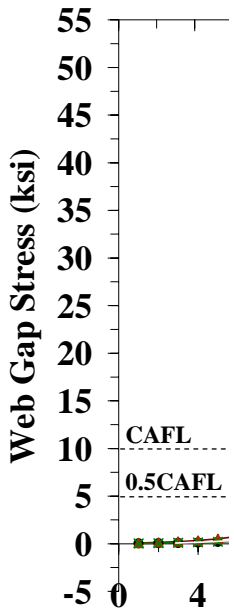


Figure 4.2: Stress Variation in Pre-1986 Top Flange Web Gap

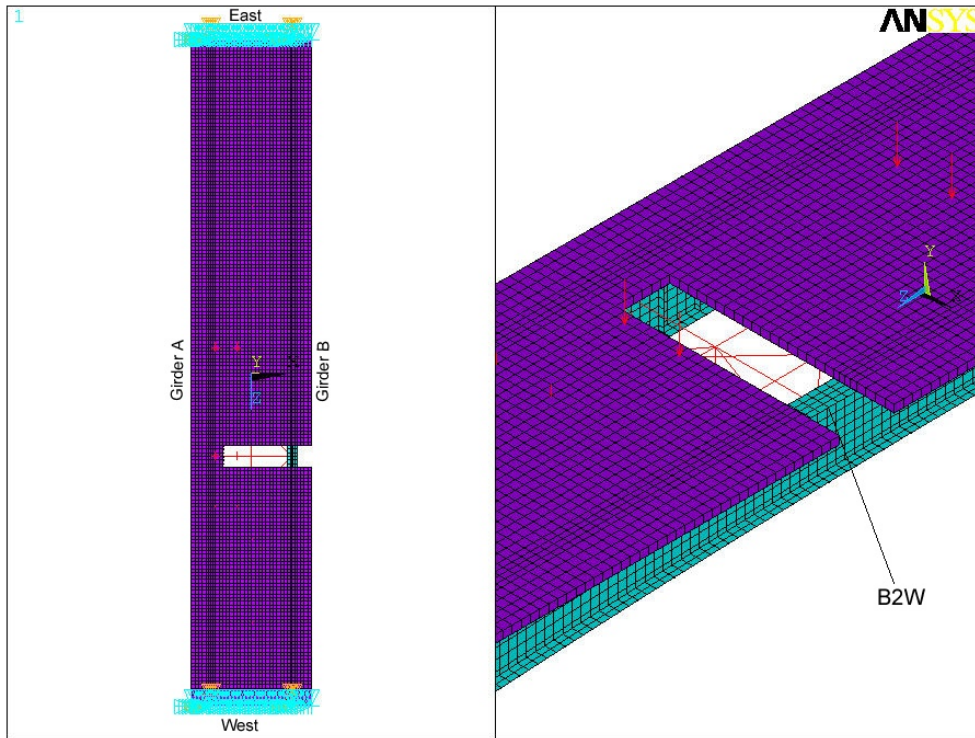


Figure 4.3: Truck Position for Load Case # 21

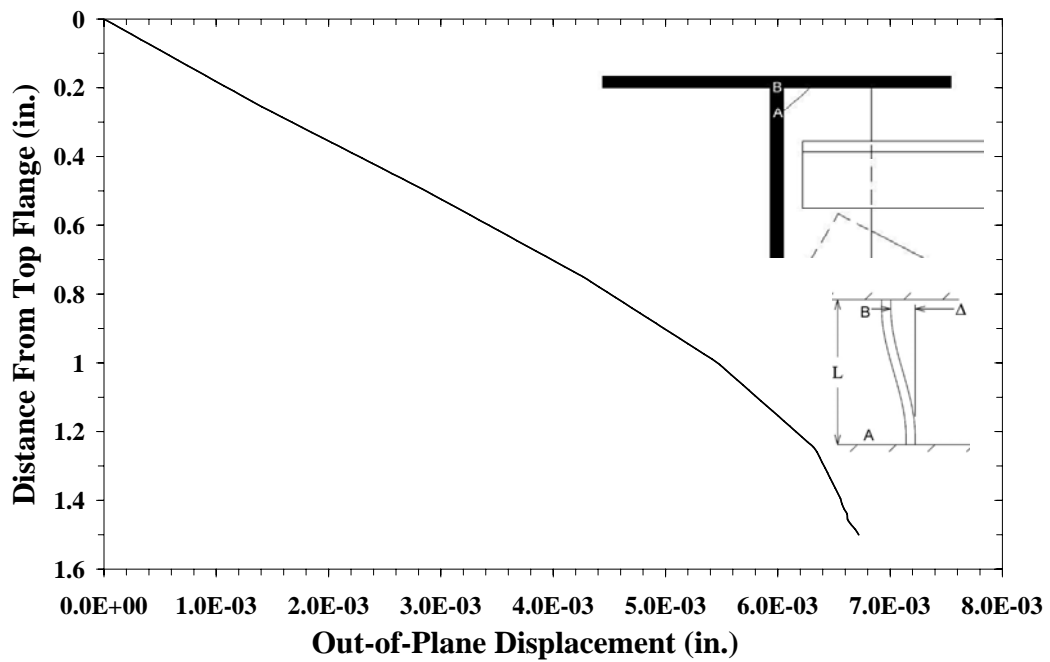


Figure 4.4: Out-of-Plane Displacement in Pre-1986 Top Flange Web Gap

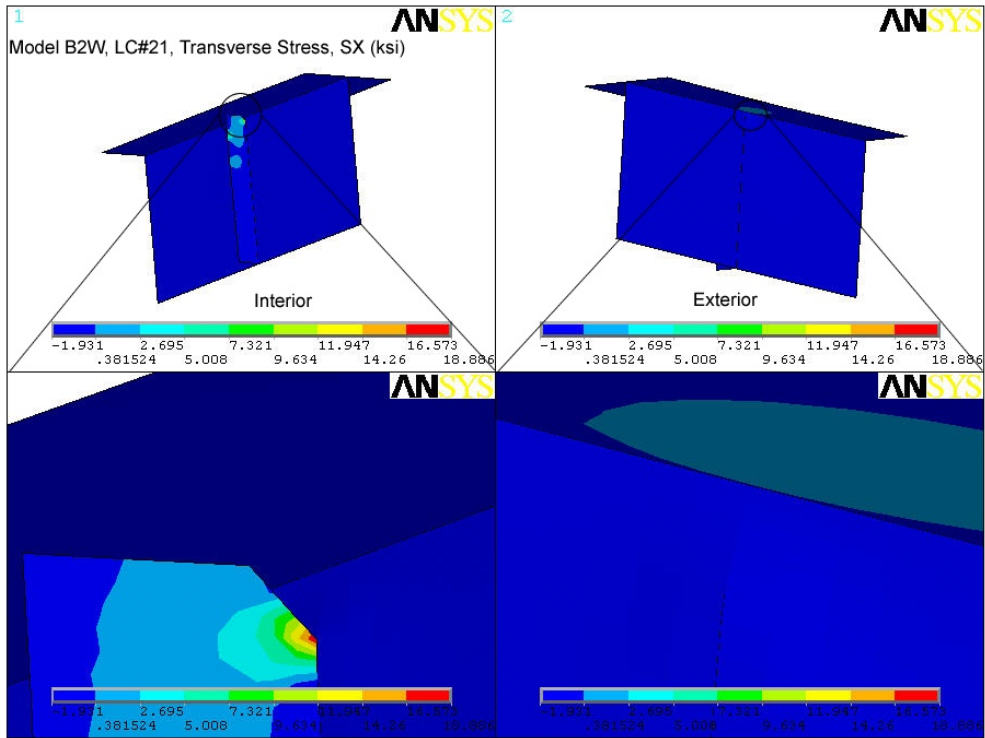


Figure 4.5: SX Stress Contours in Pre-1986 Top Flange Web Gap

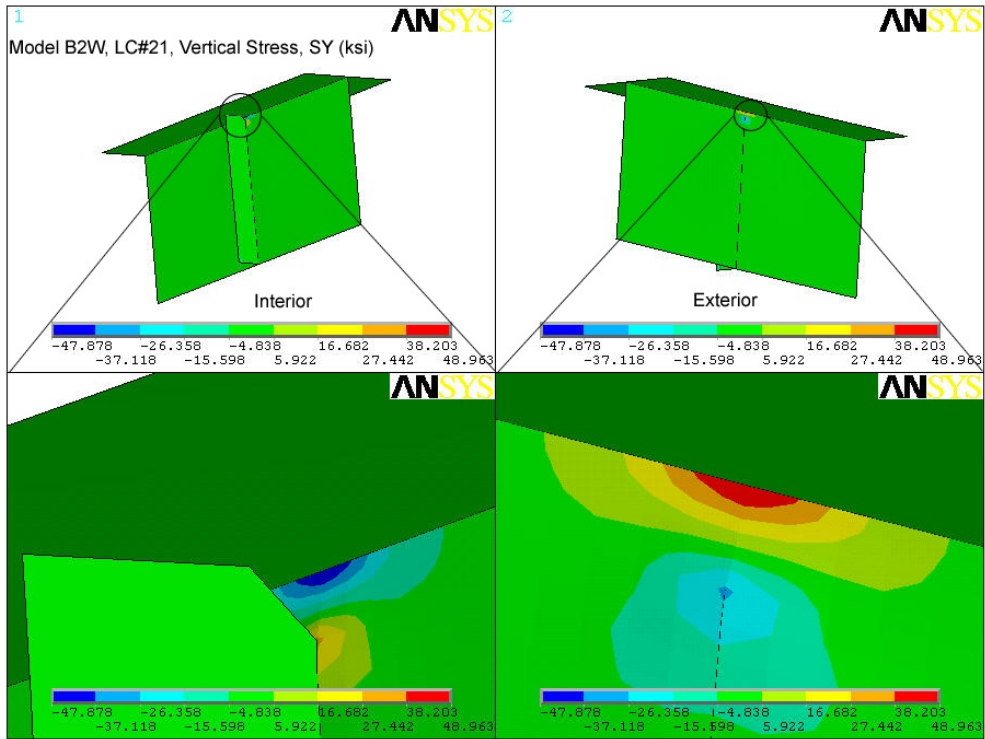


Figure 4.6: SY Stress Contours in Pre-1986 Top Flange Web Gap

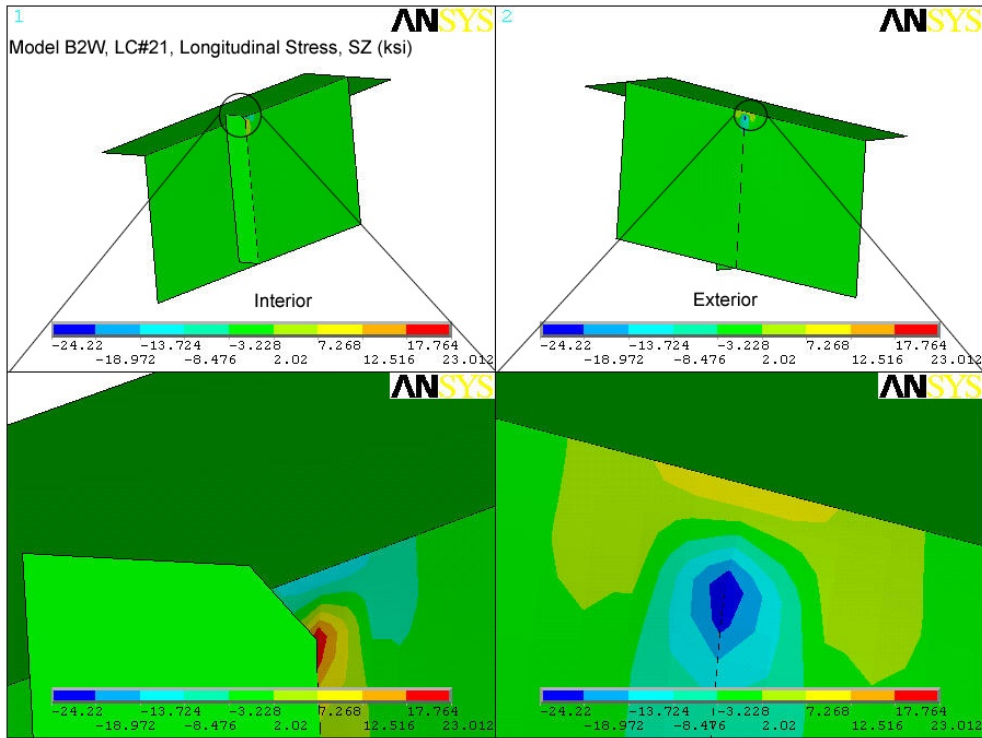


Figure 4.7: SZ Stress Contours in Pre-1986 Top Flange Web Gap

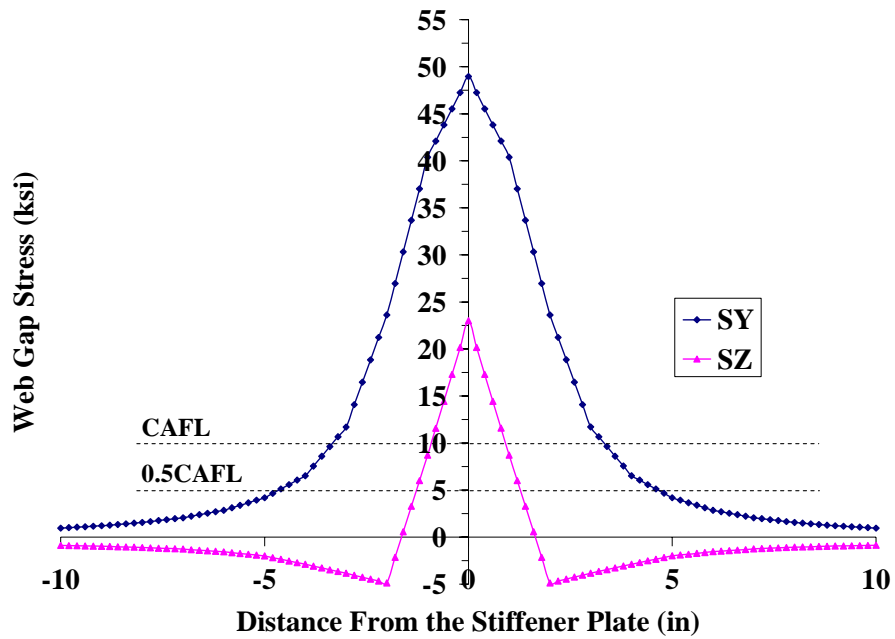


Figure 4.8: Variation of Web Gap Stress Across the Stiffener Plate in Pre-1986 Top Flange Web Gap

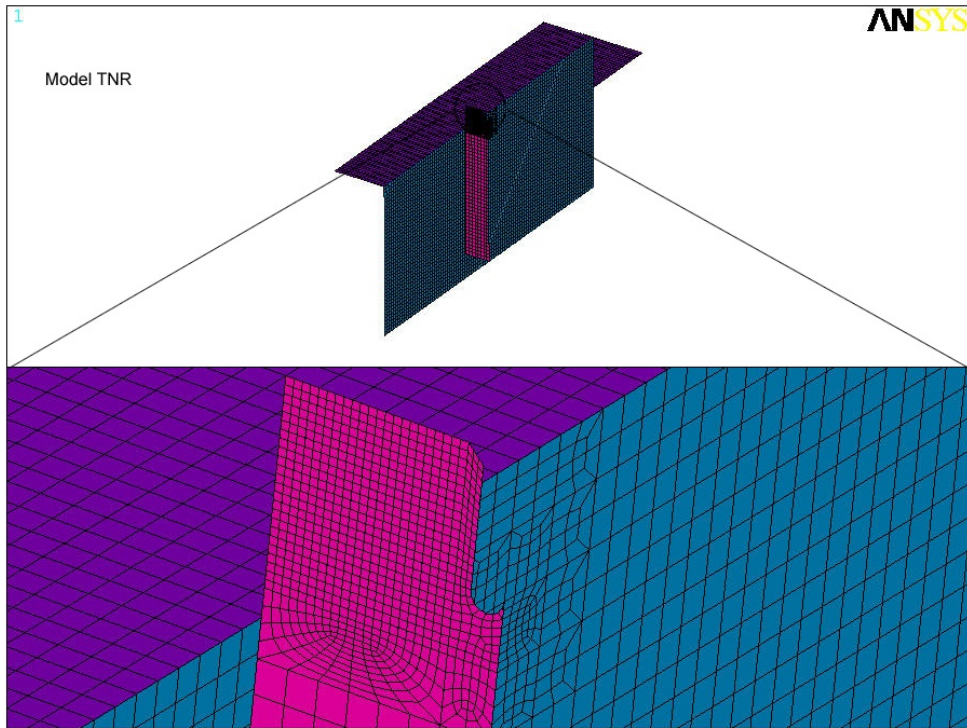


Figure 4.9: Pre-Retrofit Top Connection Submodel, TNR

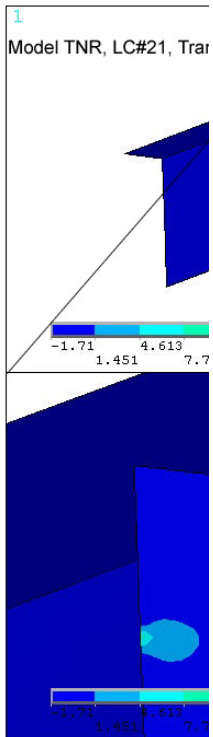


Figure 4.10: SX Stress Contours in Pre-Retrofit Top Flange Web Gap

Figure 4.11: SY Stress Contours in Pre-Retrofit Top Flange Web Gap

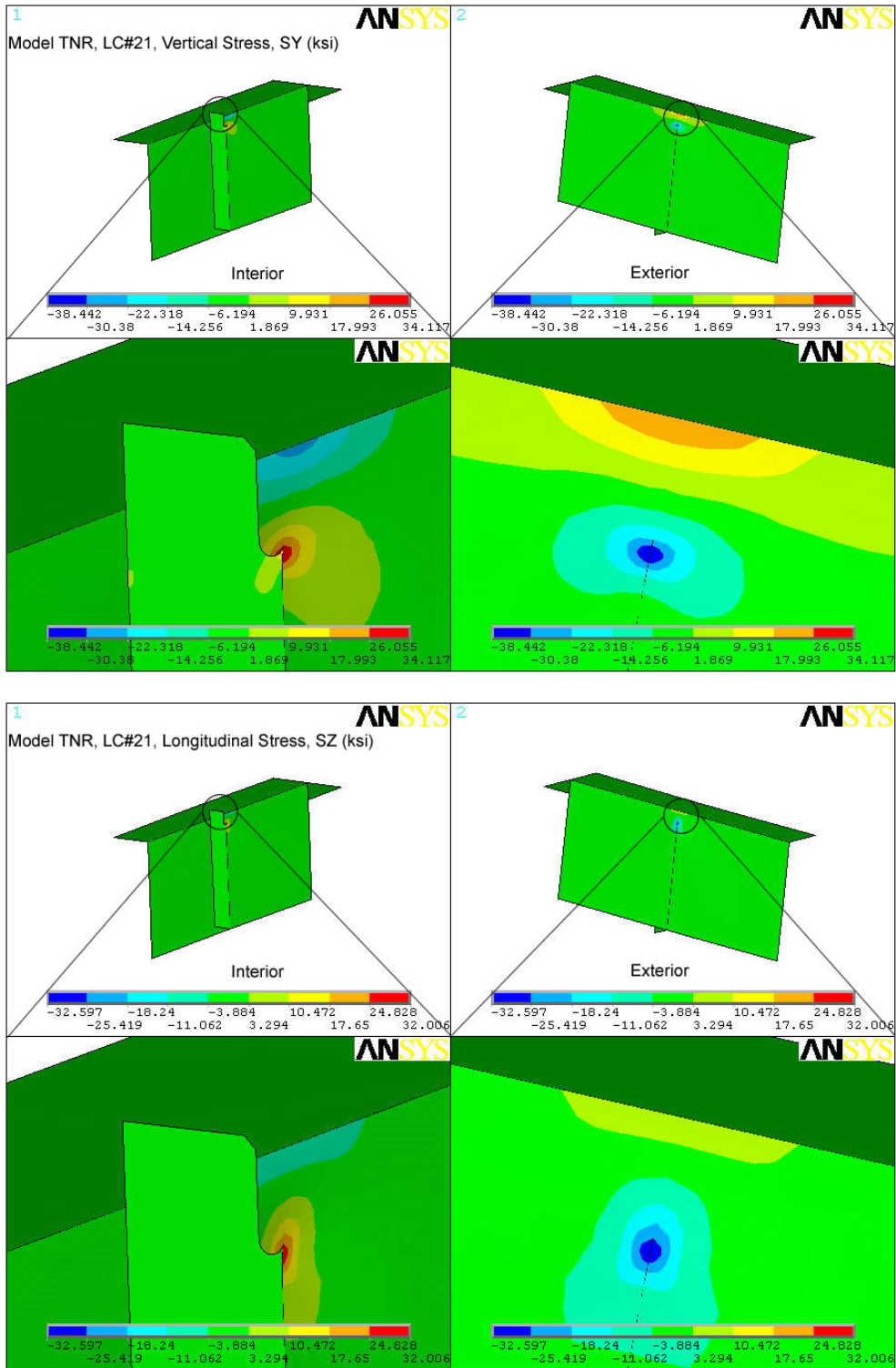


Figure 4.12: SZ Stress Contours in Pre-Retrofit Top Flange Web Gap

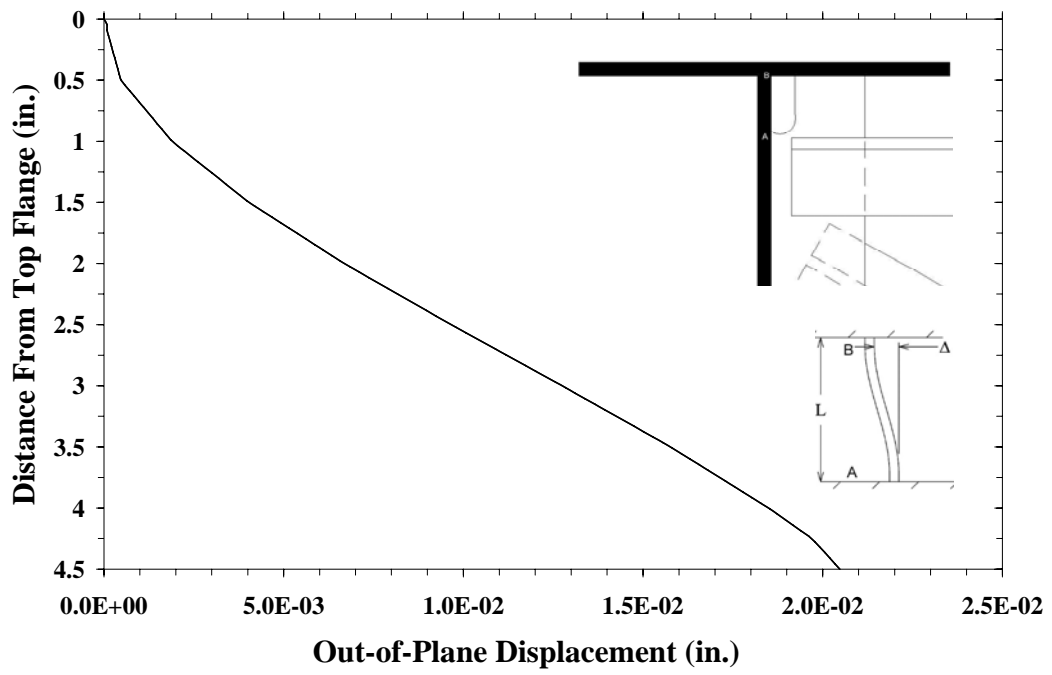
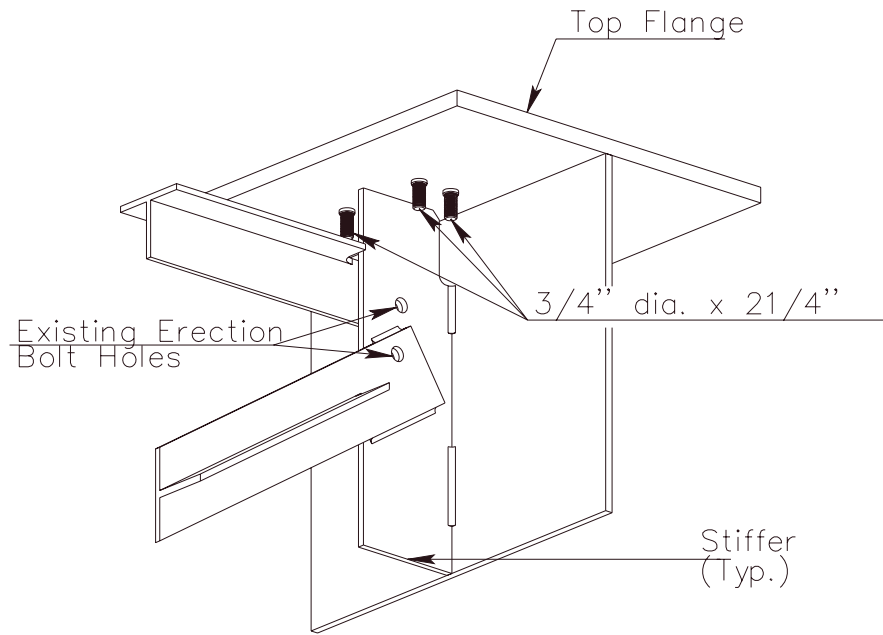
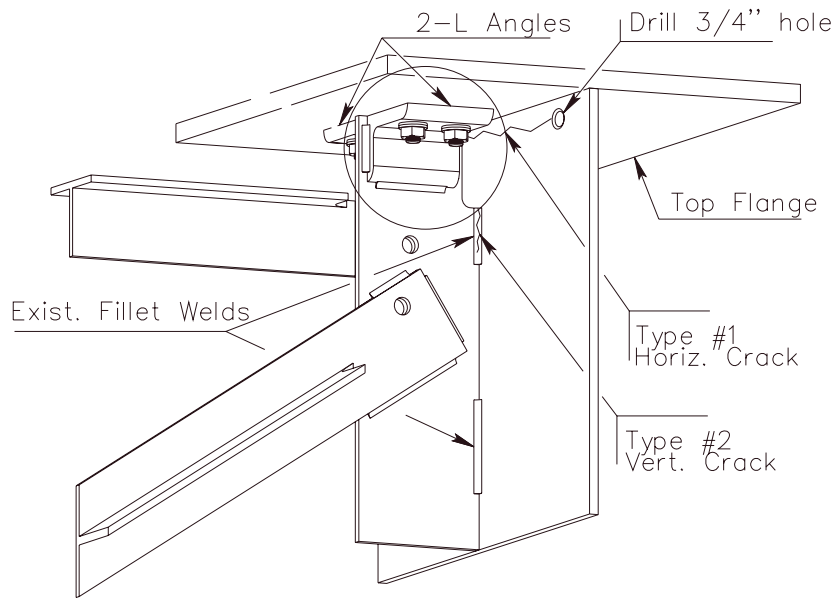


Figure 4.13: Out-of-Plane Displacement in Pre-Retrofit Top Flange Web Gap



(a) Studs Welded to Flange



(b) Angles Welded to Stiffener

Figure 4.14: Type 'A' Repair for Top Flange Connection

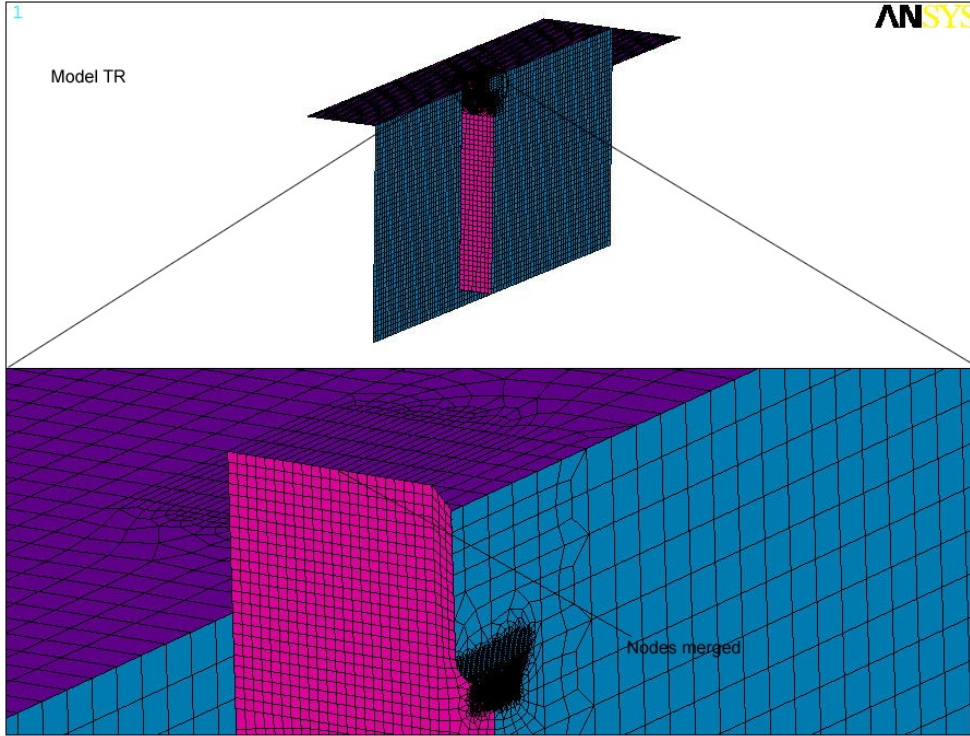


Figure 4.15: Post-Retrofit Top Connection Submodel, TR

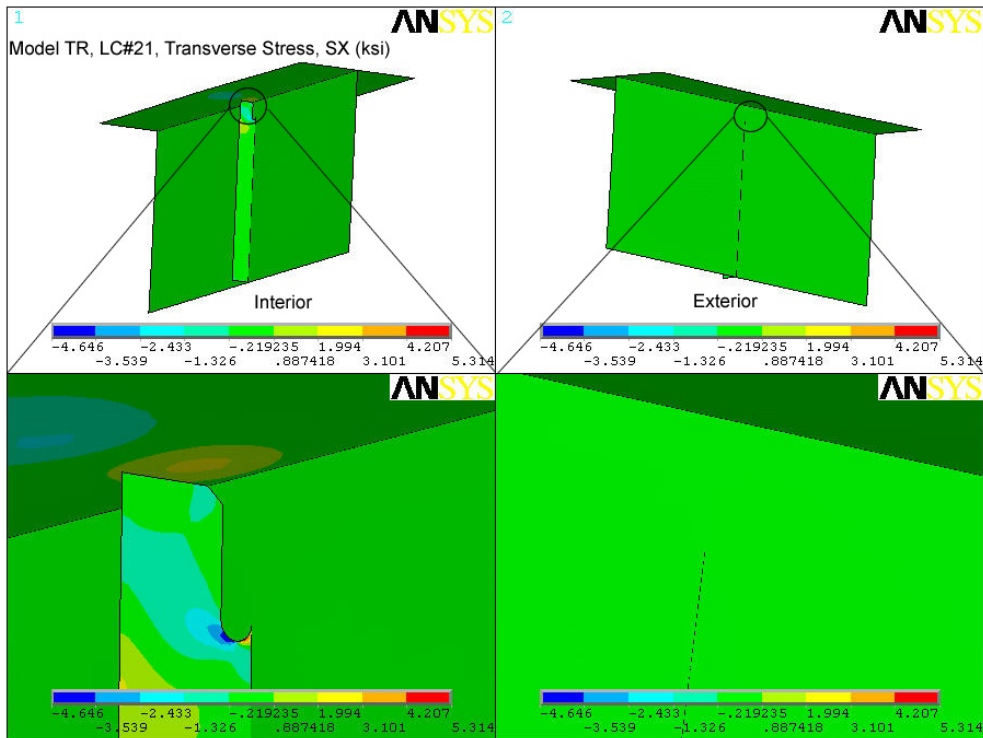


Figure 4.16: SX Stress Contours in Post-Retrofit Top Flange Web Gap

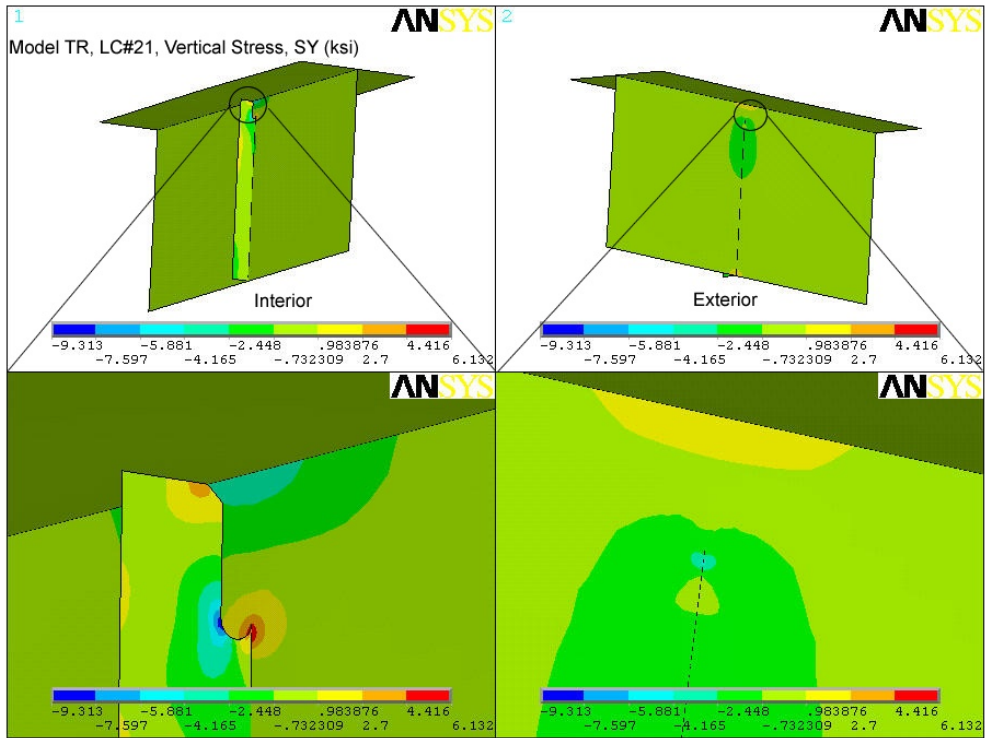


Figure 4.17: SY Stress Contours in Post-Retrofit Top Flange Web Gap

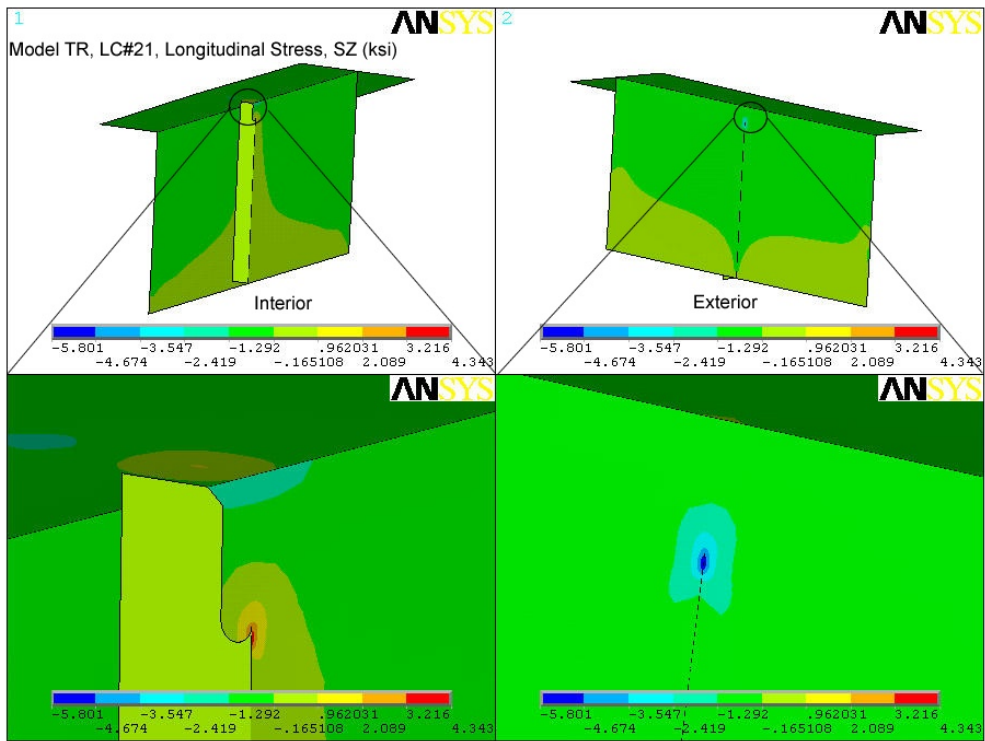


Figure 4.18: SZ Stress Contours in Post-Retrofit Top Flange Web Gap

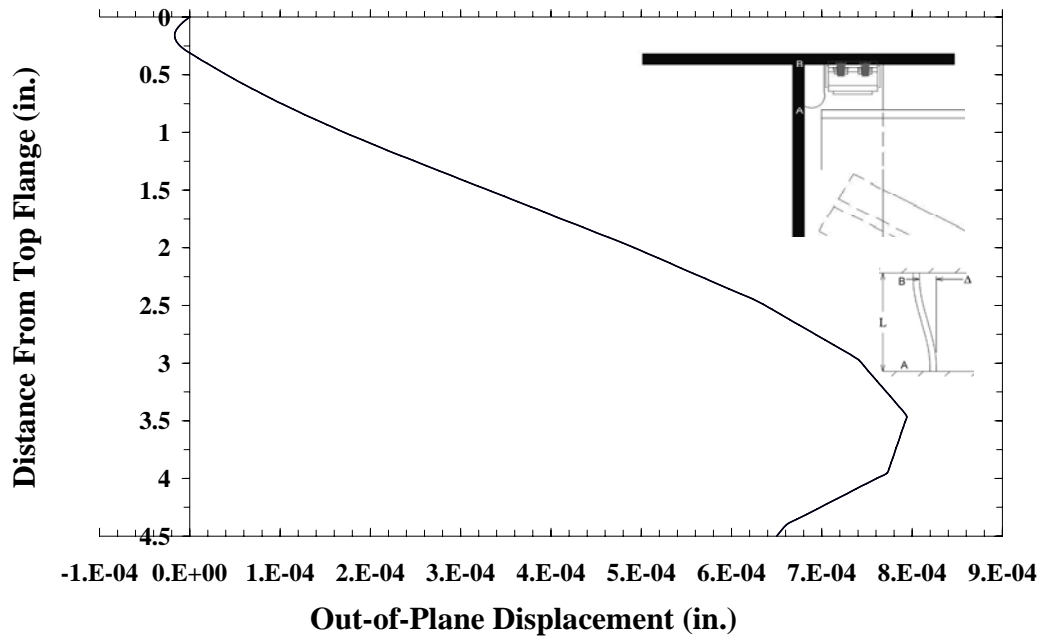
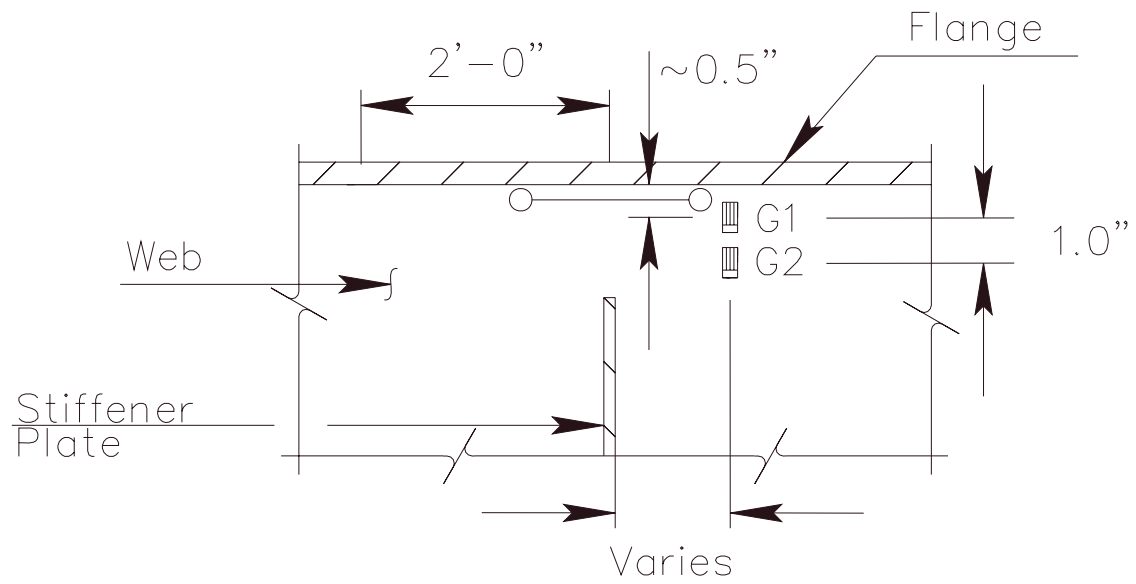
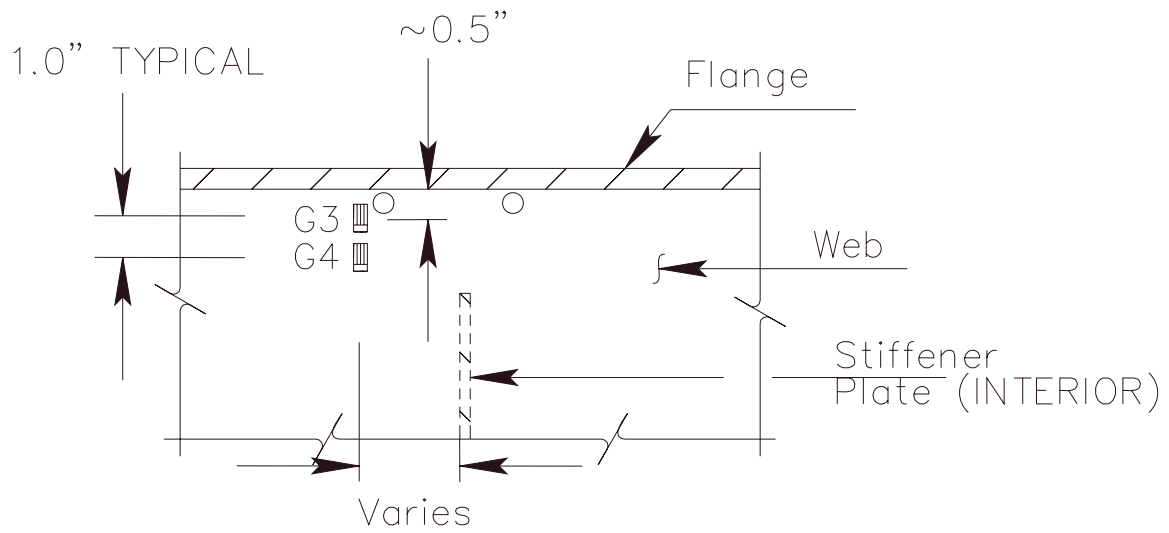


Figure 4.19: Out-of-Plane Displacement in Post-Retrofit Top Flange Web Gap



(a) Interior Side of the Girder



(b) Exterior Side of the Girder

Figure 4.20: Location of Top Flange Web Gap Gages, G1 to G4

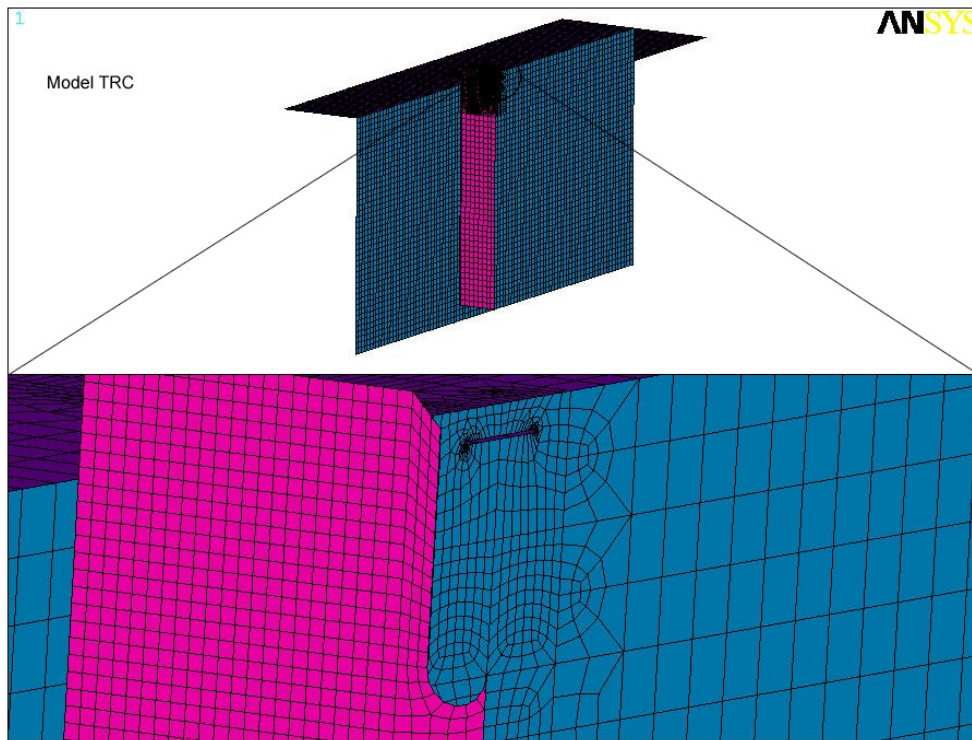


Figure 4.21: Calibrated Top Connection Submodel, TRC

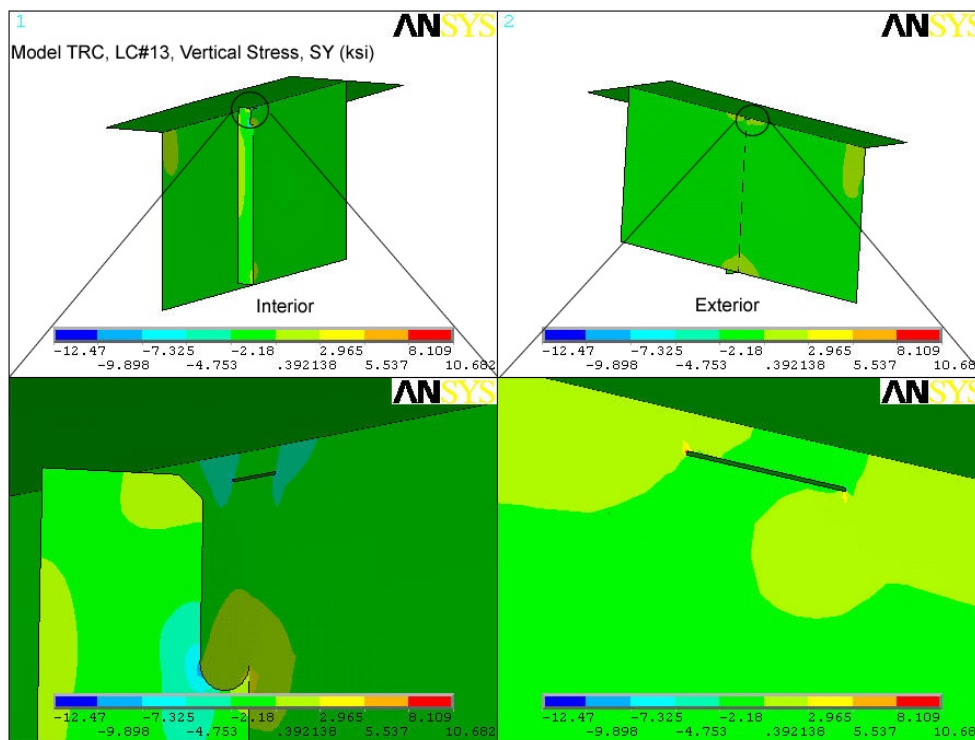


Figure 4.22: SY Stress Contours in Calibrated Post-Retrofit Top Web Gap FE Model

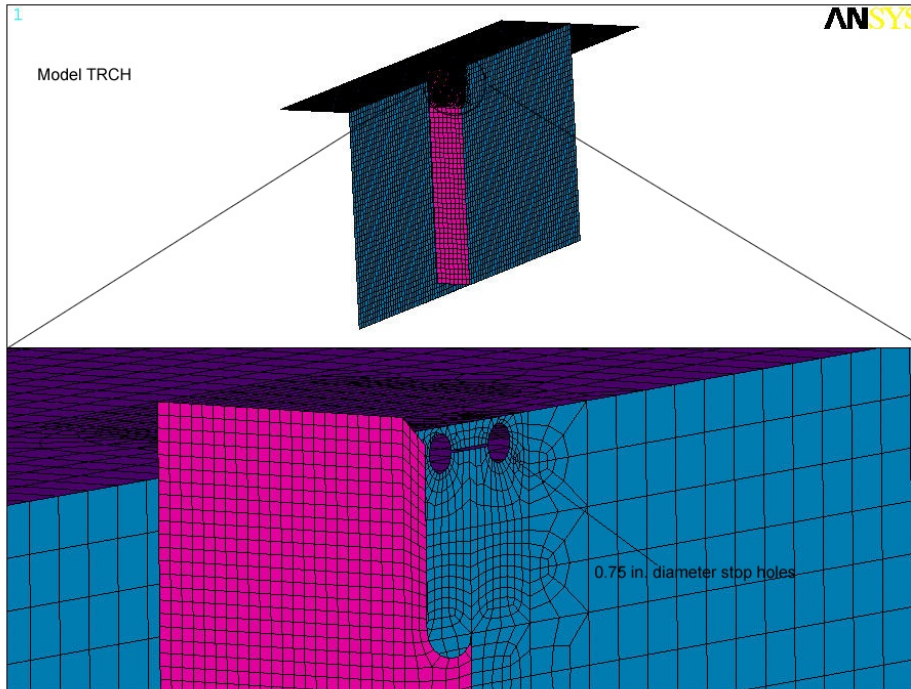


Figure 4.23: Calibrated Top Connection Submodel With Stop Hole, TRCH

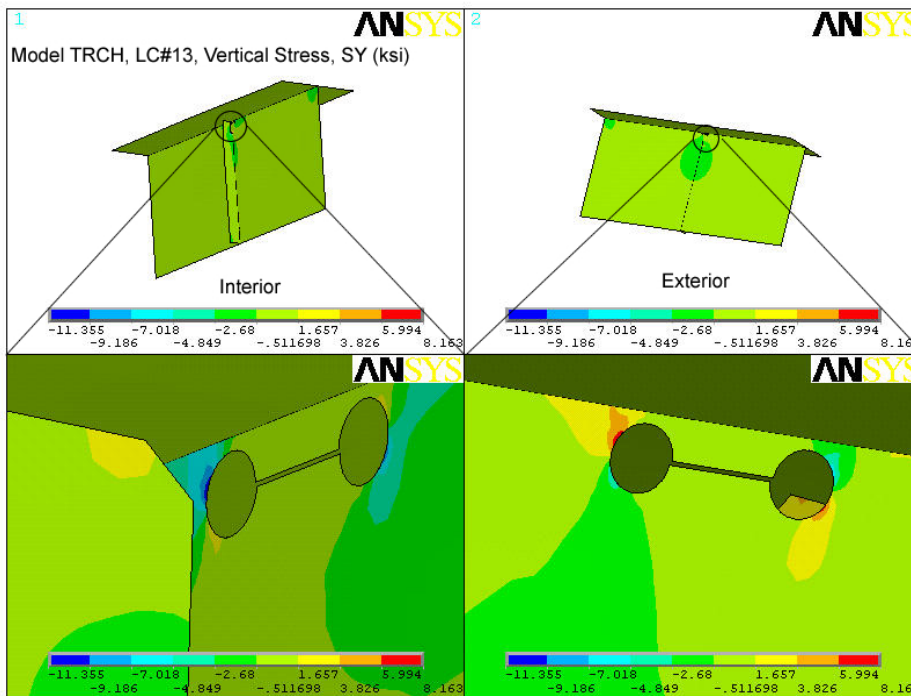


Figure 4.24: SY Stress Contours in Calibrated Post-Retrofit Top Web Gap FE Model With Stop Holes

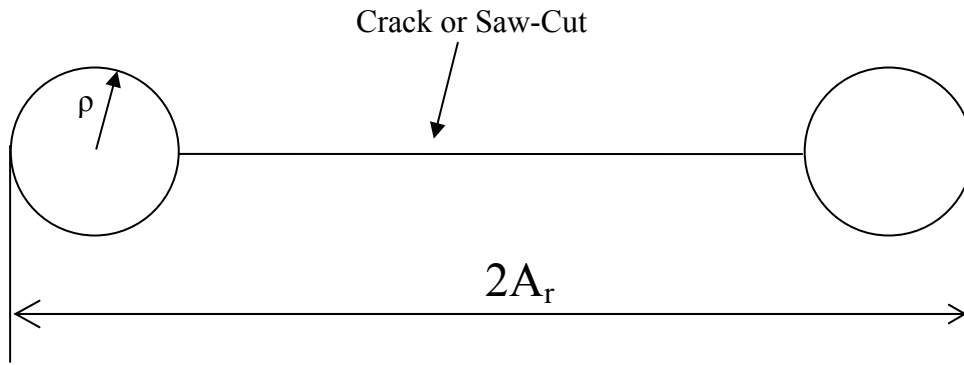


Figure 4.25: Stop Hole Retrofit proposed by Fisher et. al.

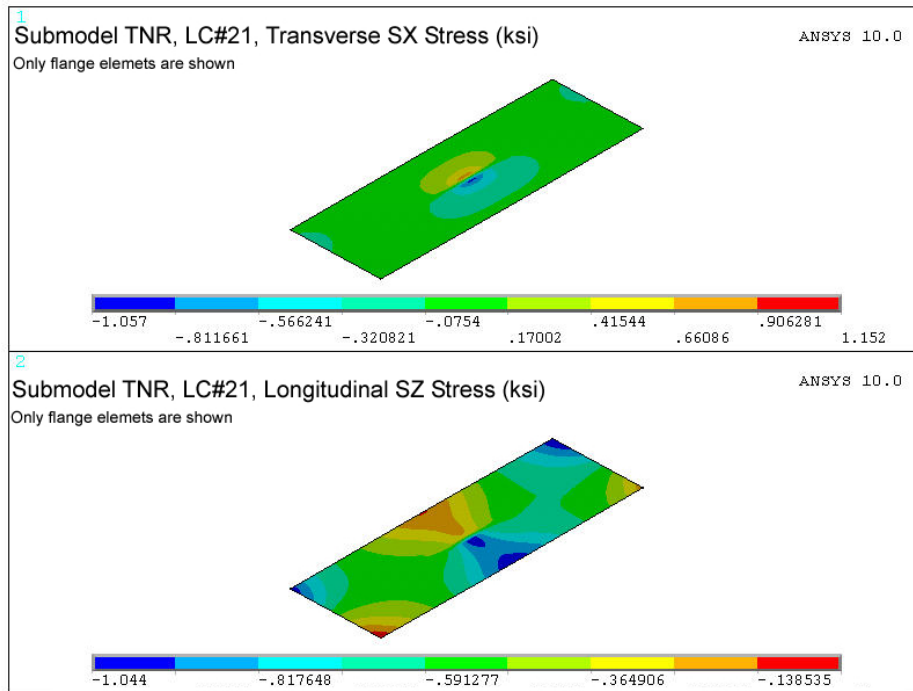


Figure 4.26: SX and SZ Stress Contours in Top Flange For Pre-Retrofit Model (TNR)

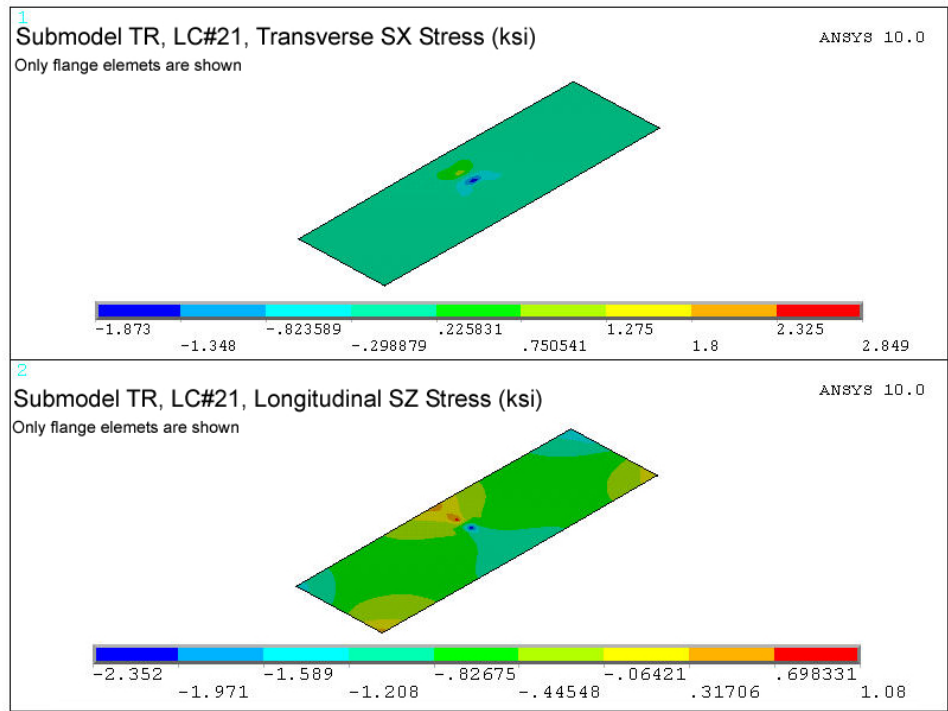


Figure 4.27: SX and SZ Stress Contours in Top Flange For Post-Retrofit Model (TR)

CHAPTER 5: BOTTOM CONNECTION ANALYSIS

The bottom flange is much less restraint for an out-of-plane movement compared to the top flange which is restrained by the deck. Consequently, the lower web gap experiences much lower web gap stresses compared to upper web gap. This is corroborated by the fact that no cracks have been observed in the lower web gap region. Cracks were only observed at the gusset plate-to-flange connection. These cracks were weld tears and they did not propagate into the parent material. This chapter discusses the results of pre and post retrofit bottom connection models and their calibration with the field test data

5.1 Bottom Flange Web Gap

5.1.1 Pre-Retrofit FE Analysis

In previous finite element studies [Zhao and Roddis 2004] on Tuttle Creek Bridge detailed analysis of the bottom flange connections at all critical cross frame connections was performed. The study showed that for a westbound truck the critical bottom flange connection is located at cross-frame A2W (see Figure 2.2) and so this connection is chosen for the present study. In this study the gusset plate was not included in the analysis and so the models were modified to include a gusset plate. This model is called model BNR (bottom no repair). The finite element submodel is shown Figure 5.1. In this model the flange-to-gusset connection is modeled by merging coincident nodes along the bold lines shown in the figure.

Figure 5.2 plots the SX, SY, and SZ stress variation of connection at A2W for the entire truck passage. The peak stresses occur at LC#22 when the truck is close to the mid-span, see Figure 5.3. The results indicate that the peak SX, SY, and SZ stresses

developed in the bottom web gap are 67%, 69%, and 62% lower than the top web gap stresses, respectively. This is because, compared to the top flange, the bottom flange is relatively free to move out-of-plane along with the stiffener plate which results in lesser distortion and hence lower stresses. Figures 5.4 to 5.6 show the web gap SX, SY, and SZ stress contours for bottom web gap at LC#22. Figure 5.7 shows the variation of out-of-plane displacement relative to the bottom flange along the 1.5 in at LC#22. The out-of-plane distortion in the bottom web gap is 67% lower than that in the top web gap (compared with model B2W).

5.1.2 Post-Retrofit FE Analysis

In the repair of the bottom connection (Type 'B' repair) the stiffener plate was welded to the gusset plate as shown in Figure 5.8. This will further reduce the lower web gap stresses. In addition to the gusset-to-flange fillet weld, the gusset plate is secured more firmly to the bottom flange by placing four pre-tensioned bolts as shown in Figure 5.8. Since the bottom connection at cross frame A2W was the most stressed, it is used to evaluate the Type 'B' repair. The model BNR is modified to include the positive connection between the stiffener and the gusset plate. The attachment was modeled by coupling all the DOFs of the nodes common to stiffener and gusset plates. The coincident nodes of flange and gusset near the location of the installed bolts are also merged, as shown in Figure 5.9. This modified model is called model BR (bottom repaired). Post retrofit stress distributions and out-of-plane displacements are shown in Figures 5.10 to 5.13. The results indicate a significant reduction in stresses. The out-of-plane displacements both before and after the repair are negligible. Table 5.1

summarizes the comparison of the critical stresses obtained from model BNR and model BR.

Table 5.1: Pre and Post Retrofit Peak FEA Stresses in Bottom Flange Web Gap

	Pre-Retrofit	Post-Retrofit	Change
SX (ksi)	4.0	1.3	-68%
SY (ksi)	10.0	1.4	-86%
SZ (ksi)	5.9	1.5	-75%

Note: Negative sign indicates percentage decrease after the retrofit

5.2 Bottom Flange Connection Model Calibration

The bottom connection web gap gages (G5 to G8) were placed on bottom connection of B2E (see Figure 2.2). The gage locations on the bottom connection are shown in Figure 4.34. Assuming that the effects of the traffic loading are symmetric, the effects of a westbound truck on girder B will be same as the effects of an eastbound truck on girder A. Therefore, under the action of an eastbound truck, the instrumented connection detail at B2E will have a similar behavior as the connection at A2W which analyzed for a westbound truck. Therefore, the results from the models BNR and BR are used for comparison with the eastbound truck test data.

5.2.1 Comparison with Pre-Retrofit Field Test Data

Table 5.2 shows the comparison of stresses obtained from the test data with that obtained from the FE analysis. The results from the FE analysis are extracted at nodes close to the gage locations shown in Figure 5.11. The peak stresses at the flange-to-web fillet weld connection are compared with the extrapolated values obtained from the gages.

Table 5.2: Pre-Retrofit Bottom Web Gap Stresses Obtained from Field Test Data and FE Analysis

Gage Number	Stress at Gage Location (ksi)		Peak Stresses (ksi)	
	Test	FEA	Test	FEA
G5	1.2	4.0	-2.4	-9.7
G6	-1.2	-4.3		(+75%)
G7	-2.5	-3.8	1.8	9.9
G8	-0.5	4.6		(+82%)

The FE results are conservative and the peak stresses are at least 75% higher than those observed in the field. The stresses are of low magnitudes and are all below the CAFL (10ksi).

5.2.2 Comparison with Post-Retrofit Field Test Data

Table 5.3 compares the post-retrofit test data with FE analysis. Table 5.4 summarizes the peak stresses obtained from the test and the FE results before and after the retrofit.

Table 5.3: Post-Retrofit Bottom Web Gap Stresses Obtained from Field Test Data and FE Analysis

Gage Number	Stress at Gage Location (ksi)		Peak Stresses (ksi)	
	Test	FEA	Test	FEA
G5	0.3	0.4	-0.7	-1.0
G6	-0.4	-0.4		
G7	-0.6	-0.1	-0.6	1.4
G8	-0.6	0.8		

Table 5.4: Comparison of Pre-Retrofit and Post-Retrofit Top Web Gap Peak Stresses Obtained from Extrapolated Gage Values with FE Analysis

	Pre-Retrofit Stress Near Horiz. Crack Tip (ksi)		Post-Retrofit Stress Near Horiz. Crack Tip (ksi)	
	Test	FEA	Test	FEA
Interior Side	-2.4	-9.7	-0.7 (-70%)	-1.0 (-89%)
Exterior Side	1.8	9.7	-0.6 (-100%)	1.4 (-86%)

Note: Negative sign indicates percentage decrease after the retrofit

The comparison shows that the type 'B' repair was very effective and the stresses in the bottom web gap are reduced significantly. The post retrofit FE results have a good match with the data and therefore, no further modifications are required for bottom connection FE model.

5.3 Bottom Flange-to-Gusset Plate Connection

5.3.1 Pre-Retrofit FE Analysis

Gusset plate was included in the bottom connection models to investigate the causes of the observed weld tears along the gusset-to-flange fillet weld and in the tack welds placed underneath the gusset plate. The welds were modeled by merging the coincident nodes between the flange and the gusset along the bold lines shown in Figure 5.1. Since, the frame members are built using truss elements only axial forces are available from the analysis of the coarse models. For each load case, the axial forces in the bracing members are transferred onto the gusset plate.

Figure 5.15 shows the transverse (SX) and longitudinal (SZ) stress distribution in the bottom flange at the critical LC#22. From the plots it can be observed that the peak stresses occur at weld terminations along the sides and at the termination of the tack weld. These hot-spots are caused by the prying action of the frame members which cause bending in the gusset plate [Marshall et. al., 2005]. The location of the peak stresses matches well with observed crack locations (see Figures 1.10 and 1.11). The vertical stresses (SY) are negligible.

5.3.2 Post-Retrofit FE Analysis

The type 'B' repair positively attaches the gusset plate to the by four pre-tensioned bolts in addition to the fillet welds. The tack weld from underneath the gusset

plate was also removed. The finite element model is shown in Figure 5.9. The peak SX and SZ stresses are shown in Figure 5.16. The peak stress develops near the nodes where brace member forces were applied and may be neglected. The results show that the peak SX and SZ stress near the weld terminations are reduced significantly by 42% and 47%, respectively. The retrofit does not affect the magnitudes of the forces transferred from the cross-frame members and does not affect the bottom flange stresses. The fact that the stresses distribution is now more uniform and there are no signs of stress concentration near the weld terminations, shows that the retrofit firmly attaches the gusset plate to the bottom flange and reduces the bending caused by the prying action. Thus corroborating the theory proposed in the earlier field report. Overall the stresses are of very low magnitudes and no further cracking is expected. Table 5.5 summarizes the peak stresses before and after the retrofit.

Table 5.5: Pre and Post Retrofit Peak FEA Stresses in Bottom Flange-to-Gusset Connection

	Pre-Retrofit	Post-Retrofit	Change
SX (ksi)	1.2	0.7	-42%
SZ (ksi)	1.9	1.0	-47%

Note: Negative sign indicates percentage decrease after the retrofit

5.4 Gusset Plate Connection Calibration

5.4.1 Comparison with Pre-Retrofit Field Test Data

Gage locations on the gusset plate in the pre-retrofit field test are shown in Figure 5.17. Gages G21 and G22 measured the stresses in the transverse and the longitudinal directions, respectively. Table 5.6 compares the stresses observed in the field with that obtained from the analysis. The analysis results show a good agreement with the test data thus validating the finite element model of gusset plate region. This

agreement also suggests that the assumptions made in the finite element model to transfer the forces from the frame members to the gusset plate used to transfer the brace member forces to the gusset plate are valid.

Table 5.6: Pre-Retrofit Gusset Plate Stresses Obtained from Field Test Data and FE Analysis

Gage Number	Stress at Gage Location (ksi)	
	Test	FEA
G21	-0.5	-0.5
G22	1.1	1.4

5.4.2 Comparison with Post-Retrofit Field Test Data

Three additional gages (G15, G13, and G16) were placed on the gusset plate during the post-retrofit field test as shown in Figure 5.17. Table 5.6 compares the measured stresses with that obtained from the analysis. These additional gages were placed to test the hypothesis presented in the previous field report [Marshall et. al., 2005] that the prying action of frame members result in bending of the gusset plate. The gages G15 and G16 placed at the top and bottom record strains of opposite signs, which indicate that the gusset plate bends under the prying action and supports the above hypothesis. The FE results at these gage locations do not predict bending. This is expected since truss elements were used to model the frame members (see section 5.3.1). Since the stresses are of very low magnitudes it is reasonable to ignore this error and so no further modifications are required for the bottom flange-to-gusset model.

Table 5.6: Pre-Retrofit Gusset Plate Stresses Obtained from Field Test Data and FE Analysis

Gage Number	Stress at Gage Location (ksi)	
	Test	FEA
G21	-0.1	-0.1
G22	1.0	1.0
G15	-0.3	-0.1
G13	1.1	-0.1
G16	-0.2	-0.1

5.5 Summary

The analysis results from model BR match well with the field test data and demonstrates the effectiveness of the Type 'B' repairs. Before retrofit, the stresses developed in the bottom flange web gap are much lower than those developed in the top flange web gap, which explains the field observation that no cracks were found in the lower web gap. The newly installed retrofit further reduces the stresses and so no fatigue cracks are expected to initiate in the lower web gap. The analysis shows that prior to the retrofit, peak stresses develop near the weld terminations at the flange-to-gusset connection, but after the retrofit the stress distribution is more uniform and there is no stress concentration at the connection. This indicates that the retrofit is effective in reducing the prying action and eliminating the hot-spots on the connection.

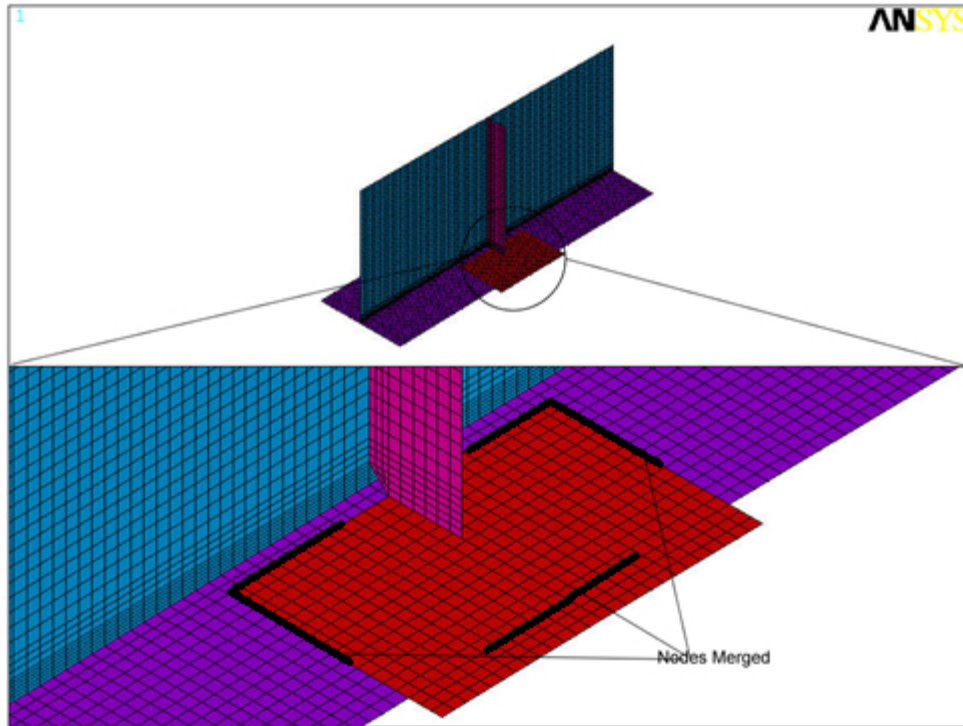


Figure 5.1: Pre Repair Bottom Connection Submodel, BNR

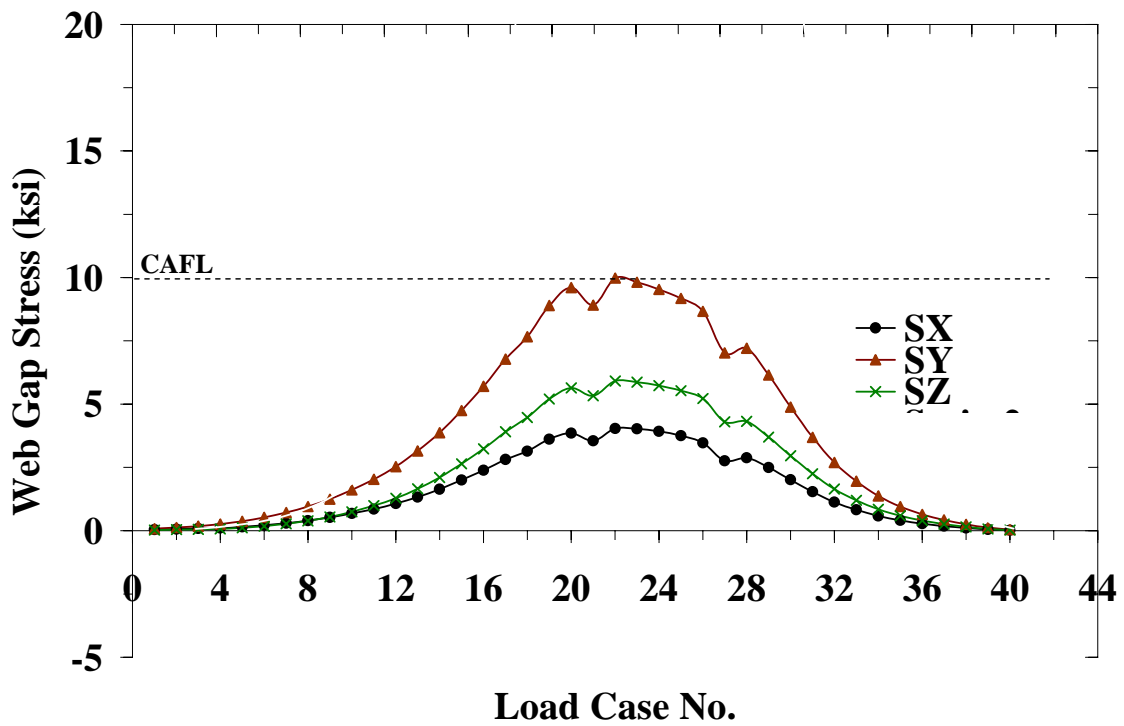


Figure 5.2: Stress Variation in Bottom Web Gap Model (BNR)

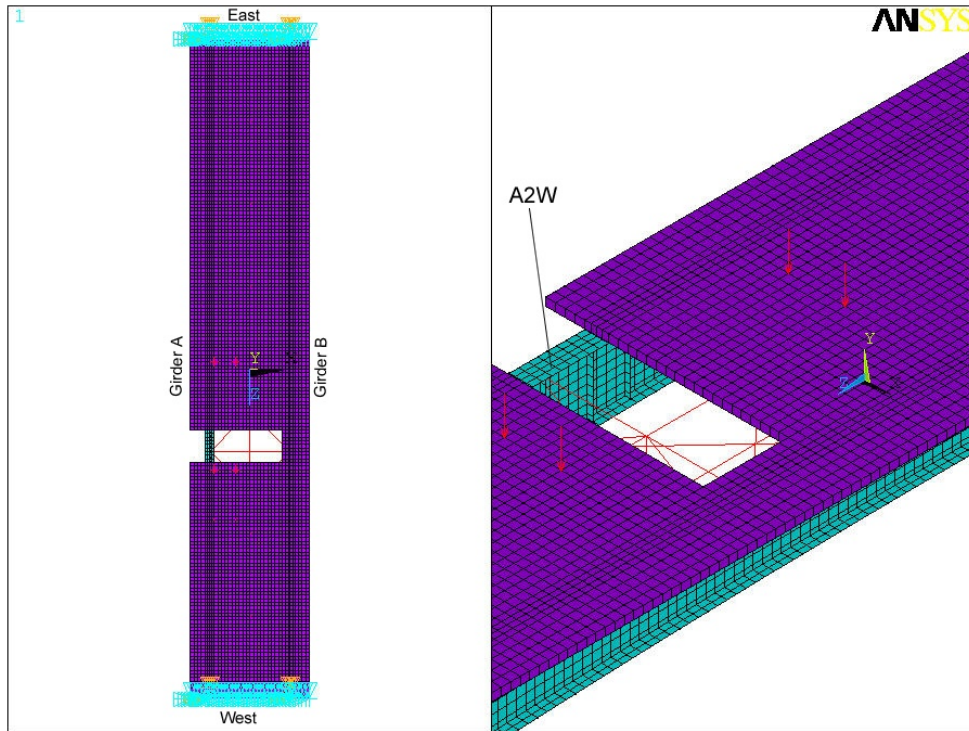


Figure 5.3: Truck Position for Load Case # 22

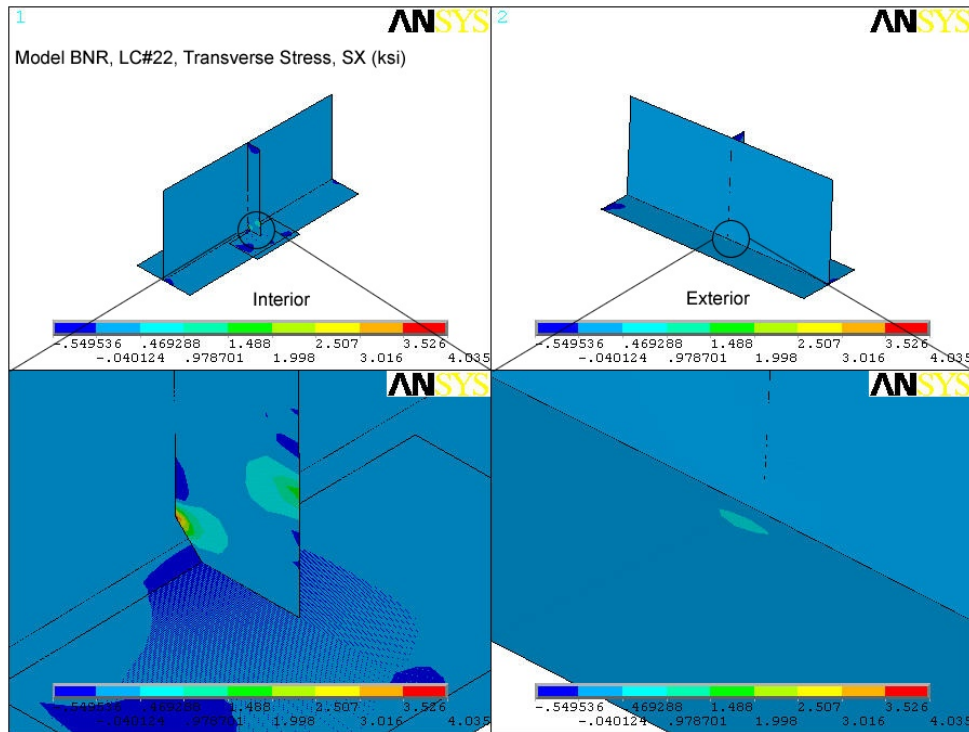


Figure 5.4: SX Stress Contours in Pre-Retrofit Bottom Flange Web Gap

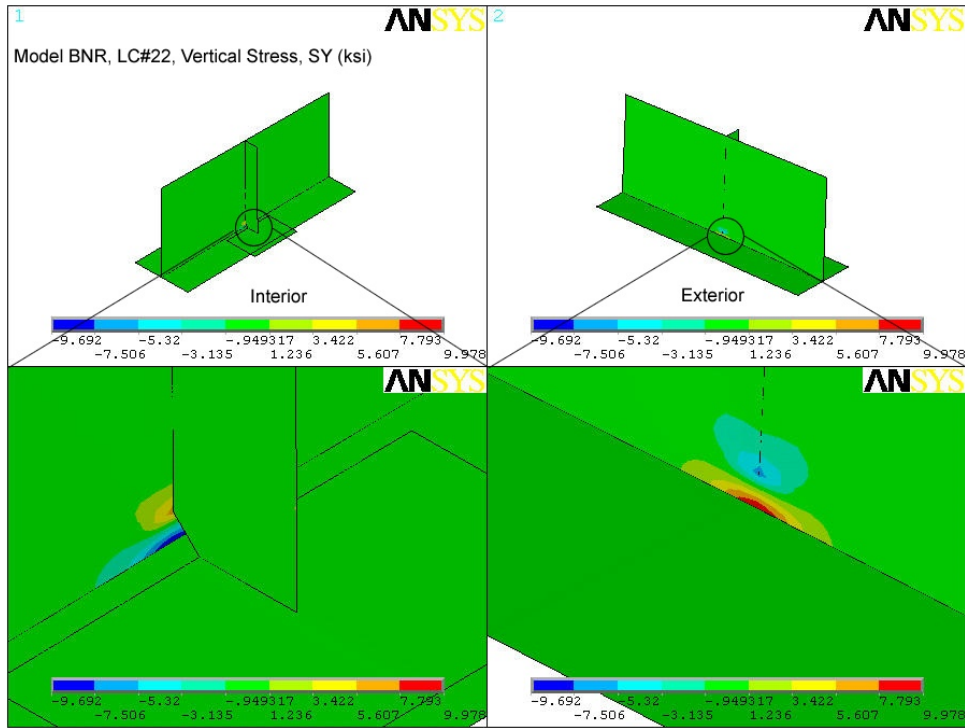


Figure 5.5: SY Stress Contours in Pre-Retrofit Bottom Flange Web Gap

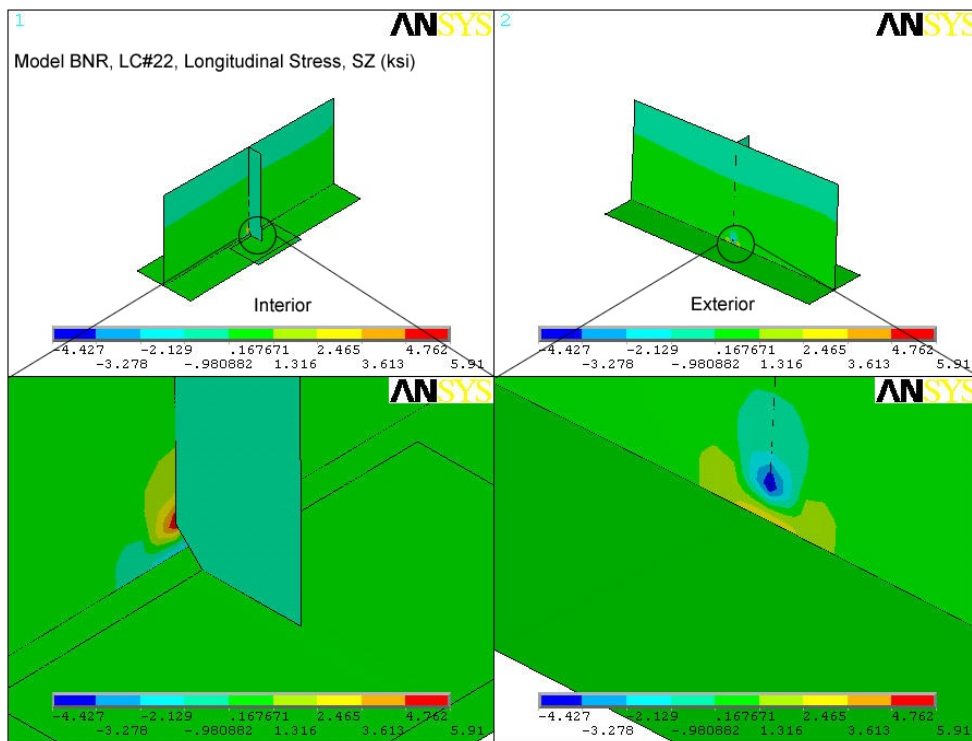


Figure 5.6: SZ Stress Contours in Pre-Retrofit Bottom Flange Web Gap

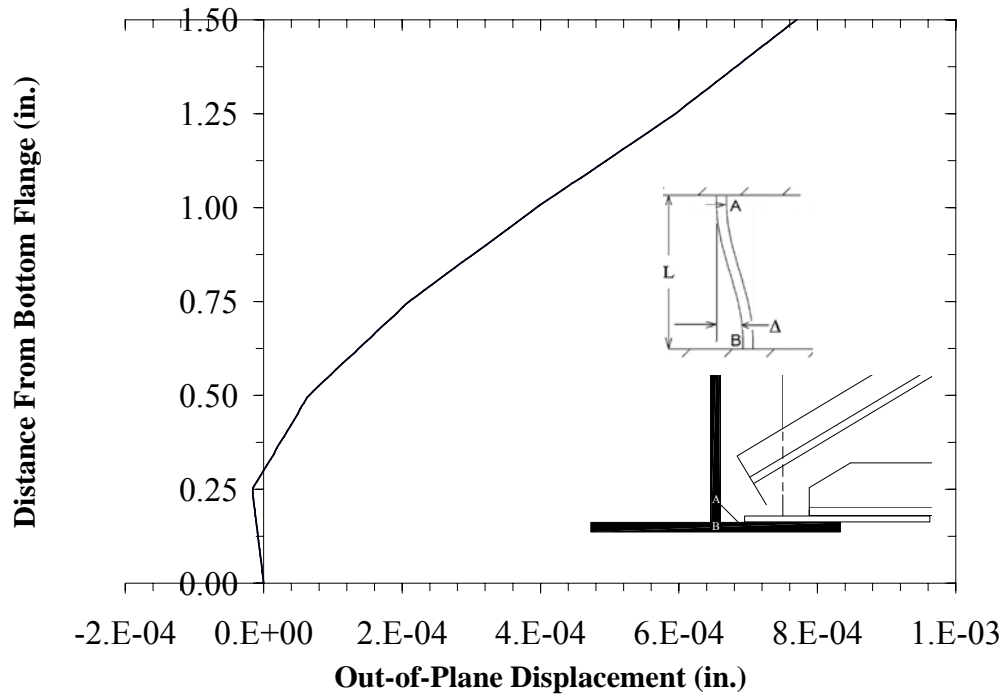


Figure 5.7: Out-of-Plane Displacement in Pre-Retrofit Bottom Flange Web Gap

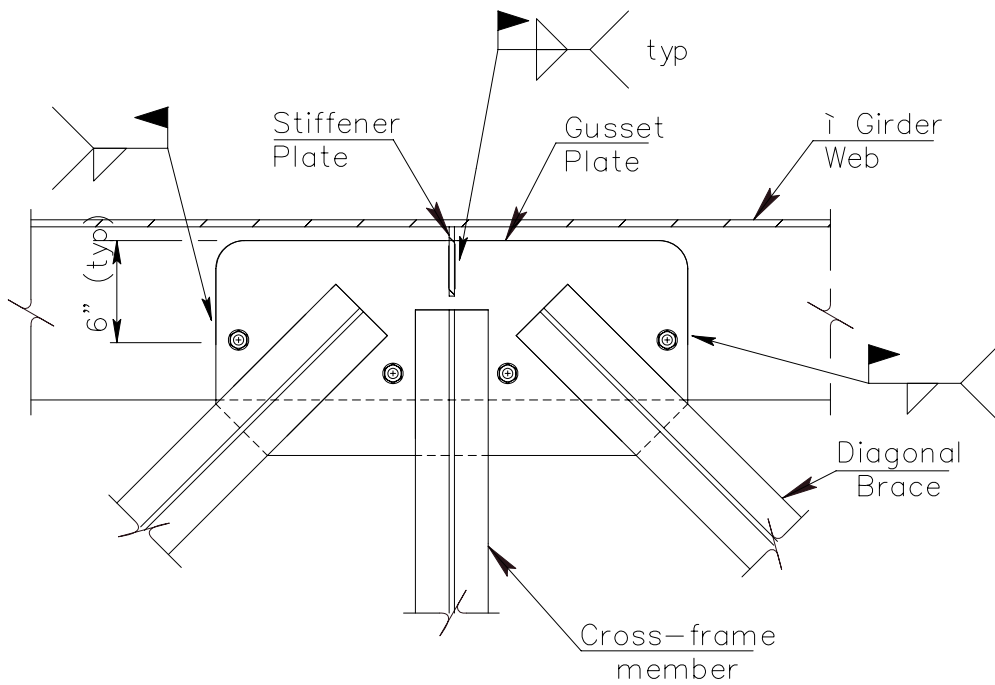


Figure 5.8: Type 'B' Repair for Bottom Flange Connection

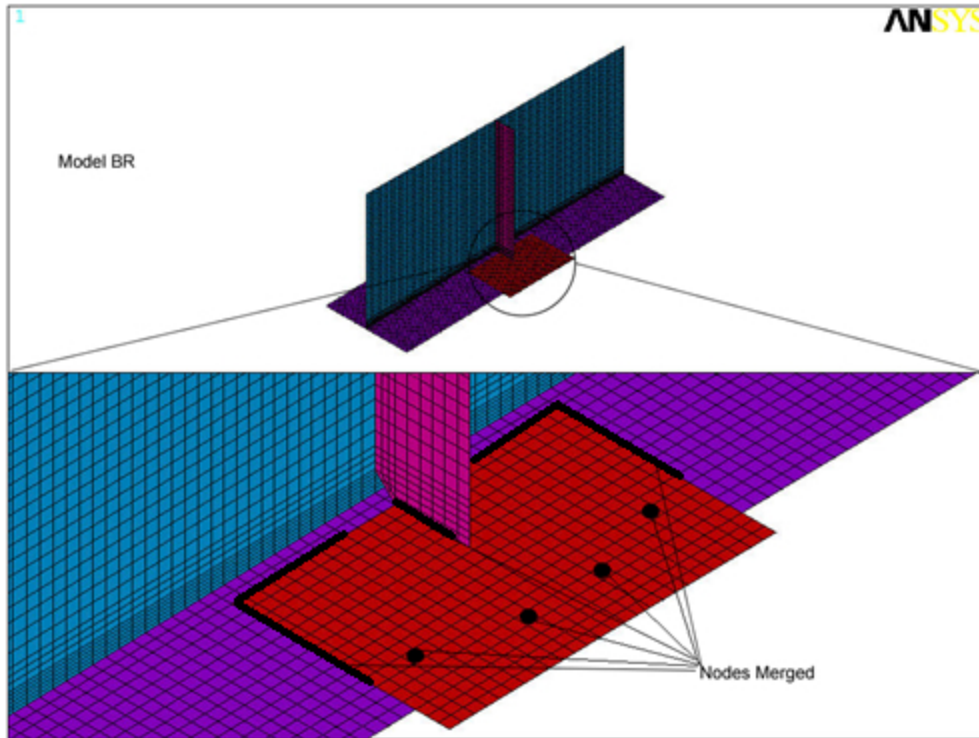


Figure 5.9: SX Stress Contours in Post-Retrofit Bottom Flange Web Gap

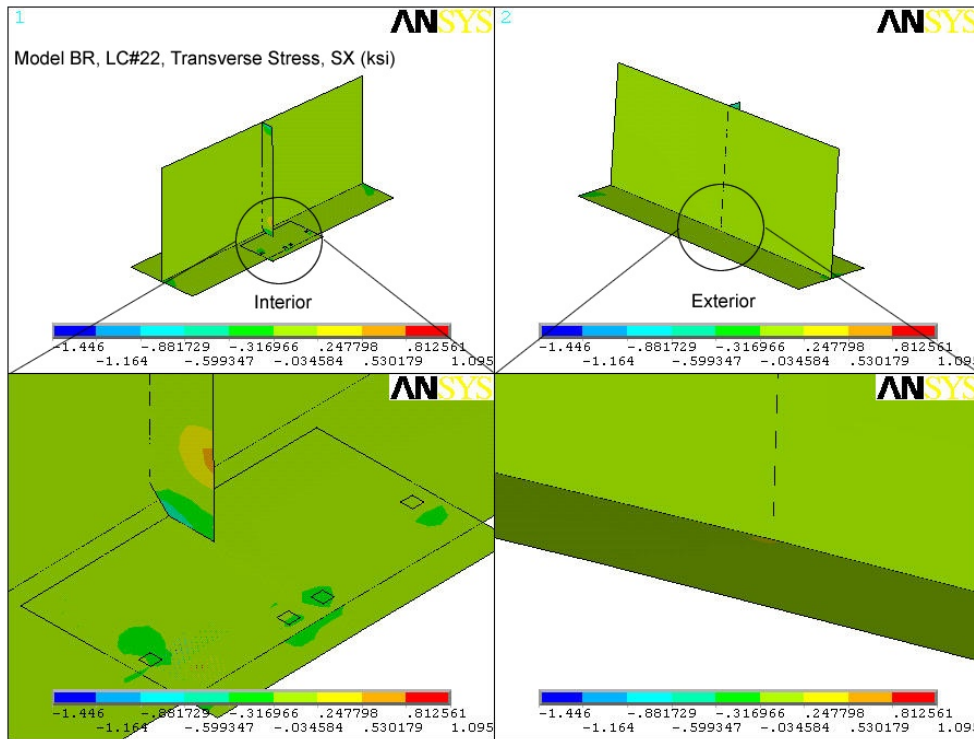


Figure 5.10: SX Stress Contours in Post-Retrofit Bottom Flange Web Gap

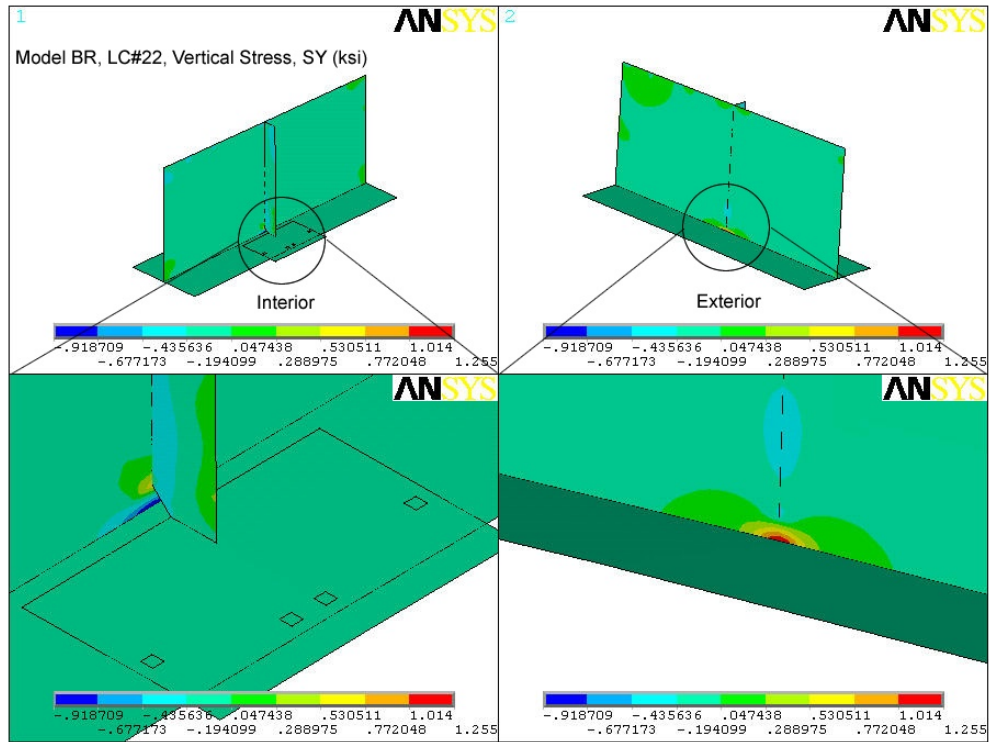


Figure 5.11: SY Stress Contours in Post-Retrofit Bottom Flange Web Gap

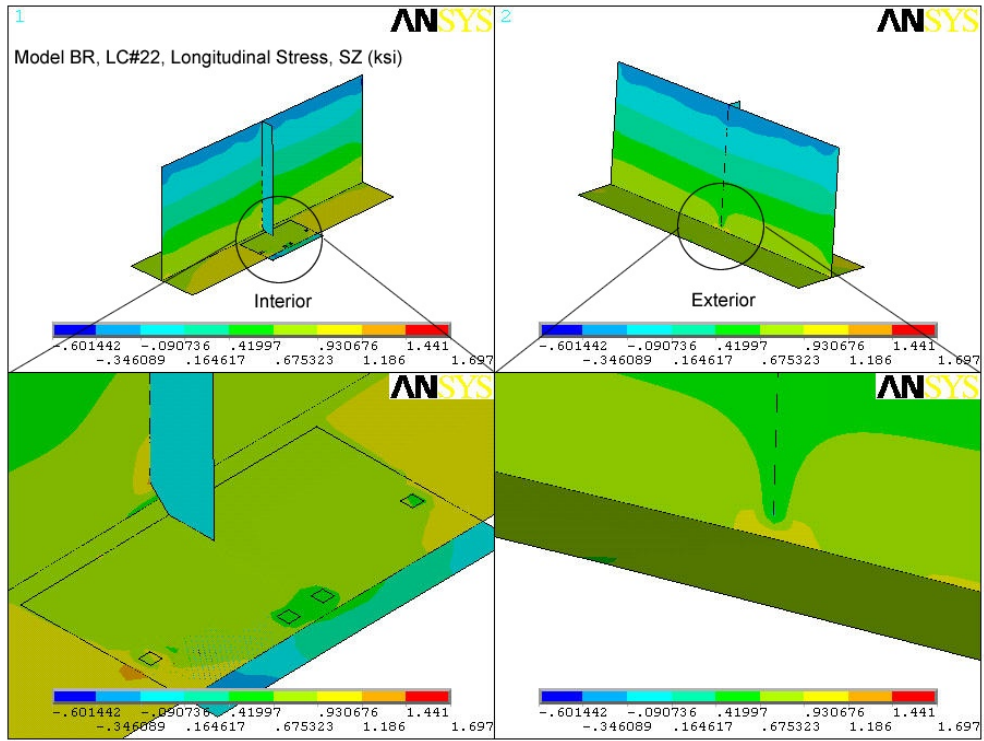


Figure 5.12: SZ Stress Contours in Post-Retrofit Bottom Flange Web Gap

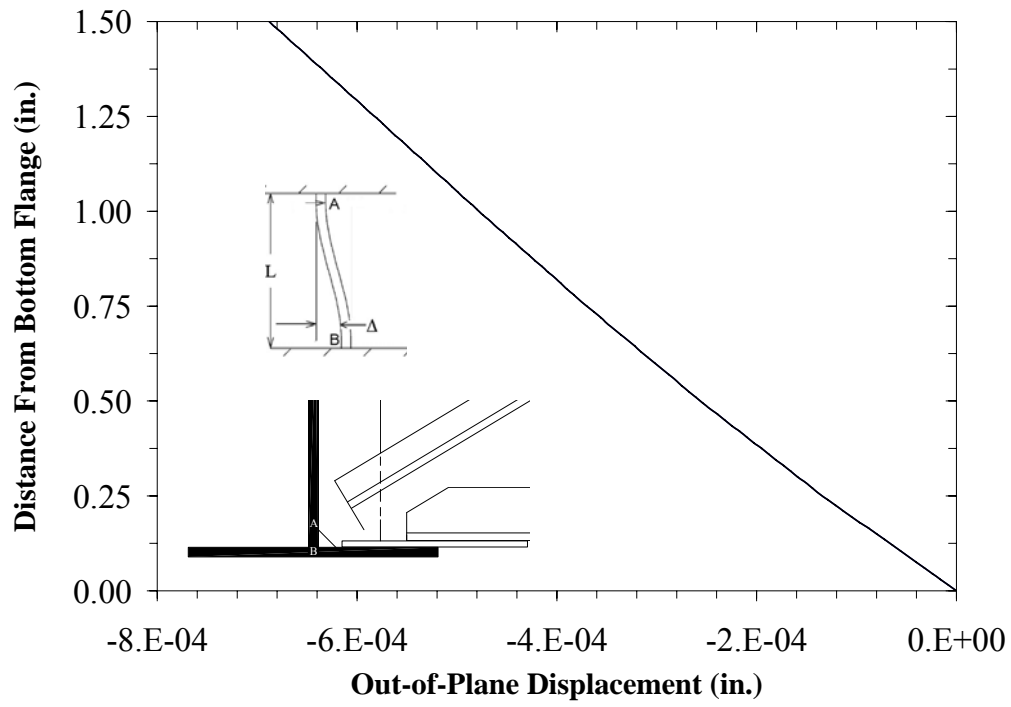
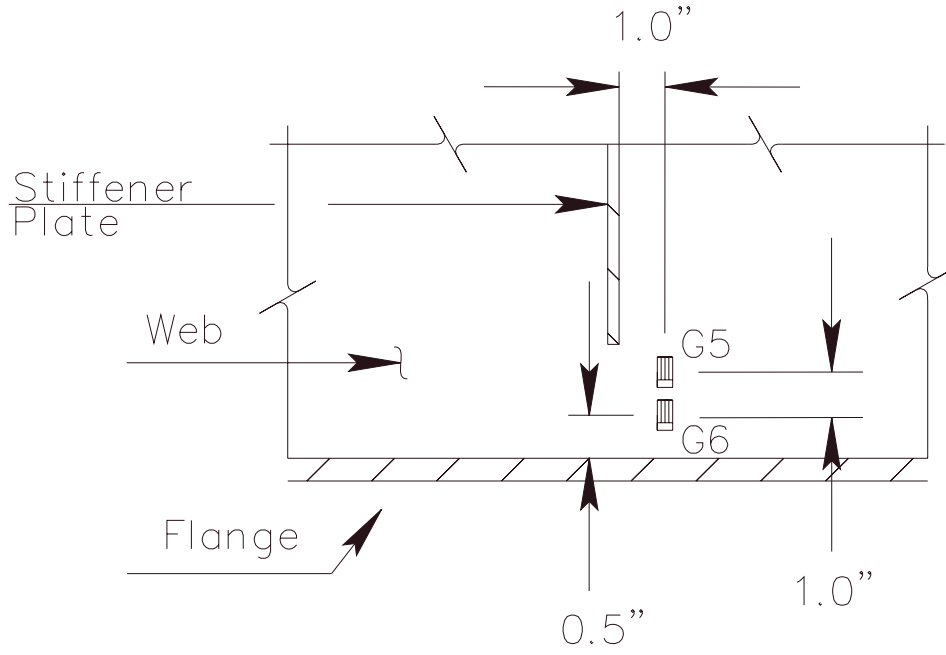
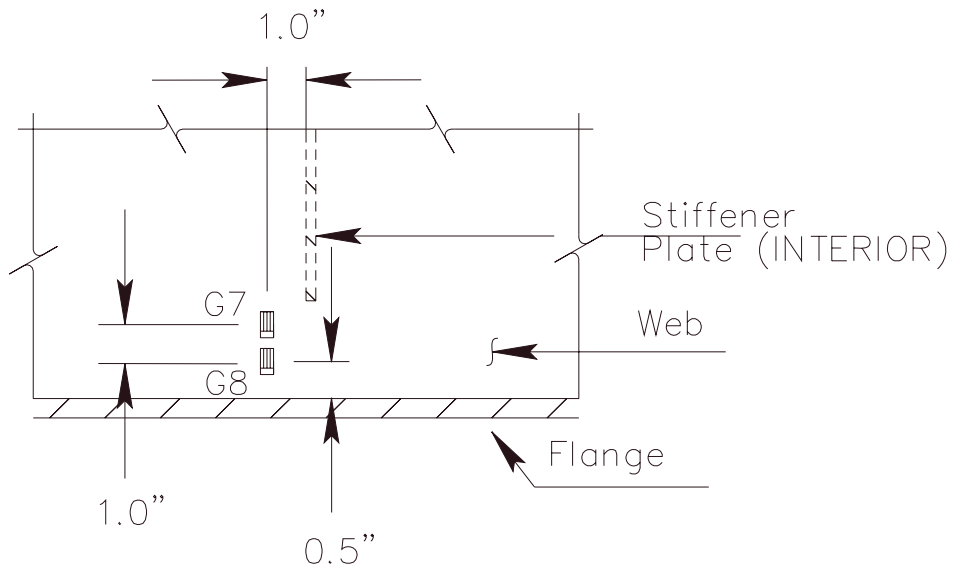


Figure 5.13: Out-of-Plane Displacement in Post-Retrofit Bottom Flange Web Gap



(a) Exterior Side of the Girder



(b) Interior Side of the Girder

Figure 5.14: Location of Bottom Flange Web Gap Gages, G5 to G8

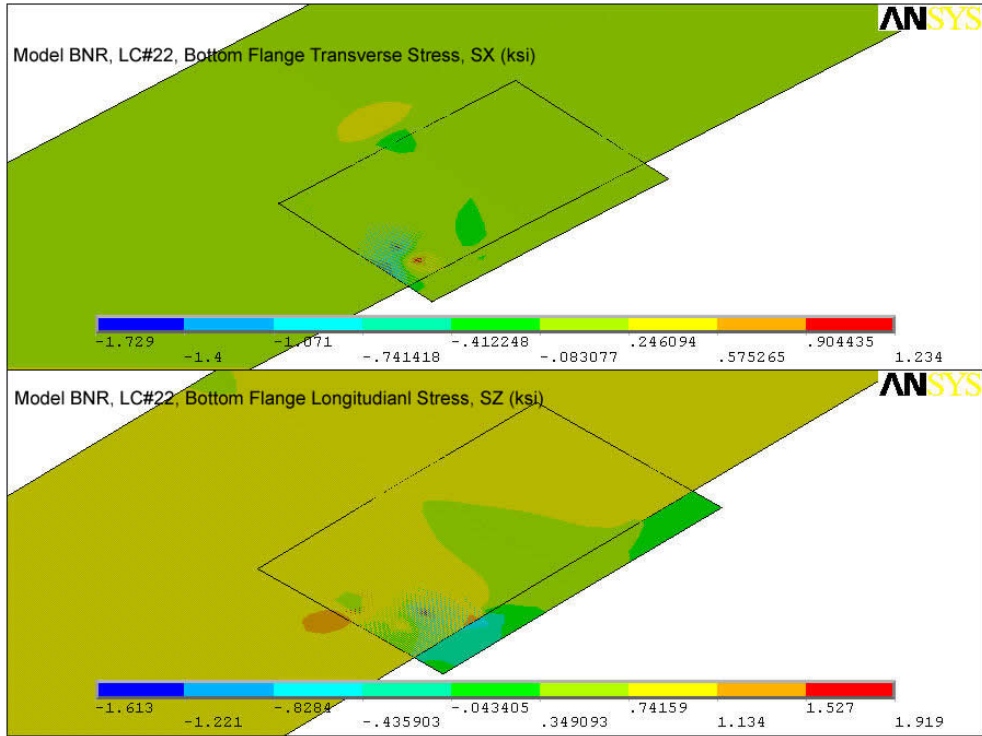


Figure 5.15: SX and SZ Stress Distribution in Pre-Retrofit Bottom Flange-to-Gusset Connection

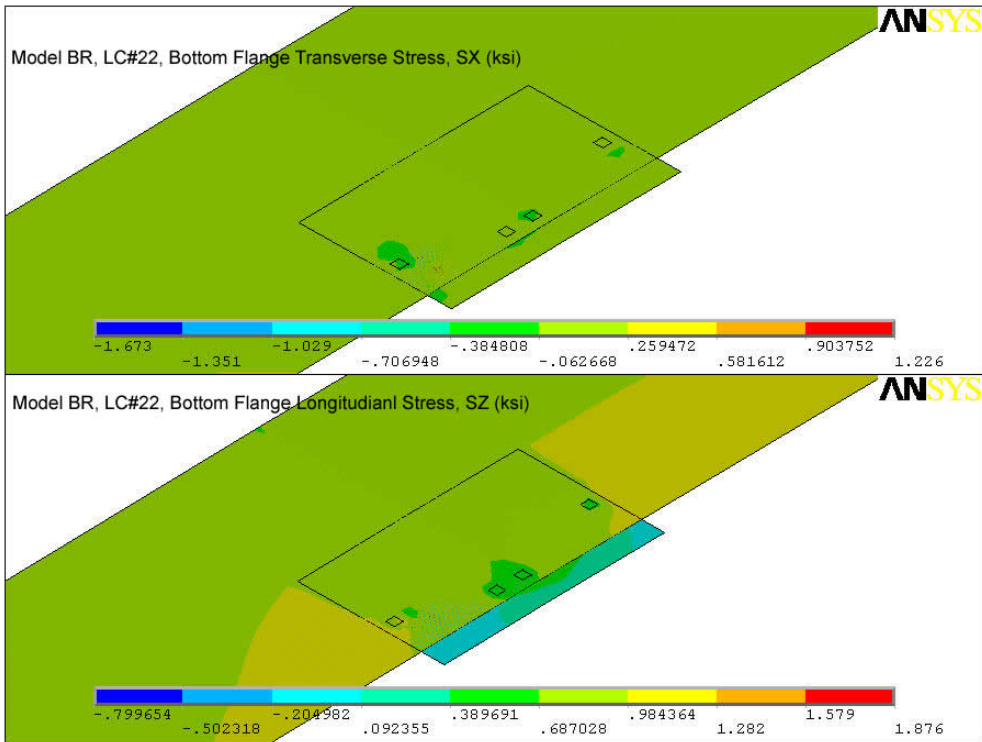


Figure 5.16: SX and SZ Stress Distribution in Post-Retrofit Bottom Flange-to-Gusset Connection

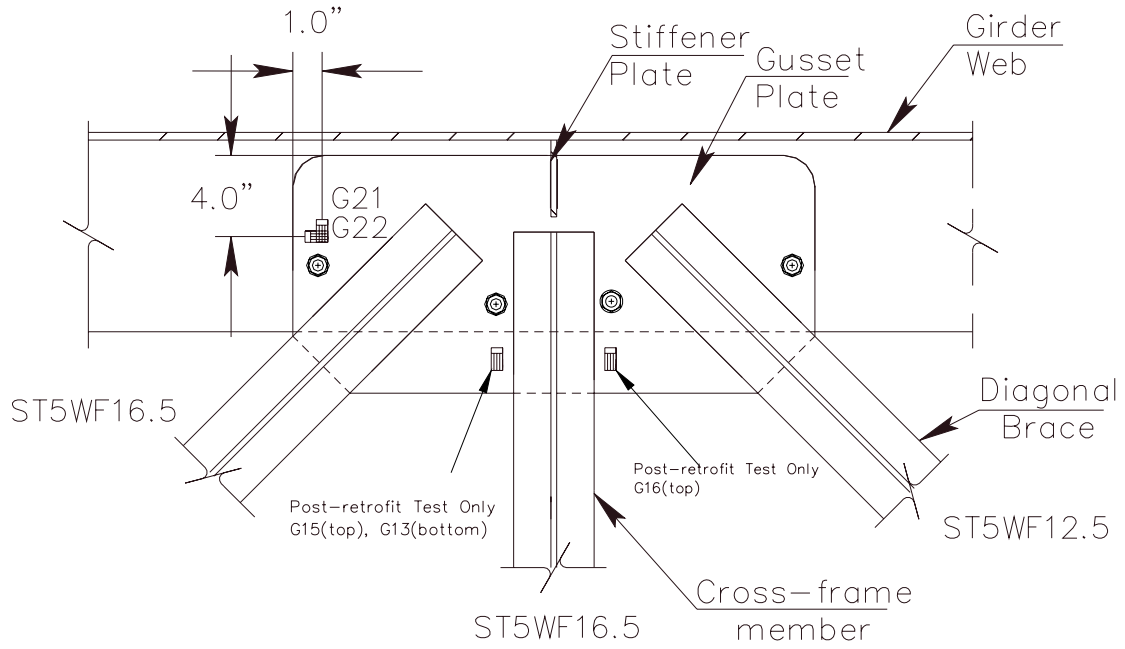


Figure 5.17: Location of Gusset Plate Gages

CHAPTER 6: ANALYSIS OF COPE HOLE

6.1 Description

Cope holes are fatigue critical details and cracks were found to originate at many such details on the bridge. Cope holes are located at all the flange splices on the bridge girders. There are four cope holes per girder for every interior span without hinge, two per girder for an interior span with hinge, two for the two end spans.

Type 'D' repair consists of increasing the existing $\frac{3}{4}$ inch radius hole to $1\frac{1}{2}$ inch minimum radius hole to remove the existing cracks and then performing UIT around the hole, see Figure 6.1.

6.2 FE Analysis

A typical cope hole location was chosen for this study. The cope hole studied was located on bottom flange of Girder-A on the east end, see Figures 6.2. Four different submodels were built with different hole radii the existing $\frac{3}{4}$ inch, proposed minimum $1\frac{1}{2}$ inch, 2 inch, and $2\frac{1}{2}$ inch. The models are named CP075, CP150, CP200, and CP250. The objective of the study was to investigate the effect of increasing the radius on the stress distribution around the hole. Figure 6.3 shows submodel for $1\frac{1}{2}$ inch radius cope hole.

6.2.1 Results

For a west bound truck the global analysis indicate that the maximum stress around the cope occurs when the leading axle is close to the mid-span, for LC#14. Figure 6.4 shows the global deflection of the bridge span for this load case. In the figure the displacements are scaled and the solid deck and the frame elements are hidden for clarity. From the isometric and the elevation views in the figure it is clear that the

bottom flange experiences an out-of-plane deformation which, affects the stress distribution around the cope hole. The stresses increase when the cope hole radius is increased.

To further understand this behavior an independent FE model for a simply supported beam was built. The beam was allowed to deflect only in its own plane. All the nodes were restricted for an out-of-plane deflection. A cope was modeled at the mid span and the beam was loaded to produce maximum stresses at the mid-span. The cope hole radius was varied and the effect of increasing the radius on the stress distribution is studied. This is discussed in detail in section 6.2.1.2.

6.2.1.1 Comparison of Results for the Cope Hole Submodels

Figure 6.5 shows a vector plot of maximum principal stress around the cope. The cracks found near the cope hole originate from the weld toe of the existing field splice and are oriented normal to the direction of the major principal stress, see Figures 6.1 and 6.5. Table 6.1 summarizes the maximum principal stress values for the four models. The maximum in all the models occurs for LC # 14. Figures 6.6 to 6.9 show the principal stress distribution at LC#14 around the cope hole for the four submodels.

Table 6.1: Maximum Principal Stress Around the Cope for LC # 14

	Model CP075	Model CP150	Model CP200	Model CP250
Cope Radius (in)	¾	1½	2	2½
S ₁ (ksi)	1.22	1.48	1.53	1.73

The maximum stress increase with the increase in cope radius this is attributed to the out-of-plane movement of the flange. Increase in radius will generally reduce the stress concentration factor at the rim of the hole. This concentration factor is usually calculated by assuming that there is no out-of-plane movement. In the present case a

significant out-of-plane displacement is present affecting the stress distribution around the cope.

The location of the cope is near the point of contraflexure and thus the stresses around the cope area are very low. The slight increase in stresses due to increase in cope radius will be not affect the fatigue life of detail since the increased stresses are well below the CAFL of 10 ksi for a category C detail. UIT treatment is done around the cope and it will further improve the fatigue characteristics. Any further cracking in this area is thus not expected.

6.2.1.2 Simply Supported Beam With a Cope at Mid-Span

The objective of this analysis is to demonstrate that in the absence of any out-of-plane displacement increase in cope radius will reduce the stresses around the rim of the hole. A simply supported beam with a cope mid-span is analyzed for point load at the center. Three FE models analyzed are for cope radius $\frac{3}{4}$, $1\frac{1}{2}$, and $2\frac{1}{2}$ inch, see Figure 6.10. Table 6.2 summarizes the maximum stress values around the cope from these analyses.

Table 6.2: Maximum Principal Stress Around the Cope in a Simply Supported Beam

	Model BM075	Model BM150	Model BM250
Cope Radius (in)	$\frac{3}{4}$	$1\frac{1}{2}$	$2\frac{1}{2}$
S_1 (ksi)	21.0	19.6	18.0

Figures 6.11 to 6.13 show the major principal stress distribution for the three models. In this case when out-plane-movement is not present the stresses decreases with the increase in cope radius. This validates assertion of section 6.2.1.1 that the out-of-plane movement of the bridge girder is the cause of increasing stress with the increase in cope radius.

6.3 Summary

The cope locations are near the point of inflection for the girder and the stresses around the cope are very low. Due to the out-of-plane movement of the bottom flange stresses around the rim of the hole increase with increase in cope radius. However, the increase is not significant and the stresses are well below the CAFL (10 ksi) for category C and the UIT treatment will further improve the fatigue life of the detail.

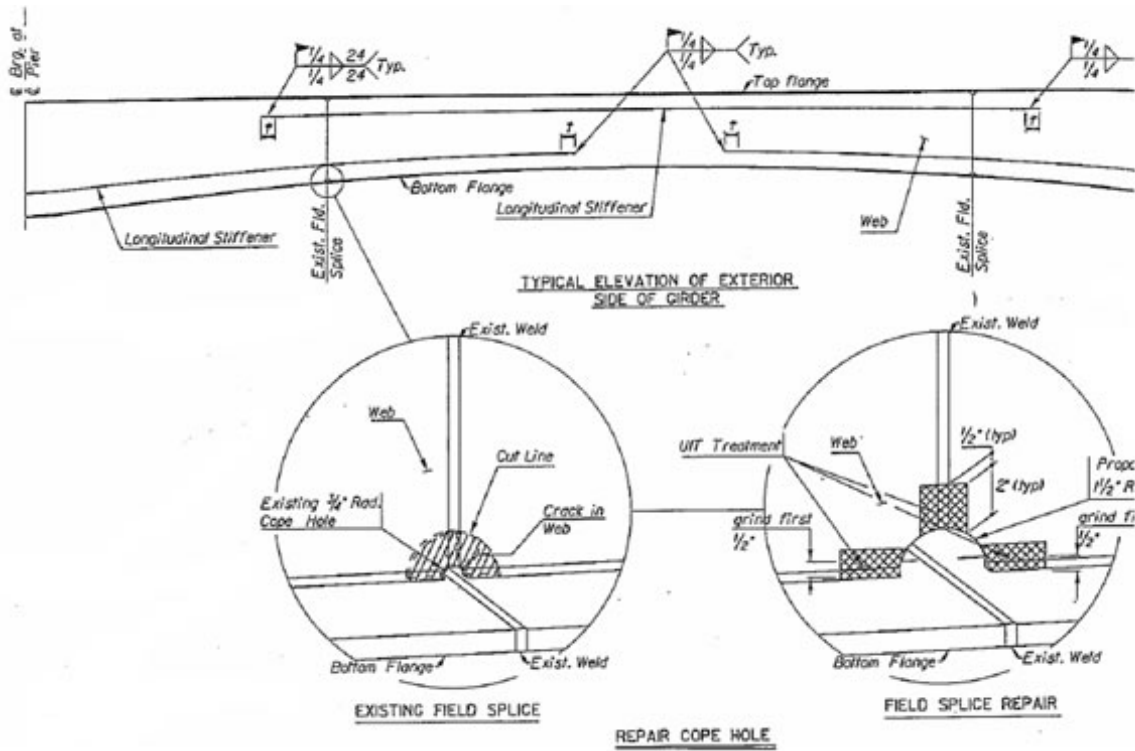


Figure 6.1: Type 'D' Repair

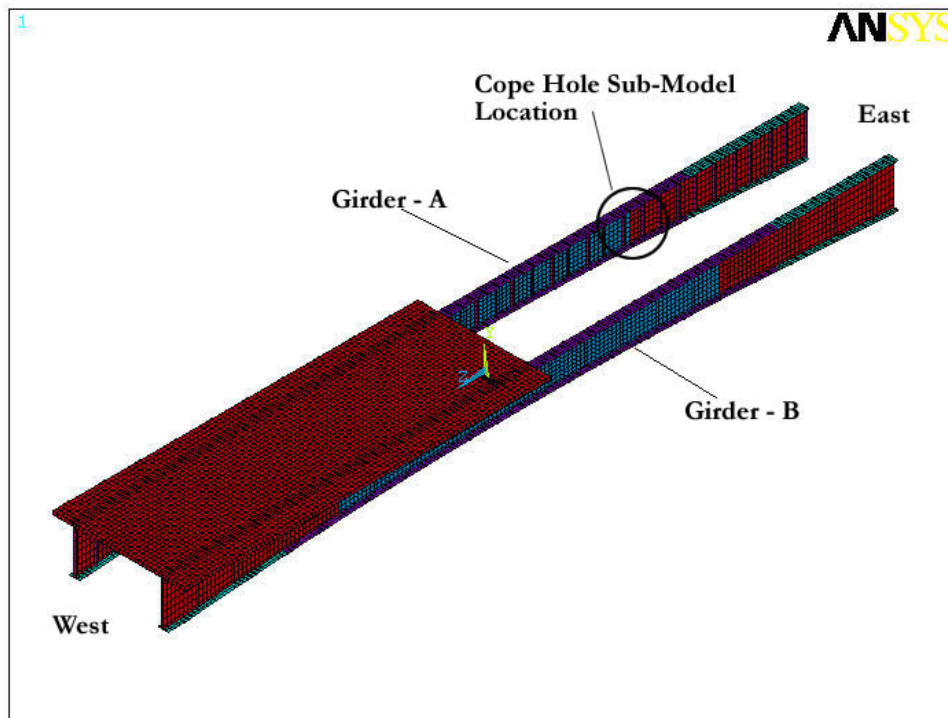


Figure 6.2: Global Model Showing the Location of the Cope Hole Submodel

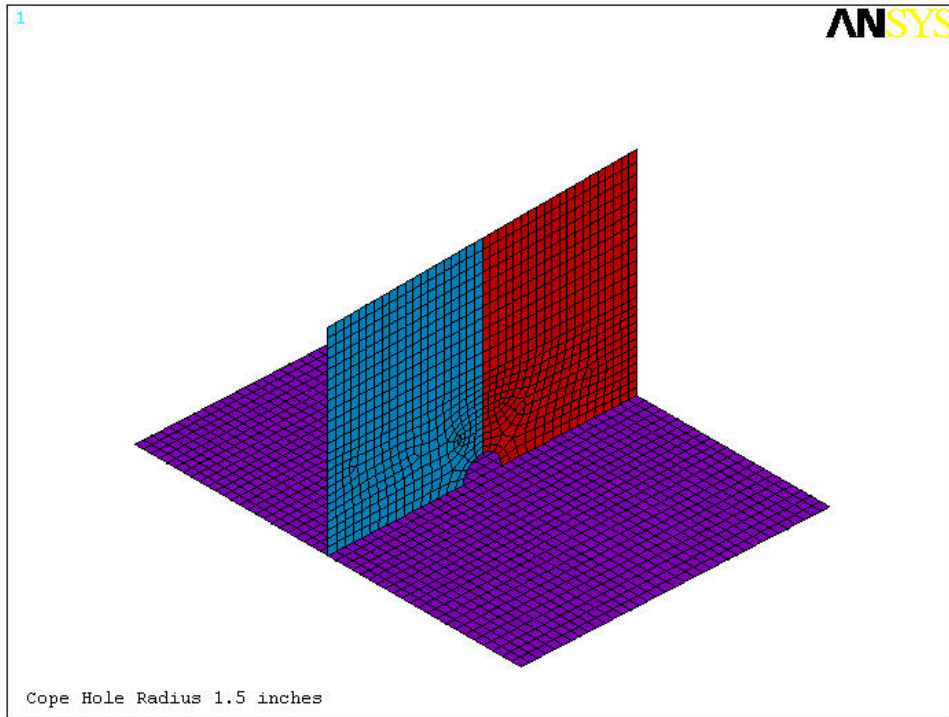


Figure 6.3: Cope Hole Submodel With Radius 1½ inch, Model CP150

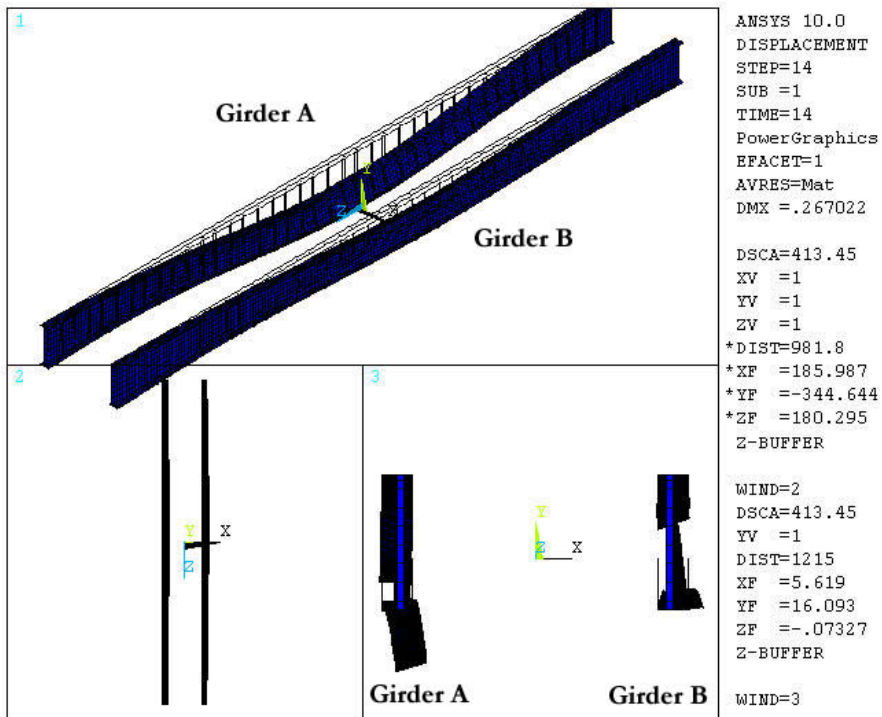


Figure 6.4: Global Deflection at Load Case # 14

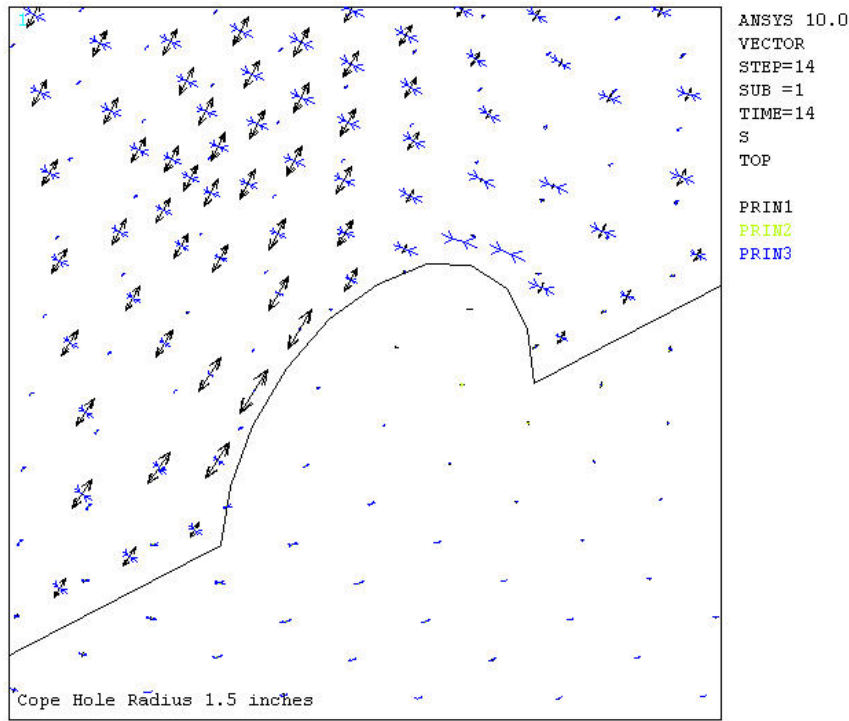


Figure 6.5: Vector Plot of Maximum Principal Stresses for Model CP150 LC#14

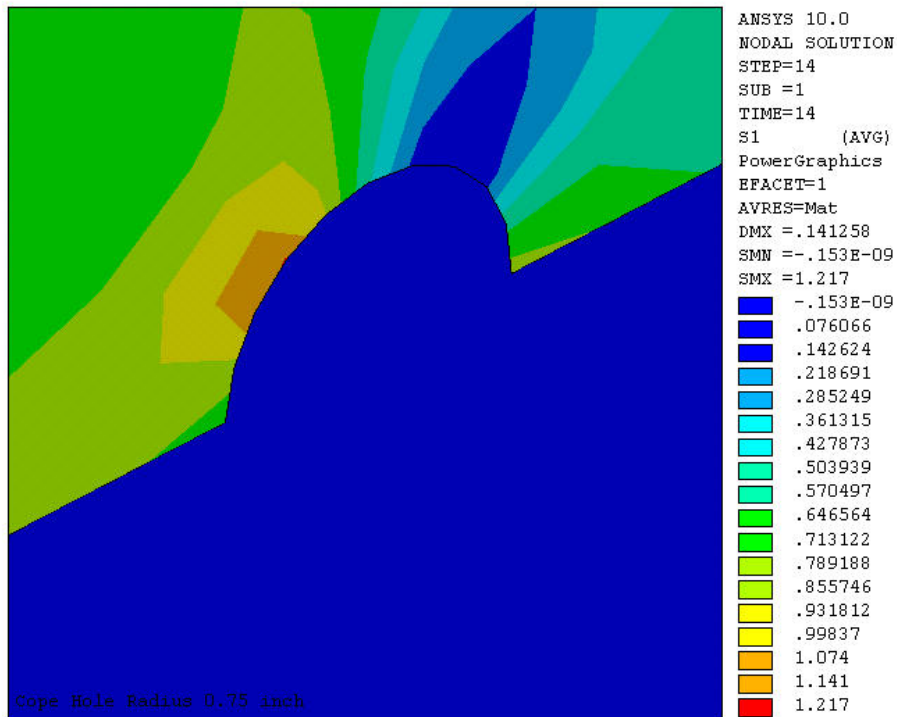


Figure 6.6: Maximum Principal Stress for Model CP075 LC#14

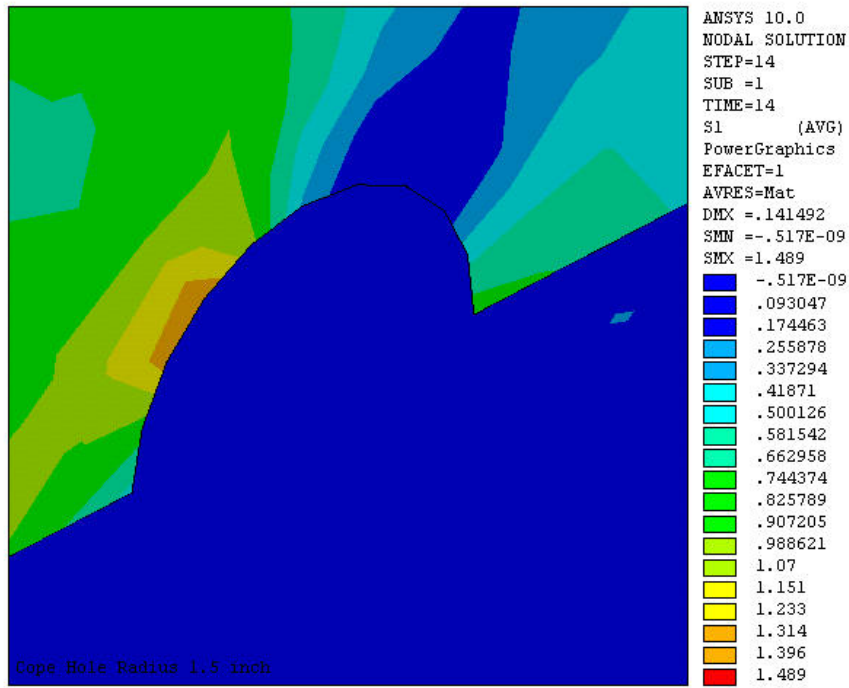


Figure 6.7: Maximum Principal Stress for Model CP150 LC#14

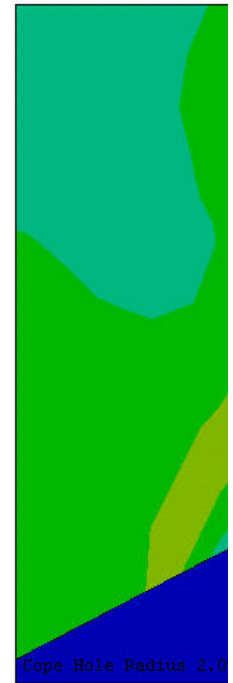


Figure 6.8: Maximum Principal Stress for Model CP200 LC#14

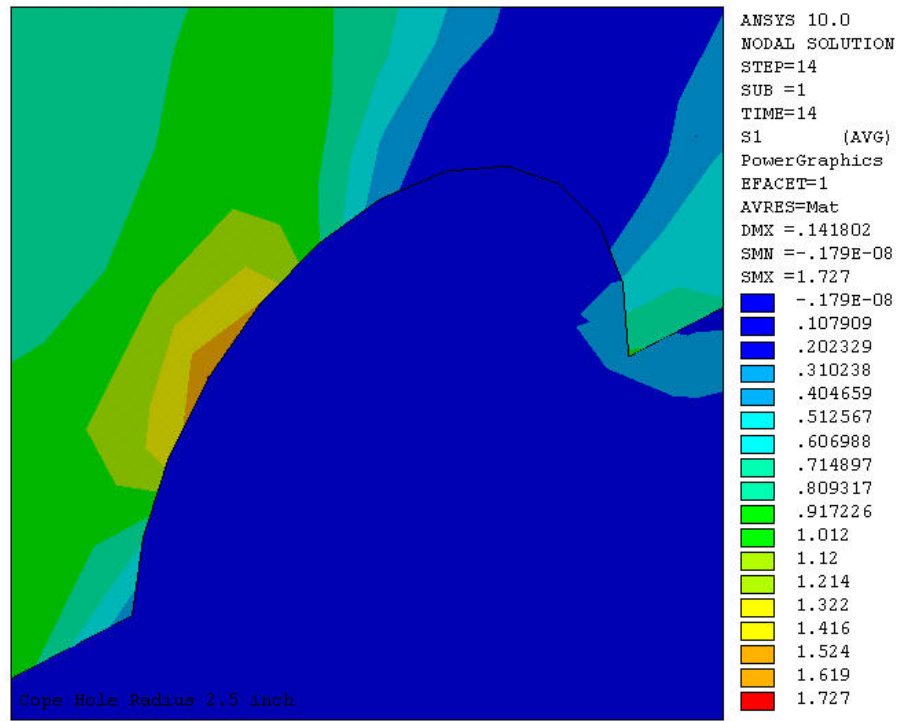


Figure 6.9: Maximum Principal Stress for Model CP250 LC#14

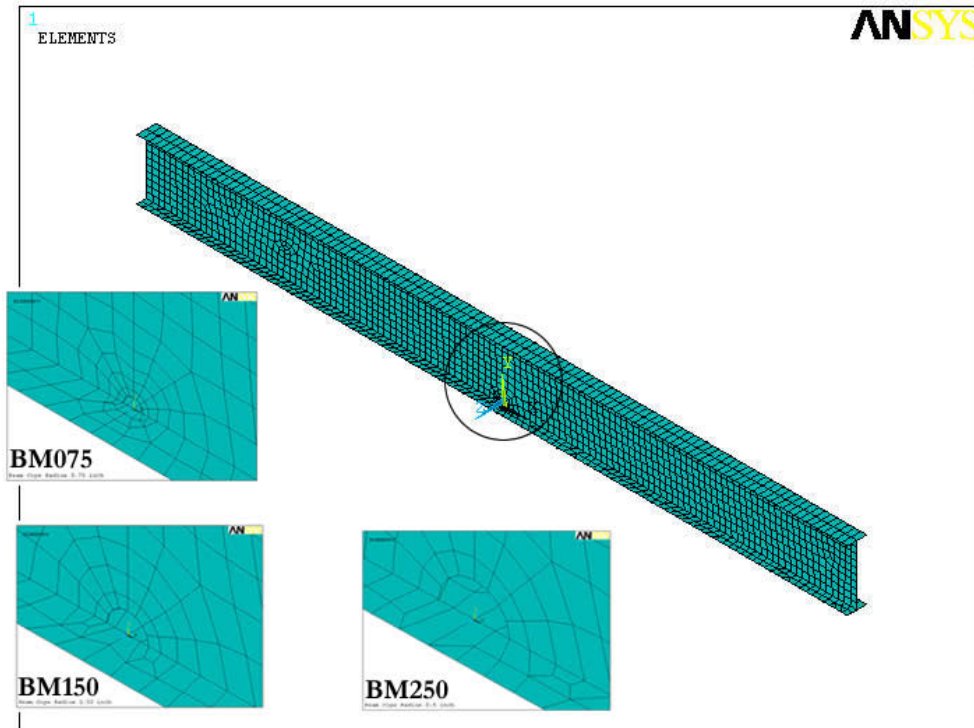


Figure 6.10: FE Models for Simply Supported Beam With a Cope at Mid-Span

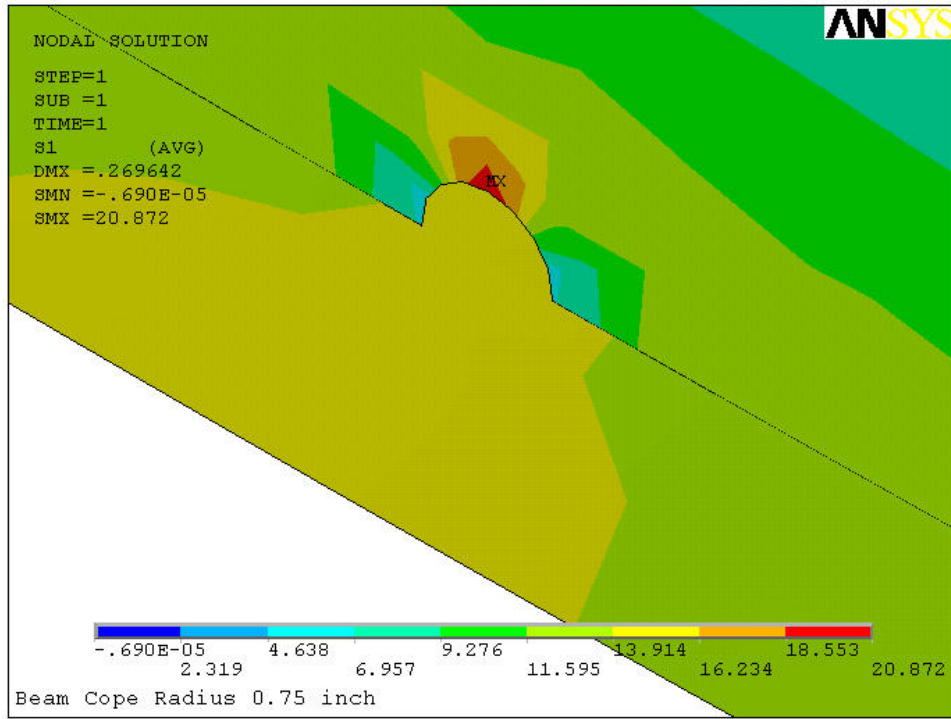


Figure 6.11: Maximum principal Stress for Model BM075

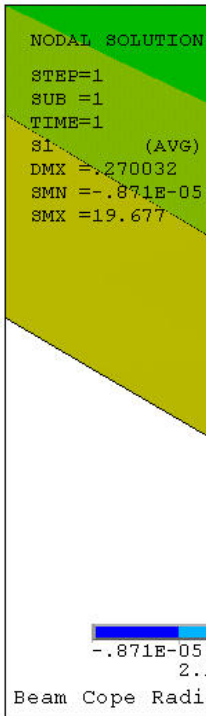


Figure 6.12: Maximum principal Stress for Model BM150

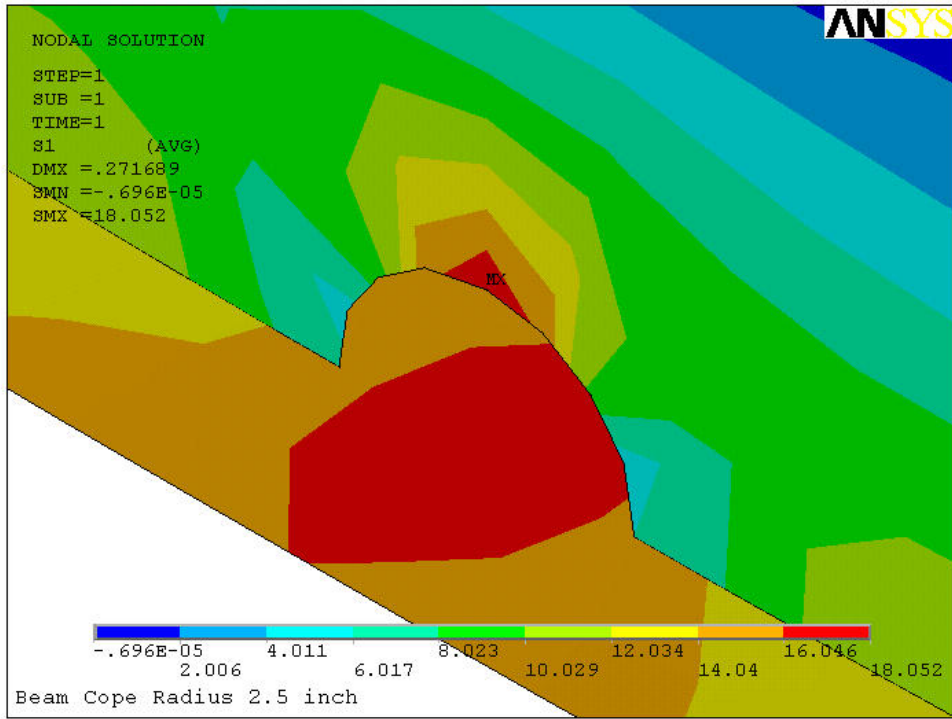


Figure 6.13: Maximum principal Stress for Model BM250

CHAPTER 7: ANALYSIS OF “NEW” HORIZONTAL CRACK

7.1 Description

During a site inspection of September 2005 a horizontal crack was found at the fourth cross-frame of span 14. The crack originated at cope end of the stiffener clip. It was not a through thickness crack and was detected by a Magnetic Particle test. It can be seen as a faint green line between the two large red lines in Figure 7.1. The crack is straight and horizontal extending approximately 2 to 3 inches on both sides of the stiffener. The fact that the crack does not turn downwards in shape of an horseshoe suggest that the crack is not a typical distortion-induced fatigue crack. The crack is oriented in the direction of rolling and it is possible that the crack originated at a mill flaw. A $\frac{3}{4}$ inch diameter retrofit hole was drilled at the tip of the crack.

To investigate the effect of Type ‘A’ repair on the stress distribution around the observed crack FE analysis was done. A worst case scenario was investigated by including a through thickness crack in the most critical top connection FE model. Stop holes were also included in the model. Further, addition of an outside stiffener was also studied as an alternative retrofit strategy.

7.2 FE Analysis

7.2.1 Through Crack with Stop Holes

The model TR is modified to include a through thickness crack extending 2 inches on both sides of the stiffener plate. Stop holes were also included in the model as shown in the figure 7.2. This new model is called TRNC (top repaired with crack). Table 7.1 compares the maximum stresses obtained from the model TR (Figures 4.15 to 4.17) are compared with the maximum stresses obtained from this model. The

stresses are reported at two locations, at the slot end (point 1) and at the crack tip (point 2) as shown in Figure 7.2. The stress distributions SX, SY, and SZ around the crack are shown in Figures 7.3 to 7.5, respectively. The hot spot shifts to the crack tip from the slot end and the stresses decrease due to this redistribution. The stresses are less than CAFL (10 ksi) and further cracking is not expected at these locations.

Table 7.1: Stresses at the slot end (point 1) and at the crack tip (point 2)

	Model TR	Model TRC	
		Slot End	Crack Tip
SX (ksi)	5.3	0.8	0.0
SY (ksi)	6.2	1.1	2.8
SZ (ksi)	4.3	0.0	2.1

7.2.1.1 Comparison with Fisher's Formula

As described earlier in chapter 4, Fisher proposed a criterion to determine the size of the stop holes to arrest fatigue cracks, this is repeated here for convenience

$$\frac{\Delta K}{\sqrt{\rho}} = \frac{\Delta \sigma \sqrt{\pi A_r}}{\sqrt{\rho}} \leq 4 \sqrt{\sigma_y} \quad \text{Equation 7.1}$$

where: ΔK = stress intensity factor range = $\Delta \sigma \sqrt{\pi A_r}$;

ρ = radius of the drilled stop hole (in);

A_r = half the equivalent crack length after rehabilitation;

$\Delta \sigma$ = nominal stress range (ksi);

σ_y = yield strength of the material (ksi).

For $\Delta \sigma = 2.8$ ksi, $A_r = 2.375$ in, and $\sigma_y = 36$ ksi the minimum stop hole diameter required to arrest crack growth is 0.2 in. The existing hole diameter of 0.75 in. should therefore be sufficient to arrest the crack growth.

7.2.2 Outside Stiffener

The FE model TR was modified to include an outside stiffener. The connection plate was mirrored to build the TRO (top repaired with outside-stiffener) model, Figure 7.6. The objective of this analysis was to investigate the effect increased stiffness around the region of the observed new crack. The model is first analyzed without including the through crack. The results are compared with the previous results obtained from the TR model (Figures 4.15 to 4.17). The crack will be included in the model only if the stress distribution is significantly modified by adding the outside stiffener plate. Table 7.2 compares the maximum stress results from these models. The stress distributions around the slot end are shown in Figures 7.7 to 7.9. It can be observed that the addition of an outside stiffener has no significant effect on the stress values. Thus, if the crack is included in this model the stress distribution will not be significantly different from that obtained from model TRNC described in section 7.2.1.

Table 7.2: Stresses at the Slot End (point 1) Before and After Including the Outside Stiffener

	Model TR	Model TRO
SX (ksi)	5.3	3.4
SY (ksi)	6.2	6.4
SZ (ksi)	4.3	5.4

7.3 Summary

The crack is not a typical distortion-induced fatigue crack. It is believed to be originated at a mill flaw. Type 'A' repair reduces the stresses significantly in the web gap region. The presence of the crack redistributes the hot-spot from the root of the slot to the crack tip. The maximum crack opening stress (SY) at the crack tip is 2.8 ksi is significantly lower than the CAFL (5 ksi). The diameter of the drilled stop hole is one-half times larger than minimum required by Fisher's criterion. Type 'A' repair combined with

drilled stop holes thus provides an effective retrofit and further crack growth in this region is not expected.

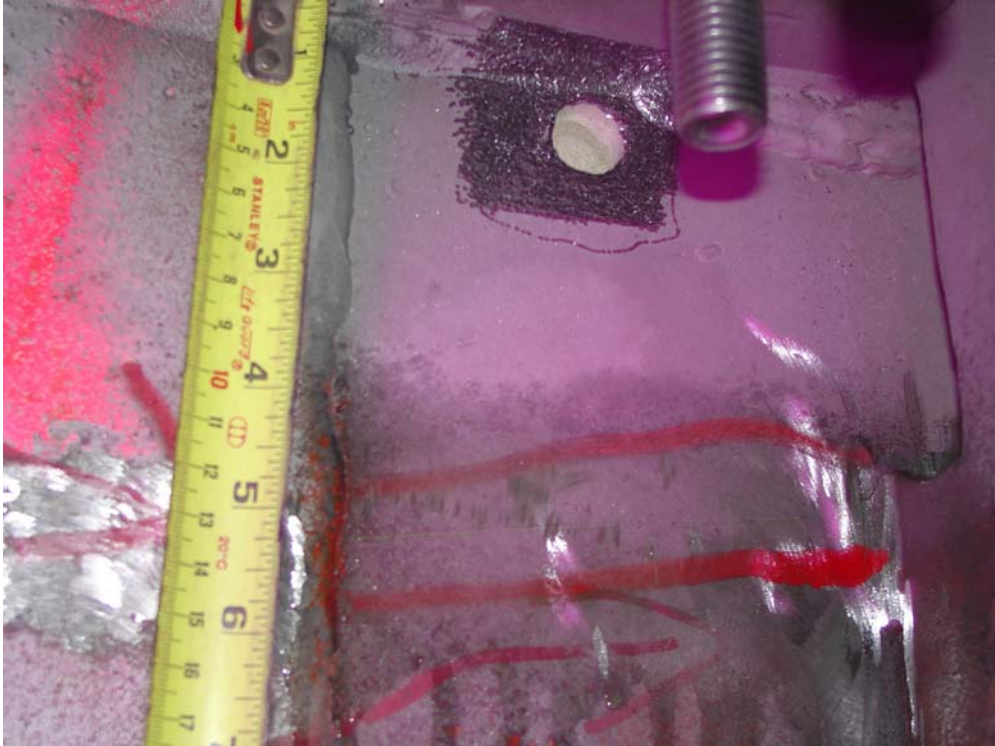


Figure 7.1: New Crack Observed in June 2005

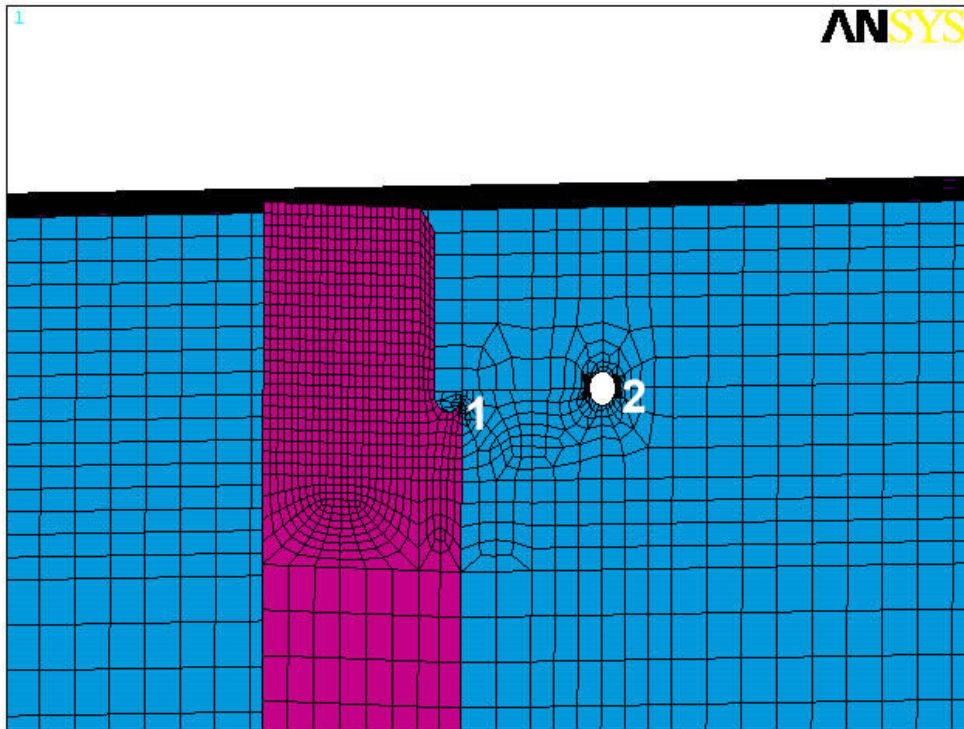


Figure 7.2: Submodel TRNC

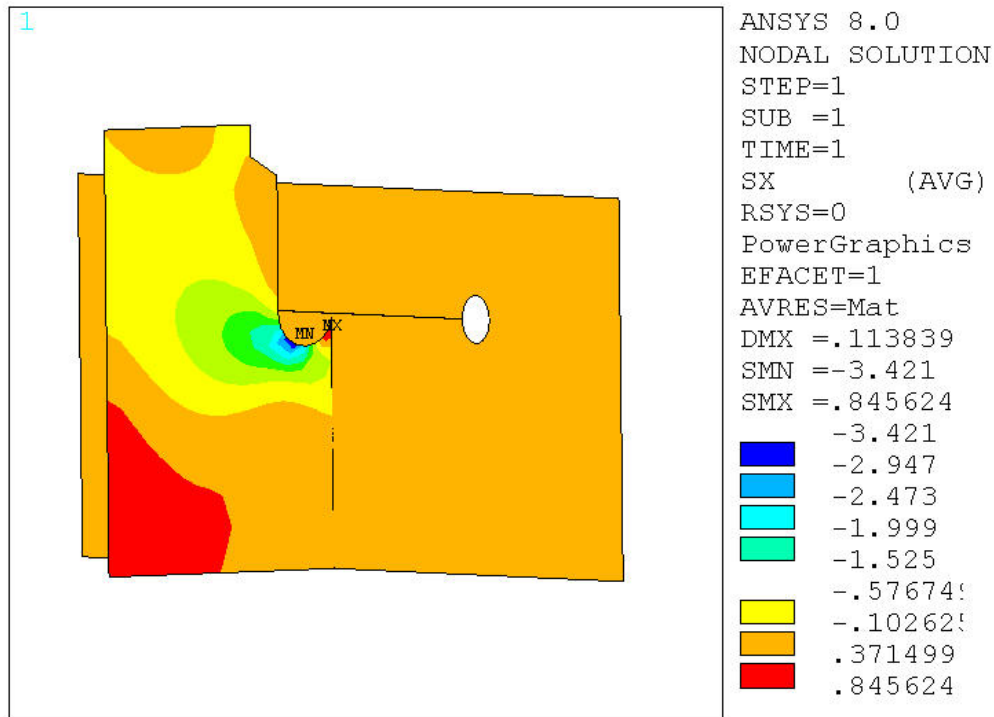


Figure 7.3: SX Stress Contours in Top Web Gap After Including a 4 inch Through Crack

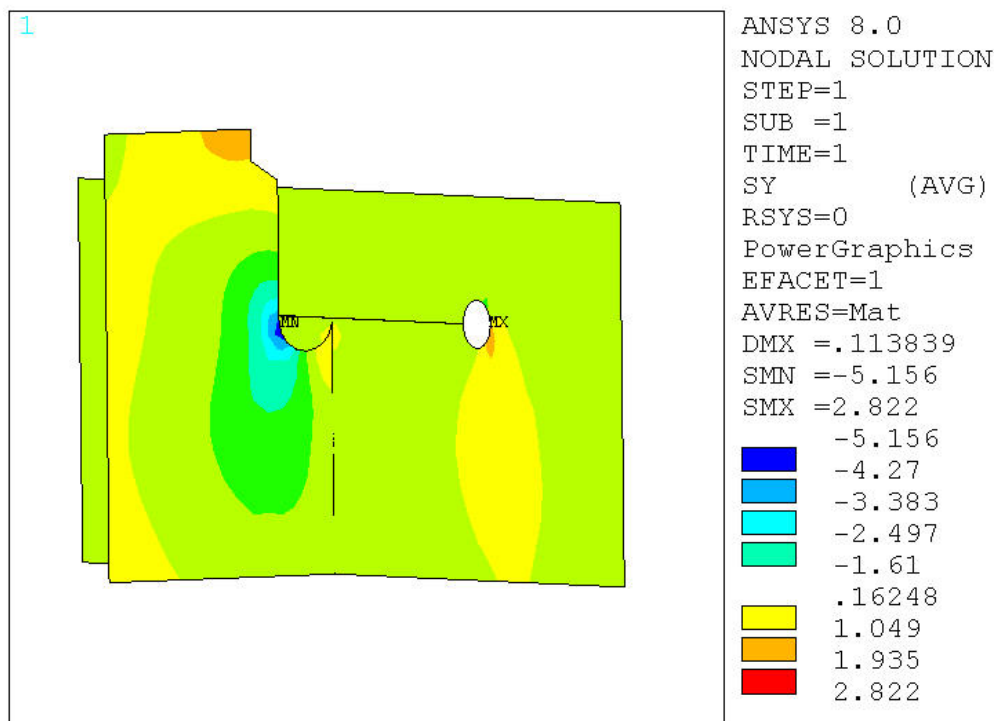


Figure 7.4: SY Stress Contours in Top Web Gap After Including a 4 inch Through Crack

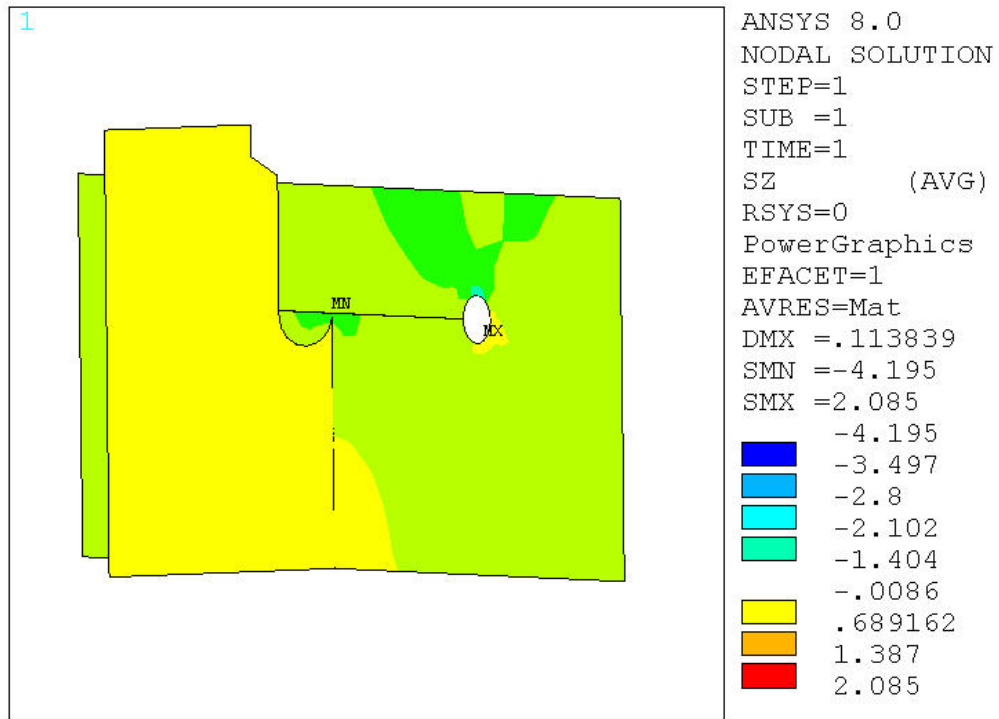


Figure 7.5: SZ Stress Contours in Top Web Gap After Including a 4 inch Through Crack.

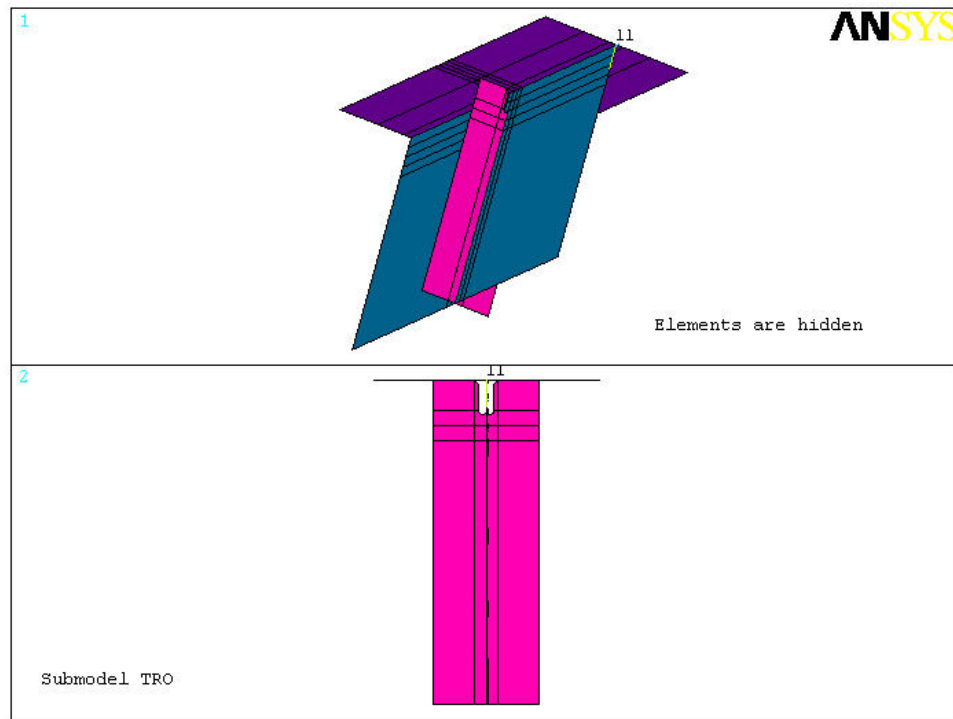


Figure 7.6: Top Web Gap Submodel With Outside Stiffener, TRO

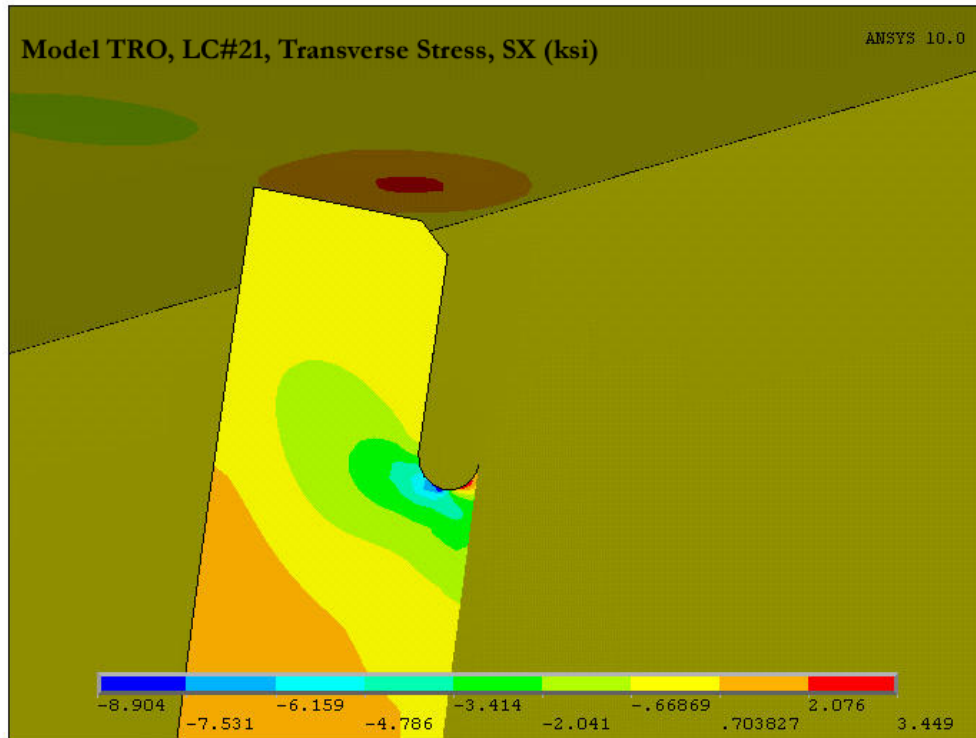


Figure 7.7: SX Stress Contours in Top Web Gap After Including an Outside Stiffener.

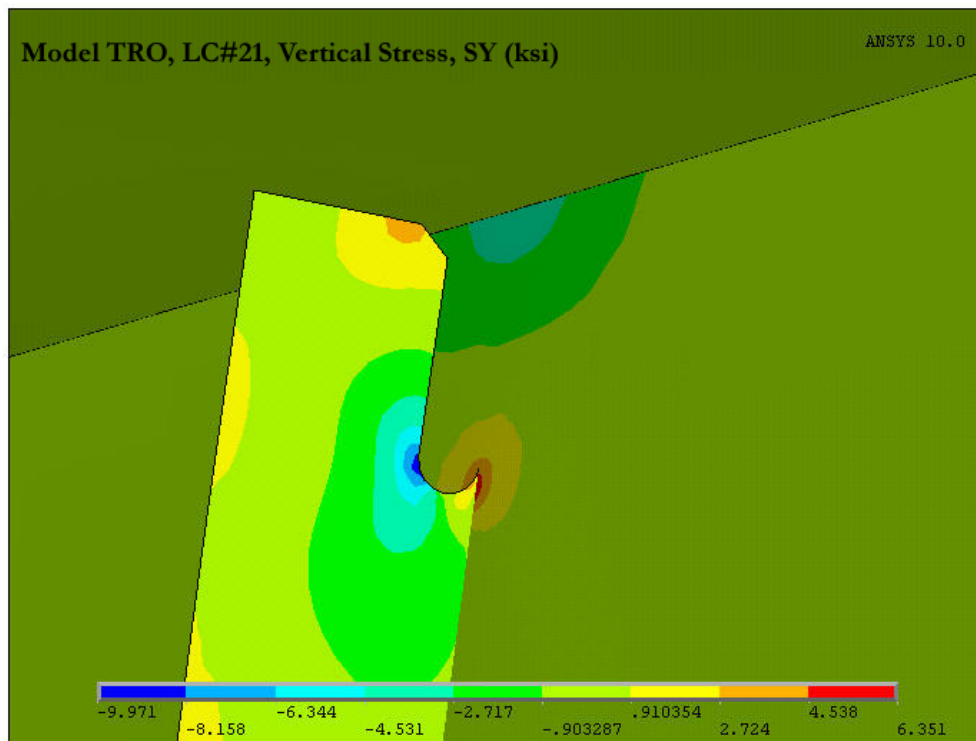


Figure 7.8: SY Stress Contours in Top Web Gap After Including an Outside Stiffener.

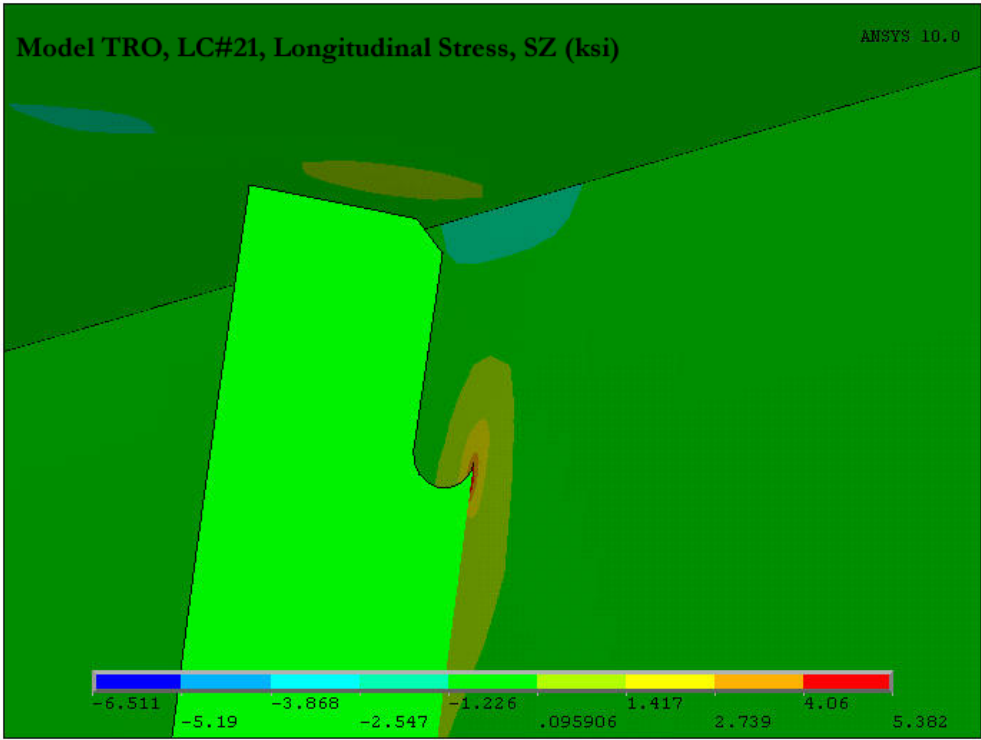


Figure 7.9: SZ Stress Contours in Top Web Gap After Including an Outside Stiffener.

CHAPTER 8: CONCLUSIONS

The Tuttle Creek Bridge is an example of a two-girder bridge with distortion induced fatigue cracking at the connections between the transverse stiffeners and the girder web. In addition to the web gap, cracks were also observed at the bottom flange-to-gusset plate connection and at the cope holes. Since the bridge lacks redundant load paths, the primary girders are fatigue critical elements, and so the fatigue critical details are of special concern for the Tuttle Creek Bridge. A finite element model was developed for a typical intermediate span of the bridge to investigate the behavior of the fatigue critical details and to evaluate the effectiveness of the newly installed retrofits. A dual-level finite element procedure was used in this study to reduce computational cost without compromising the accuracy. The finite element models were calibrated using the field strain data and in general the analytical results were in good agreement with the measured values. The analysis successfully demonstrated the effectiveness of the retrofits in reducing the stresses at the fatigue prone details below the constant amplitude fatigue limit. The following conclusions can be drawn from the study:

1. The global coarse models were built assuming noncomposite behavior of the bridge, however, the test data from the flange gages indicated that some degree of composite action is present. The study shows that considering noncomposite action in the analysis does not alter the stress distribution significantly and that the stress estimates are conservative. The measured data from the gages placed on the cross-frame members agree well with the results obtained from the coarse models. This further corroborates the validity of the noncomposite finite element model.

2. Before the retrofit the distortion induced stresses developed in the top flange web gap were higher than the CAFL. The peak stresses developed at the tip of the stiffener plate and at the flange-to-web fillet weld which explains the observed crack patterns in the upper web gap. The region of stress concentration is confined within 6 in. affected zone, 3 in. on each side of the stiffener. The analytical results are about 27% lower than the measured web gap stresses. The error is caused due to the presence of a surface crack which was not incorporated in the pre-retrofit finite element model.
3. Post-retrofit finite element model of the top flange web gap was modified to include the horizontal surface crack near the flange-to-web fillet weld. The results of the calibrated model were in good agreement with the post-retrofit field data. The error in estimation of peak stress was reduced to about 13%, thus validating the finite element model.
4. The Type 'A' repair of the top connection significantly reduced the stresses in the upper web gap. The stresses near the horizontal crack tip were reduced by 68% and stresses near the stiffener end were reduced by 87%.
5. Comparing with Fisher's formula suggest that the size stop holes at the horizontal crack tips is sufficient to prevent crack reinitiation.
6. The stresses developed in the bottom flange web gap are much lower than those developed in the top flange web gap. The pre-retrofit stresses are lower than the CAFL which explains why no cracks were found in the lower web gap region. The pre-retrofit finite element model of the lower web gap was conservative and the predicted stresses were about 75% greater than the measured stresses.

7. The Type 'B' repair of the bottom connection reduced stresses in the lower web gap significantly. The stresses after the retrofit are well below the fatigue limit of 10 ksi. The results obtained from the post-retrofit finite element model agree well with the measured field data, thus validating the finite element model.
8. The analysis of the bottom flange-to-gusset connection suggests that before the retrofits the weld terminations were the regions of stress concentration. This explains the field observations that the weld terminations were the primary sites of weld tears in the gusset plate region.
9. Post-retrofit analysis suggests that the repair scheme firmly attaches the gusset plate to the bottom flange. It reduces the prying action and eliminates the hot-spots near the weld terminations.
10. The data acquired from the gages placed on the gusset plate matched well with the analytical results thus validating the bottom flange-to-gusset model.
11. The increase in cope hole radius marginally increase the stresses around the cope hole. This increase is due to the out-of-plane movement of the flange. The stresses are well below the fatigue limit and the ultrasonic impact treatment will further improve the fatigue characteristics of the detail.
12. The new horizontal crack found at one of the cross-frame to girder connection is not a typical distortion-induced fatigue crack. The presence of the crack releases the constraints at the stiffener tip. It reduces the peak stress in the upper web gap and redistributes the hot-spot from the tip of the stiffener to the crack tip. Based on the

Fisher's formula the size of the stop holes drilled at the crack tips should be sufficient to arrest crack growth.

13. The most fatigue-prone detail on the bridge is the top flange web gap. Fatigue life calculations based on the peak stress range developed in the top web gap suggest that for the present truck volume the service life of the bridge is 230 years. If it is assumed that future traffic volume is twice the present volume the estimated service life of the bridge will be 115 years. Thus, the estimated service life of the bridge should be over 100 years.

REFERENCES

AASHTO, 1998

LRFD Bridge Design Specifications, 2nd edition. American Association of State Highway and Transportation Officials, Washington, D. C.

ANSYS Release 10.0, 2006

ANSYS, Inc., Canonsburg, Pennsylvania

Connor and Fisher, 2005

Robert J. Connor and John W. Fisher. Identifying Effective and Ineffective Retrofits for Fatigue Cracking in Steel Bridges using Field Instrumentation, Proceedings of 2005 Structures Congress, New York, NY.

Dowling, 1999

Norman E. Dowling. Mechanical Behavior of Materials: Engineering Methods for Deformation, Fracture, and Fatigue. Second Edition. New Jersey: Prentice Hall, 1999.

D'Andrea et.al., 2002

Mark D'Andrea, Gilbert Y. Grondin, and Geffory L. Kulak. Behavior and Rehabilitation of Distortion-Induced Fatigue Cracks in Bridge Girders, Structural Engineering Report No. 240, Department of Civil and Environmental Engineering, University of Alberta. Edmonton, Alberta, Canada.

Fisher et.al, 1980

John W. Fisher, B. M. Barthelemy, D. R. Mertz, and J. A. Edinger. National Cooperative Highway Research Program Report 227: Fatigue Behavior of Full-Scale Welded Bridge Attachments. Transportation Research Board, National Research Council, Washington, D.C.

Fisher et.al, 1990

John W. Fisher, Jian Jin, David C. Wagner, and Ben T. Yen. National Cooperative Highway Research Program Report 336: Distortion-Induced Fatigue Cracking in Steel Bridges. Transportation Research Board, National Research Council, Washington, D.C.

Li and Schultz, 2005

Huijuan Li and Arturo E. Schultz. Analysis of Girder Deflection and Web-Gap Stress for Rapid Assessment of Distortional Fatigue in Multi-Girder Steel Bridges, MN/RC – 2005-38, Final Report, Minnesota Department of Transportation, St. Paul, Minnesota, October 2005.

Marshall et. al., 2005

Nathan Marshall, Guillermo Ramirez, W. M. Kim Roddis, Stanley T. Rofle and Adolfo B. Matamoros. Field Instrumentation and Analysis of the Tuttle Creek Bridge BR. No. 16-81-2.24, The University of Kansas Center For Research, Inc. Lawrence, Kansas.

Roddis and Zhao, 2003

W. M. Kim Roddis and Yuan Zhao. Finite-Element Analysis of Steel Bridge Distortion-Induced Fatigue, Journal of Bridge Engineering, Volume 8, Issue 5, pp. 259-266, 2003.

Zhao, 2003

Yuan Zhao. Fatigue Prone Steel Bridge Details: Investigation and Recommended Repairs, Ph.D. dissertation. Department of Civil, Environmental, and Architectural Engineering, University of Kansas, Lawrence, Kansas.

Zhao and Roddis, 2004

Yuan Zhao and W. M. Kim Roddis. Fatigue Prone Steel Bridge Details: Investigation and Recommended Repairs, K-TRAN: KU-99-2, Final Report, Kansas Department of Transportation, Topeka KS, May 2004.

